

学位論文

SPH simulations of mergers of double white dwarf binaries: Possible progenitors of Type Ia supernovae

(二重白色矮星連星合体のSPHシミュレーション:Ia型超新星の親星としての検証)

平成28年12月博士(理学)申請

東京大学大学院理学系研究科
天文学専攻

佐藤 裕史

Abstract

Type Ia supernovae (SNe Ia) have important roles in the present astronomy as the cosmological standard candle and major producers of iron group elements. Although they have been considered as a thermonuclear explosion of a carbon-oxygen (CO) white dwarf (WD) with nearly the Chandrasekhar limiting mass in a binary system, their progenitors and explosion mechanisms are still unclear.

A merger of a double CO WD binary is one of the possible SN Ia progenitors as the double degenerate (DD) scenario, while another progenitor scenario is the single degenerate (SD) scenario, in which a CO WD explodes by accumulating hydrogen or helium-rich matter from its non-degenerate companion.

Recent observations provide several evidence which support the DD scenario, especially, SN 2011fe strongly constrains the SD scenario, and DD progenitors are considered to be more likely.

On the other hand, theoretical studies indicated that the DD model has some difficulties. In particular, according to some representative studies, rapid accretion of the secondary CO WD onto the primary in their merger could ignite off-center carbon burning quiescently, the primary would be converted to an oxygen-neon-magnesium (ONeMg) WD. If the WD pair has a total mass more massive than the Chandrasekhar limiting mass, such a system would collapse to a neutron star, not explode as an SN Ia. These were called the accretion induced collapse (AIC).

However, many hydrodynamical simulations using smoothed particle hydrodynamical (SPH) codes were performed recently, and they showed that there are some possible paths in which merging CO WDs could lead to SNe Ia. For examples, Yoon et al. (2007) indicated that the off-center carbon burning could be avoided if some conditions are satisfied, e.g., for a low accretion rate of $< 10^6 M_{\odot} \text{ yr}^{-1}$ due to sufficient rotational support and slow angular momentum transfer. In such cases, the primary CO WD can grow its mass without being converted to an ONeMg WD and lead to an SN Ia explosion $\sim 10^6$ yr after the merger.

In another case, Pakmor et al. (2010) showed that carbon detonation could be initiated in the dynamical merger phase of very massive $\sim 0.9 M_{\odot}$ CO WDs. They also presented that the detonation waves propagate through the primary CO WD and convert it to radioactive nickel, although the secondary is converted to intermediate elements (e.g., silicon, sulfur). They calculated the light curve and spectra of such events with their radiative transfer code, and found that they could reproduce observational properties of subluminous SNe Ia, such as SN 1991bg-like events. They called such explosion mechanism the violent merger scenario. After that, they also simulated a more massive merger in which masses of CO WDs are $1.1 M_{\odot}$ and $0.9 M_{\odot}$. They showed that the merger could explain a normal SN Ia, although its highly asymmetric profile seems to be inconsistent with observations.

These studies indicated that the DD scenario could lead to an SN Ia explosion without collapsing to a neutron star along the AIC scenario. However, what CO WD binaries could lead to SNe Ia is still uncertain. Especially, a mass range of merging CO WDs exploding as SNe Ia is significantly important to understand the DD scenario and the nature of SNe Ia.

In this study, we performed three dimensional SPH simulations of CO WD mergers for various mass combinations ranging $0.5 \sim 1.1 M_{\odot}$, and examined possibilities leading to SNe Ia. Our simulations have higher numerical resolution than any previous studies and adopt a plausible initial condition. As a result, we find that double CO WD binaries with massive primary and secondary stars ($> 0.8 M_{\odot}$) could explode during their mergers, along the violent merger scenario. We also derive the critical mass ratio of the violent merger scenario, above which mergers explode as SNe Ia. Our critical mass ratio ($q_{\text{cr}} \sim 0.9$ for $0.9 M_{\odot}$) is larger than that obtained by previous study ($q_{\text{cr}} \sim 0.8$ for the same mass). We conclude that this difference mainly comes from differences between our and their initial conditions. We also discuss an impact of the critical mass ratio on the peak brightness distribution of SNe Ia.

Mergers of CO WDs could lead to SNe Ia in their post-merger phases when their primary masses are less than $0.9 M_{\odot}$, their mass ratios are less than the critical one of the violent merger scenario, and their total masses exceed the Chandrasekhar mass, although more studies for the post-merger evolution are needed.

We derive a relation between merger outcomes and mass combinations of merging CO WDs, and derive the possible mass range leading to SNe Ia. Using the derived relation, we briefly evaluate a ratio of DD mergers leading to SNe Ia as less than 8% of all WD mergers. We also predict the final fate of Henize 2-428, a bipolar planetary nebula, whose central system is recently suggested as a super-Chandrasekhar DD binary. Our consequence indicates that the core of Henize 2-428 would explode as an SN Ia along the violent merger scenario.

Contents

Abstract	iii
1 Introduction	1
1.1 Supernova classification	1
1.2 Type Ia supernovae	2
1.3 Progenitor problem of SNe Ia	7
1.3.1 Observational clues	8
Single degenerate model	8
Double degenerate model	9
1.3.2 Theoretical studies	13
Single degenerate model	13
Double degenerate model	15
1.4 Aim of this thesis	17
2 Numerical Methods	20
2.1 Overview of SPH	20
2.2 Numerical configuration	24
2.2.1 Numerical code and computational environment . .	24
2.2.2 Gravity	25
2.2.3 Smoothing length	25
2.2.4 EOS and Nuclear reaction	25
2.2.5 Artificial viscosity	26
2.2.6 Time integration	27
2.3 Initial setup	27
2.3.1 Single CO WD	27
2.3.2 Binary CO WD	28
Resolution dependence of initial condition	30
2.4 Simulation run	32
3 Simulation Results	33
3.1 Overview	33
3.2 Dynamical merger phase	37
3.2.1 Violent merger scenario	37
3.2.2 Conditions for the violent merger scenario	37
3.2.3 The critical mass ratio for violent merger scenario . .	39
3.3 Remnant phase	42
3.4 Merger outcomes	48
3.4.1 Ratio of WD mergers leading to SNe Ia	50
4 Discussion	52
4.1 Dependence on the numerical resolution	52
4.2 Comparison with the previous studies	54
4.2.1 Individual models	56
The case of $1.1 + 0.9 M_{\odot}$	56

	The case of $0.9 + 0.6 M_{\odot}$	57
4.2.2	The critical mass ratio	59
	Nuclear burning	60
	Initial condition	64
	Numerical resolution	67
	Brightness distribution of the violent merger-induced SNe Ia	68
4.2.3	Other parameter surveys	70
4.3	The final fate of Henize 2-428	72
4.3.1	The observational properties of Henize 2-428	72
4.3.2	Predicting the merger outcome of Henize 2-428	73
5	Conclusion and Remarks	79
	Acknowledgements	83
A	Summary of Our Simulation	84
	Bibliography	91

Chapter 1

Introduction

1.1 Supernova classification

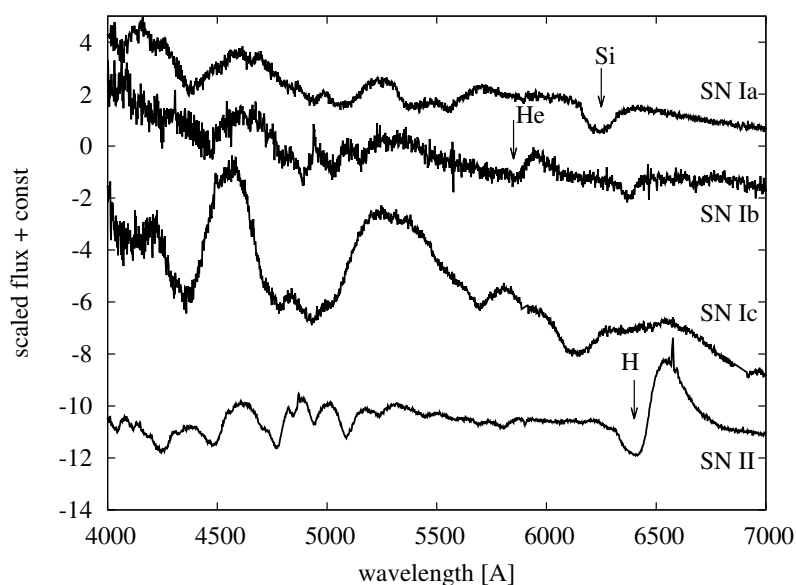


FIGURE 1.1: Typical spectra of various SN types near optical maximum. The vertical axis is the linearly scaled flux and shifted by some constant for visibility. The example of SN Ia is SN 2000fa (Jha et al., 2006; Matheson et al., 2008), SN Ib is SN 2005bf (Tominaga et al., 2005), SN Ic is SN 1994I (Millard et al., 1999), and SN II is SN 1999gi, which is an SN IIP (Leonard et al., 2002). Data is obtained from the CfA Supernova Data Archive (<http://www.cfa.harvard.edu/supernova/SNarchive.html>).

Supernovae (SNe) are explosions of stars at the end of their lives. They are classified by their properties of observational spectra (e.g., Filippenko, 1997). At first, they are divided into two types from the presence/absence of hydrogen (H). Type I SNe do not show H lines in their spectra, while the events having them is sorted into Type II (SNe II). Type I events are further divided into three sub-types. Type Ia supernovae (SNe Ia) have strong silicon features around 6200 Å, which is originally 6355 Å and shifted to bluer by the Doppler effect of the SN ejecta velocity ($\sim 10^4$ km s $^{-1}$). Among Type I SNe not having strong silicon signatures, the events showing helium (He) lines in their peak spectra are classified into Type Ib (SNe Ib). On the other

hand, Type I SNe with neither Si nor He are called Type Ic (SNe Ic). We summarize typical spectra of each type in Figure 1.1.

In the present astronomy, SNe Ib, SNe Ic, and SNe II are considered as explosions of massive stars ($> 8 M_{\odot}$) at the death of them (e.g., Smartt, 2009). They are summarized as core collapse supernovae (CC SNe) because the gravitational collapse of an iron core in a massive evolved star induces such an explosion. CC SNe usually remain compact remnants, such as a neutron star or black hole. On the other hand, an SN Ia is considered as a thermonuclear explosion of a carbon-oxygen (CO) white dwarf (WD). CO WDs are produced from intermediate mass stars ($1 \sim 8 M_{\odot}$) (e.g., Umeda et al., 1999). In this sense, SNe Ia are explosions at the end of evolution of intermediate mass stars, not massive stars like CC SNe. SNe Ia are usually considered not to leave any compact remnants, although some theoretical studies suggested that compact remnants might exist in some cases (e.g., Jordan et al., 2012; Kromer et al., 2013a; Kromer et al., 2015; Fink et al., 2014), and there is an observational report of a possible candidate of the compact remnant (Foley et al., 2014).

1.2 Type Ia supernovae

SNe Ia, which are thermonuclear explosions of CO WDs (e.g., Hoyle and Fowler, 1960), play important roles as cosmological standard candles (e.g., Riess et al., 1998; Perlmutter et al., 1999) and major sources of iron group elements in galactic chemical evolution (e.g., Timmes et al., 1995; Kobayashi et al., 1998), in the astronomy. Many excellent reviews for SNe Ia are available in Hillebrandt and Niemeyer (2000), Howell (2011), Hillebrandt et al. (2013), and Maoz et al. (2014). Here, we briefly mention the overview of SNe Ia. Because spectra of SNe Ia do not show hydrogen features and SNe Ia appear in the both old and young populations, we can expect that SN Ia progenitors would associate with H-poor and evolved stars¹. From shape of its light curve, luminosity of an SN Ia is driven by radioactive nickel (^{56}Ni), and cobalt (^{56}Co). Moreover, its spectra show strong silicon features. These chemical composition implies combustion of degenerate CO mixtures. The fact that SNe Ia have relatively uniform luminosities than CC SNe indicates that the amount and physical conditions of combustion would be similar among the events. The typical mass of synthesized ^{56}Ni is about $0.6 M_{\odot}$ from its peak luminosity. Ejecta mass could be estimated from width of light curve. The total ejected mass typically lies around $\sim 1.4 M_{\odot}$ (e.g., Mazzali et al., 2007; Childress et al., 2015)². Recently, Nugent et al. (2011) analyzed early lightcurves of SN 2011fe, which was one of the most nearby SNe Ia discovered in decades, and set a constraint on radius of the exploding star $< 0.1 R_{\odot}$. This limit supports that SN Ia is an explosion of a compact object, like a CO WD. These observational features indicate that the exploding object is a CO WD having near the Chandrasekhar mass

¹CC SNe originating from the death of massive stars typically occur in young stellar populations.

²However, recent studies (e.g., Scalzo et al., 2014a; Scalzo et al., 2014b; Childress et al., 2015) indicated the presence of SNe Ia having sub-Chandrasekhar mass ejecta. These events might come from different progenitors from near-Chandrasekhar events.

limit, $M_{\text{Ch}} \sim 1.4 M_{\odot}$ (e.g., Hoyle and Fowler, 1960; Nomoto et al., 1984)³.

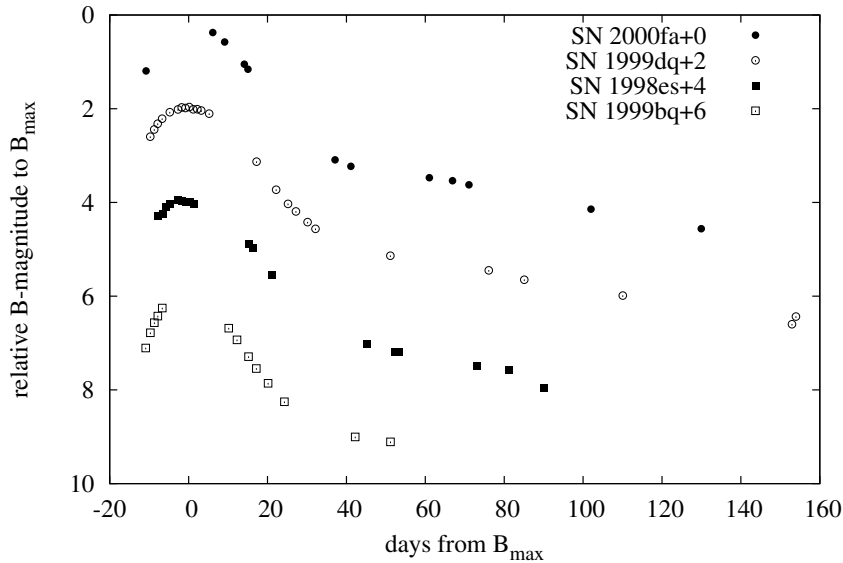


FIGURE 1.2: Typical lightcurves of normal SNe Ia from Jha et al. (2006). The vertical axis is relative B-band magnitude to their maximum B-band magnitudes (B_{max}). They are shifted by some constant, which are presented in their labels, for visibility. Data are obtained from the CfA Supernova Data Archive

(<http://www.cfa.harvard.edu/supernova/SNarchive.html>).

Since SNe Ia are one of the most luminous transients in our universe (typical luminosity is $\sim 10^{43}$ erg s^{-1}), we can observe them even in the cosmological distance. They have relatively uniform lightcurves and spectra, although some diversity is present⁴. Figure 1.2 shows lightcurves of some normal SNe Ia (Jha et al., 2006). We can confirm their similarity. There is a tight correlation between the peak magnitudes of SNe Ia and the decline rates of lightcurves (e.g., Pskovskii, 1977). Phillips (1993) found that the absolute maximum magnitudes of SNe Ia in each band could be empirically obtained as a function of $\Delta m_{15,B}$, which is a decline magnitude in B-band after 15 days from their peak brightness. The formulae is expressed as

$$M_{\text{max}} = a + b \Delta m_{15,B}, \quad (1.1)$$

where M_{max} is the maximum magnitude, a and b are constants, for each band. Such a correlation is called the Phillips relation. Figure 1.3 shows an example of this relation for SNe Ia in Table 1 of Hamuy et al. (1996), which were observed in the Calán/Tololo SN survey (Hamuy et al., 1993). We can confirm its tight correlation between the absolute B-band magnitudes B_{max} and the decline rates of their B-band light curves $\Delta m_{15,B}$. We also express

³The energetics is also consistent. The nuclear energy from $\sim 0.6 M_{\odot}$ (a factor of 10^{51} erg) is comparable to the sum of the binding energy of a CO WD with M_{Ch} and the kinetic energy of SN ejecta with M_{Ch} and 10^4 km s^{-1}

⁴A part of such diversity might be generated from an aspherical explosion due to off-center carbon ignition in the CO WD (Maeda et al., 2010).

the approximate relation (Equation 1.1) as a black solid line in Figure 1.3, whose constants are the same as those presented in Table 3 of Hamuy et al. (1996). Therefore, we can estimate the absolute luminosity of an SN Ia from the relation, and measure the distance to the SN (and its host galaxy). Due

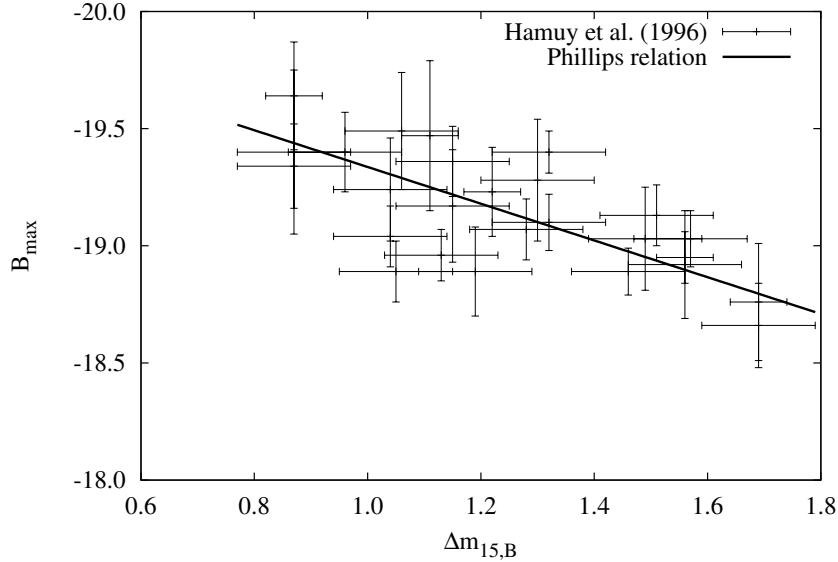


FIGURE 1.3: The Phillips relation between the maximum absolute B-band magnitudes B_{\max} and the decline rates of B-band magnitude $\Delta m_{15,B}$ of SNe Ia observed in the Calán/Tololo SN survey (symbols with errorbars). Data are obtained from Hamuy et al. (1996), but we omitted three events significantly reddened. The black solid line is an approximate formula expressed as Equation 1.1, where $a = -19.26$ and $b = 0.78$ from Hamuy et al. (1996).

to its powerful luminosity and the Phillips relation, SNe Ia are used as a standard candle which is applicable even in the cosmological distance up to $z \sim 2$ (e.g., Howell, 2011). Using the cosmic lighthouses, the distances to high- z galaxies were measured, and an amazing fact that the expansion of our universe is accelerating was discovered (e.g., Riess et al., 1998; Perlmutter et al., 1999)⁵.

A thermonuclear explosion of a CO WD with the mass of near M_{Ch} typically produces $0.6 \sim 0.7 M_{\odot}$ of radioactive nickel ^{56}Ni , which finally decay into stable iron ^{56}Fe (e.g., Nomoto et al., 1984; Khokhlov, 1991; Iwamoto et al., 1999; Seitenzahl et al., 2013). This is sufficient to explain the luminosity and kinetic energy observed in a typical SN Ia event, and the predicted lightcurve, spectra, and abundances are also consistent with the observations (e.g., Höflich, 1995; Nugent et al., 1997; Röpke et al., 2012). On the other hand, although there is some diversity, a typical amount of ^{56}Ni ejected from a CC SN is about $0.1 M_{\odot}$ (e.g., Woosley and Weaver, 1995). In a CC SN, the matter locating near the center would be accreted by or

⁵Their discoveries were awarded the Nobel Prize 2011 in Physics, "for the discovery of the accelerating expansion of the Universe through observations of distant supernovae".

fall-back into its compact remnant after the explosion, while an SN Ia explosion blows off the CO WD entirely, and the central matter, which contain a plenty of iron, could be successfully ejected. According to estimates from detailed nucleosynthesis calculations and chemical evolution models of galaxies, a large fraction of iron group elements would come from SNe Ia, while CC SNe make a significant contribution to oxygen, neon, and magnesium (e.g., Timmes et al., 1995; Kobayashi et al., 1998; Thielemann et al., 1986).

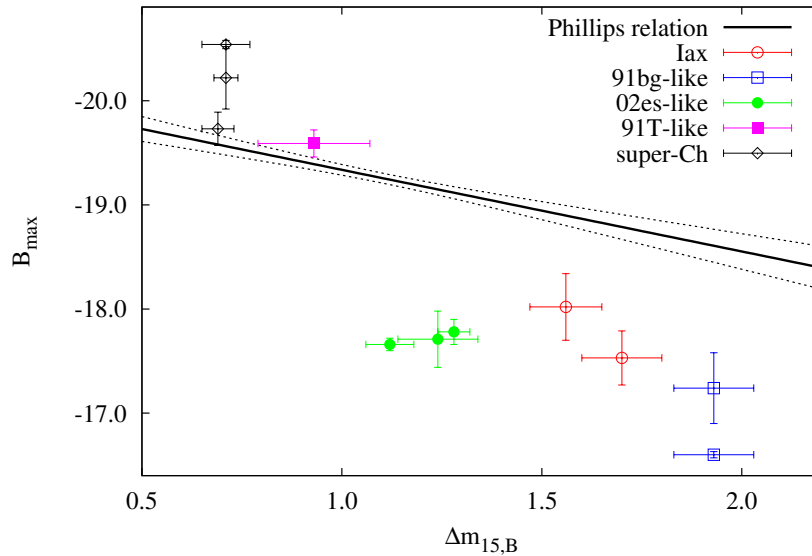


FIGURE 1.4: Deviations of the peculiar SNe Ia from the Phillips relation. The data are summarized in Table 1.1. The dashed black lines indicate $1\text{-}\sigma$ errors.

Although SNe Ia had been considered to be homogeneous within the Phillips relation, recent observations revealed that there are some peculiar sub-types of SNe Ia deviating from the relation (e.g., Gal-Yam, 2016). We just mention them briefly here.

1. SNe Iax (or SN 2002cx-like), introduced by Foley et al. (2013), have relatively lower peak brightnesses (~ 18 mag), lower ejecta velocities ($\sim 8000 \text{ km s}^{-1}$), and higher temperatures of photosphere, which resemble SN 2002cx (e.g., Li et al., 2003). The estimated fraction of Iax events is about a few to 30% (e.g., Li et al., 2011b; Foley et al., 2013).
2. Another subluminescent SNe Ia is the SN 1991bg-like event (e.g., Filippenko et al., 1992b; Leibundgut et al., 1993). Their lightcurves decline faster than the typical SNe Ia and do not have the second peak in R-band which appears in the normal SNe Ia. The spectra show a trough produced by absorption lines of iron group elements, mainly Ti II due to its low photospheric temperature. Unlike SNe Iax, the ejecta velocity is almost consistent with a typical value of normal SNe Ia.
3. SN 2002es-like events are also subluminescent peculiar SNe Ia and have low ejecta velocities, like SNe Iax (e.g., Ganeshalingam et al., 2012).

However, they have some differences from SNe Iax, e.g., the shorter rise time of their lightcurves due to their lower ejecta masses, Ti II troughs in their spectra due to their lower photospheric temperature (like SN 1991bg-like event), and trend to appear in old hosts (e.g., White et al., 2015)⁶. Foley et al. (2013) classified them as a different sub-type from SNe Iax.

4. Filippenko et al. (1992a) found that Fe III lines appeared before the peak spectra of SN 1991T, which is different from normal SNe Ia. Mazzali et al. (1995) reported that SN 1991T-like SNe Ia had higher luminosities and hotter photospheres than the normal ones. SN 1991T-like events seem to obey the Phillips relation, unlike above subluminal peculiar SNe Ia (e.g., Blondin et al., 2012).
5. Recent observations revealed that there were several events with much higher luminosity than twice of a typical SN Ia ($\sim 10^{43}$ erg s⁻¹). Their magnitudes came up to < -20 mag and total ejected masses exceeded $2 M_{\odot}$. Such SNe Ia are called the super-Chandrasekhar SNe Ia, e.g., SN 2003fg (e.g., Howell et al., 2006), SN 2006gz (e.g., Hicken et al., 2007), SN 2007if (e.g., Scalzo et al., 2010), and SN 2009dc (e.g., Yamamoto et al., 2009; Silverman et al., 2011). Because they do not show pre-peak Fe III features in their spectra and they are much more luminous than the normal ones, they would be a different population from SN 1991T-like events. Their ejecta velocities are relatively lower ($< 10^4$ km s⁻¹) than those of the normal SNe Ia, and C II lines appear around the peak luminosity. These observational properties imply the existence of unburned carbon in the outer ejecta. Some mechanisms and progenitors of super-Chandrasekhar SNe Ia have been suggested. For example, Hillebrandt et al. (2007) considered that the overluminosity might arise from asphericity of explosion of a CO WD with nearly M_{Ch} . However, Tanaka et al. (2010) found that SN 2009dc was almost spherical explosion by observing its spectropolarimetry. On the other hand, Scalzo et al. (2010), Yuan et al. (2010), and Noebauer et al. (2016) proposed the interaction between the SN ejecta and circumstellar matter as the source of the luminosity.

Although some populations of SNe Ia do not obey the Phillips relation, a significant fraction of SNe Ia ($> 60\%$) is considered to belong to the normal events obeying the relation, and we can distinguish peculiars from the normal SNe Ia by the spectra and lightcurve shapes. For example, Li et al. (2011b) estimated that a fraction of normal SNe Ia is about 70%, slow velocity SNe Ia (SNe Iax + SN 2002es-like events) 5%, SN 1991bg-like events 15%, and SN 1991T-like events 9%, from the observations of nearby galaxies. Therefore, SNe Ia can be still one of the most powerful distance indicators in the universe (e.g., Howell, 2011). We depict the place where the peculiar SNe Ia locate in the $B_{\text{max}} - \Delta m_{15,B}$ plane and how they deviate from the Phillips relation. We show the representative examples for each

⁶White et al. (2015) speculated that SN 2002es-like events might arise from the incomplete explosions of CO WDs by pure deflagration (Kromer et al., 2013a; Kromer et al., 2015), while SN Iax might be results of the violent merger-induced explosions (see Pakmor et al., 2010, and our Section 3.2).

peculiar SN Ia, although data of the SN 1991T-like event are derived from the mean properties in Table 5 of Blondin et al. (2012). The summary of the data is presented in Table 1.1.

SNID	Type	B_{\max}	$\Delta m_{15,B}$	References
SN 2002cx	Iax	-17.53 ± 0.26	1.70 ± 0.10	(a)
SN 2005hk	Iax	-18.02 ± 0.32	1.56 ± 0.09	(a)
SN 1991bg	91bg-like	-16.60 ± 0.03	1.93 ± 0.10	(b)
SN 2005bl	91bg-like	-17.24 ± 0.34	1.93 ± 0.10	(b)
PTF09dav	91bg-like	-15.33 ± 0.08	1.87 ± 0.06	(c)
SN 1999bh	02es-like	-17.71 ± 0.27	1.24 ± 0.10	(d)
SN 2002es	02es-like	-17.71 ± 0.27	1.24 ± 0.10	(d)
PTF10ops	02es-like	-17.66 ± 0.06	1.12 ± 0.06	(e)
$\langle 91T - \text{like} \rangle$	91T-like	-19.59 ± 0.13	0.93 ± 0.14	(f)
SN 2006gz	super-Chandrasekhar	-19.73 ± 0.16	0.69 ± 0.04	(g)
SN 2007if	super-Chandrasekhar	-20.54 ± 0.04	0.71 ± 0.06	(h)
SN 2009dc	super-Chandrasekhar	-20.22 ± 0.30	0.71 ± 0.03	(i)

TABLE 1.1: Summary of the data of the representative peculiar SNe Ia shown in Figure 1.4. $\langle 91T - \text{like} \rangle$ is the mean properties of SNe Ia classified as SN 1991T-like events (Blondin et al., 2012). The labels of References are, (a) Phillips et al. (2007), (b) Taubenberger et al. (2008), (c) Sullivan et al. (2011), (d) Ganeshalingam et al. (2012), (e) Maguire et al. (2011), (f) Blondin et al. (2012), (g) Hicken et al. (2007), (h) Scalzo et al. (2010), and (i) Taubenberger et al. (2011).

1.3 Progenitor problem of SNe Ia

Despite their astronomical importance, the progenitors of SNe Ia are still unclear. We can deduce that the progenitor systems of SNe Ia would be binaries with a CO WD component from the above considerations. Because an isolated CO WD, whose mass distribution has its peak around $0.6 M_{\odot}$ (Kleinman et al., 2013), cannot explode by itself, it has to get mass from other stars. As the CO WD grows its mass, its central density becomes higher. When its mass reaches the critical mass, $M_{\text{ig}} = 1.38 M_{\odot}$, explosive carbon burning ignites at its center, and blows off the entire CO WD (e.g., Nomoto, 1982a). However, whether a companion from which the CO WD accumulates matter is non-degenerate star, e.g., main sequence, red giant (single degenerate, SD model), or degenerate one, e.g., CO WD (double degenerate, DD), is still controversial. In the SD model, the WD accretes H (or He) rich matter from the companion by wind or the Roche lobe over flow (RLOF), and increases its mass (Whelan and Iben, 1973). On the other hand, in the DD model, the binary CO WD loses its orbital angular-momentum emitting gravitational waves, shrinks its orbital separation, and increases

its mass by merging (Iben and Tutukov, 1984; Webbink, 1984)⁷. In the classical DD scenario, if the total mass of the DD system exceeds M_{ig} , it would lead to an SN Ia explosion.

Here, we briefly summarize the representative observational clues and theoretical studies for progenitors⁸.

1.3.1 Observational clues

Single degenerate model

Some recent observations show that a few SNe Ia including peculiar events have possible signatures of a companion (e.g., Foley et al., 2014; McCully et al., 2014; Cao et al., 2015; Marion et al., 2016). Recently, McCully et al. (2014) reported the discovery of a luminous blue star in the pre-explosion image of an SN Iax event, SN 2012Z. Because its luminosity and color are consistent with a helium star, they proposed that SN 2012Z might be originated from an explosion of a CO WD accreting from a helium star.

Foley et al. (2014) discovered a possible surviving companion in the post-explosion image of SN 2008ha, which is an extremely dim SN Iax⁹. They found that its properties were consistent with stellar evolution models for $\sim 3 M_{\odot}$ star¹⁰.

Cao et al. (2015) found that iPTF14atg, which was considered to belong to SN 2002es-like event (e.g., Ganeshalingam et al., 2012), showed a strong UV flash in its early lightcurve, which indicates the signatures of the ejecta-companion interaction expected from Kasen (2010)¹¹. In a normal SN Ia, Marion et al. (2016) reported that SN 2012cg had early blue excess in B-V color possibly arising from the the interaction between the ejecta and $\sim 6 M_{\odot}$ main sequence companion though Maguire et al. (2016), Liu and Stancliffe (2016), and Shappee et al. (2016) had doubts on the interpretation because the deep observations for H_{α} emission in its late time put strong constraints on the mass ejected from the progenitor of $< 0.01 M_{\odot}$.

Some SNe Ia show the signatures of circumstellar matter (CSM) ejected from the companions before explosions, called the SNe Ia-CSM (e.g., Silverman et al., 2013b). Patat et al. (2007) found variable blueshifted Na I D absorption lines in the spectra of SN 2006X. They were interpreted as the intervening lines formed by the CSM with low velocity $10 \sim 100 \text{ km s}^{-1}$ lying between the SN and the observers. Several observations showed that nearly $20 \sim 30\%$ had such blueshifted Na I D absorption lines, including observations without checking the time-variation (e.g., Sternberg et al., 2011; Foley et al., 2012b; Maguire et al., 2013; Phillips et al., 2013). Hamuy et al. (2003) discovered strong Balmer lines of hydrogen originating from the

⁷Although the core degenerate (CD) model (e.g., Kashi and Soker, 2011) and the collision between two CO WDs (e.g., Kushnir et al., 2013) are also suggested as other progenitor models, these are out of the scope of this thesis.

⁸As a recent good review, Maoz et al. (2014) summarized details of observational studies for SN Ia progenitors.

⁹They also suggested that the object might be a remnant left by incomplete explosion of a CO WD induced by off-center ignited pure-deflagration (Kromer et al., 2013a).

¹⁰Moriya et al. (2010) suggested that SN 2008ha was a CC SNe with small ejecta kinetic energy and massive fallback.

¹¹Recently, Kromer et al. (2016) speculated that iPTF14atg might originate from the CO WD merger of $0.9 + 0.76 M_{\odot}$ because of its several observational properties. However, the early UV flash could not be explained by their model.

ejecta-CSM interaction, in an SN 1991T-like event, SN 2002ic¹². SN 2005gj is considered as the similar event (e.g., Prieto et al., 2007). Another SN Ia-CSM PTF11kx also had explicit hydrogen features, time-variable Na I D lines, and multiple CSM shells (e.g., Dilday et al., 2012; Silverman et al., 2013a). Its progenitor might be a SD system whose companion is a red giant, and experience multiple novae (Dilday et al., 2012). However, Soker et al. (2013) argued that the estimated mass of CSM in PTF11kx, $> 0.1 M_{\odot}$, was too large for the SD progenitor, and the merger of a CO WD and an AGB core during the common envelope, i.e., the core degenerate scenario, might be more likely¹³.

Recently, another super-Chandrasekhar SNe Ia candidate, SN 2012dn appeared (e.g., Brown et al., 2014). The spectra of SN 2012dn was similar to those of SN 2006gz (Chakradhari et al., 2014) though it was less luminous than SN 2009dc. Yamanaka et al. (2016) observed that its color evolution was also consistent with that of SN 2009dc, and showed that there were signatures of NIR echo from surrounding dust formed from pre-explosion mass loss. The mass loss was estimated as $10^{-6\sim-5} M_{\odot} \text{ yr}^{-1}$ and would support the SD system as the progenitor of some super-Chandrasekhar SNe Ia, if SN 2012dn belongs to them. These cases might be explained by the SD model.

Double degenerate model

On the other hand, there are some observational clues which support the DD model (e.g., Maoz et al., 2014). As discussed above, the SD model has several detectable observational predictions due to the presence of non-degenerate companion, e.g., pre/post-explosion image of the companion, SN ejecta-companion interaction, the signatures of CSM emerging from the companion. If such evidence was not detected, the SD model is severely constrained and the DD model is preferred.

For examples, in the SD model, the companion star would be observed before and after the SN Ia explosion. Especially, the surviving companion would be collided with the SN ejecta, and consequently, have an anomalous location on the Hertzsprung-Russell (HR) diagram, peculiar surface abundances, and proper motion. However, there has ever been no detection of companions of the normal SNe Ia in the pre/post-explosion (e.g., Li et al., 2011a; González Hernández et al., 2012; Kerzendorf et al., 2012; Schaefer and Pagnotta, 2012), although there are some arguments about a possible candidate of the surviving companion of SN 1572 (Tycho's SN), so-called Tycho's G-star (e.g., Kerzendorf et al., 2013; Bedin et al., 2014)¹⁴. Kelly et al. (2014) observed SN 2014J¹⁵, which was the nearest SN Ia appeared in M 82 (~ 3.5 Mpc) (e.g., Goobar et al., 2014), and rejected a red giant as its possible

¹²There are some studies arguing that the events similar to SN 2002ic might be actually a SN Ib/c with ejecta-CSM interaction (e.g., Benetti et al., 2006).

¹³Some mechanisms which could explain the CSM signatures in the DD model have been proposed (e.g., Raskin and Kasen, 2013; Shen et al., 2013).

¹⁴Noda et al. (2016) found that no detection of the surviving companion might be explained by mass-stripping and energy injection due to the collision between SN ejecta and companion's envelope.

¹⁵SN 2014J was discovered by Steve Fossey and his four undergraduate students during their observational training at University of London Observatory (Fossey et al., 2014).

companion in the SD model.

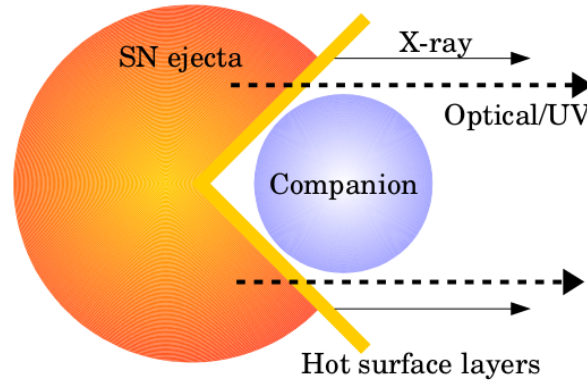


FIGURE 1.5: A schematic figure of the interaction between the SN ejecta and the companion and the X-ray and optical/UV emission from the shock-heated matter. See text for details.

When SN ejecta collide with the companion star, some detectable signatures of the interaction would be expected in the early observation, especially, in the UV and X-ray bands. Kasen (2010) estimated such emission, and found that the ejecta-companion interaction produces a prompt X-ray flash ($10^2 \sim 10^4$ s) and optical/UV emission (a few days). Their typical luminosities are $\sim 10^{44}$ erg s $^{-1}$ for the X-ray flash and $\sim 10^{41\sim 43}$ erg s $^{-1}$ for the optical/UV emission, respectively. Although such signatures have strong viewing-angle dependence, they are bright enough to be detected in the early lightcurves of nearby SNe Ia. Since early optical/UV emission becomes more prominent as the radius of the progenitor increases, we can estimate or limit the possible progenitor of an SN Ia from its early lightcurves. We depict a schematic pictures of the signatures in Figure 1.5. When the SN ejecta collide with the companion, the ejecta is shock-heated, and forms dense and hot surface layers. The hot layers are exposed because the companion opens a cone-shaped hole. At first, a part of the thermal energy generated by the shock-heating is observed in the X-ray. Subsequently, photons which can not escape from the layers due to their longer diffusion timescales emit, but they are lowered to the optical/UV wavelengths because of adiabatic cooling. These correspond to the later optical/UV emission.

Several observations have investigated the presence of the emission from the ejecta-companion interaction for a number of SNe Ia with early lightcurves in multiple bands, and set constraints on their progenitors (e.g., Hayden et al., 2010; Bianco et al., 2011; Ganeshalingam et al., 2011; Brown et al., 2012b; Foley et al., 2012a). Especially, they ruled out red giants from the candidates of the progenitors for a large fraction of the SNe Ia. Olling et al. (2015) searched such signatures for a few SNe Ia discovered by the *Kepler*, which is a space observatory operated by NASA, and reported no detection of them. These observations limit the presence of non-degenerate companions in SNe Ia, i.e., the SD model. In the DD model, some materials are scattered during the merger of WDs, and would form CSM before the explosion (e.g., Fryer et al., 2010; Raskin and Kasen, 2013). The collision between such CSM

and SN ejecta possibly produce similar signatures to the emission from the ejecta-companion interaction in the SD models (e.g., Nugent et al., 2011).

Kutsuna and Shigeyama (2015) performed multi-dimensional radiative hydrodynamical simulations of some collisions between SN ejecta and companion stars. They pointed out that the brightness of emission from the ejecta-companion interaction become lower in the case of non-LTE, where the temperature of ejecta is different from that of radiation, while Kasen (2010) assumed the LTE situation. As a result, the SD model might be able to avoid the above observational constraints¹⁶.

Another observational clues of the SD model is the signatures of hydrogen stripped from the non-degenerate companion observed in the late phase spectra. According to the mesh-based hydrodynamical simulations performed in Marietta et al. (2000), the SN ejecta strips about $> 0.1 M_{\odot}$ from the envelope of the companion. Several observational studies (e.g., Mattila et al., 2005; Leonard, 2007; Lundqvist et al., 2013; Lundqvist et al., 2015; Maguire et al., 2016) put constraints on the stripped hydrogen mass from the late phase spectra in a number of SNe Ia, and found that their results ($\sim 0.01 M_{\odot}$) were too small to be consistent with the prediction of Marietta et al. (2000). Pakmor et al. (2008) performed similar simulations using their SPH code, and found the stripped mass ($\sim 0.01 M_{\odot}$) being much less than the prediction of Marietta et al. (2000) and consistent with some observational limits. They discussed that the differences come from the structure of companion, which was derived from their binary evolution model.

The interaction between the SN ejecta and CSM formed by stellar winds of a non-degenerate companion also produces the expected signatures of the SD model in X-ray and radio bands (e.g., Chomiuk et al., 2012; Margutti et al., 2012). However, there has been no detection of such signatures from SNe Ia although some SNe Ia showed different CSM signatures, e.g., hydrogen lines, variable Na I D lines (see Maoz et al., 2014, and references therein). As mentioned above, a small amount of matter is ejected and form CSM in mergers of double WD binaries, this constraints might be applied to the DD model, not only to the SD model.

The event which was put the strongest constraints on the SD progenitor is SN 2011fe (e.g., Chomiuk, 2013). SN 2011fe was a normal SN Ia which was discovered in M101 (Nugent et al., 2011). Because of its close distance and intense observations from the very early phase, SN 2011fe has been a best-studied SN Ia. The representative observational limits for its progenitor are as follows.

Li et al. (2011a) put constraints on the progenitor using the pre-explosion images taken by the Hubble Space Telescope (HST). Their constraints excluded the possibilities of a red giant and a main sequence star with $> 3.5 M_{\odot}$.

Nugent et al. (2011) and Bloom et al. (2012) limited the radius of the exploding object as $< 0.1 R_{\odot}$ using the early observational data. Moreover, they ruled out a red giant and massive main sequence as the companion star using the ejecta-companion interaction model of Kasen (2010). Brown et al. (2012a) observed the early UV lightcurve of SN 2011fe and excluded even

¹⁶They also found that the early lightcurve behavior observed in SN 2014J (e.g., Goobar et al., 2014) might be result of the ejecta-companion interaction.

1 M_{\odot} main sequence as the companion. These constraints might be critical for the DD model because according to some hydrodynamical simulations, a DD merger scatters CSM extending $> 0.1 R_{\odot}$ before its SN explosion (e.g., Fryer et al., 2010; Tanikawa et al., 2015). Nugent et al. (2011) argued that an SN Ia arising from the DD model might show similar emission to the signature of the ejecta-companion interaction in the SD model.

Shappee et al. (2013) and Graham et al. (2015) searched $H\alpha$ emission lines from the matter stripped from the companion in the nebular phase spectra of SN 2011fe, and limited the stripped mass $< 0.001 M_{\odot}$, which was significantly lower than a theoretical prediction of Marietta et al. (2000). Their constraints ruled out a red giant and main sequence star as the companion.

Margutti et al. (2012) estimated the amount of CSM surrounding SN 2011fe using Swift X-ray Telescope (XRT), and set constraints on possible mass loss rate from the non-degenerate companion as $< 2 \times 10^{-9} M_{\odot} \text{ yr}^{-1}$. Chomiuk et al. (2012) also limited the mass loss rate as $< 2 \times 10^{-9} M_{\odot} \text{ yr}^{-1}$ from their radio observations¹⁷. Their results excluded almost all possible non-degenerate companions filling their Roche lobes.

These observational constraints indicate that the SD systems seem not to be progenitors in some SNe Ia and the DD model might be more likely, especially for SN 2011fe.

Here, we would like to note that there are some sub-scenarios of the SD model which can explain the above observational constraints, e.g., spin-up/down delayed explosion scenario (e.g., Justham, 2011; Di Stefano et al., 2011; Hachisu et al., 2012a; Benvenuto et al., 2015). In that scenario, a CO WD gets angular momentum by accretion from its companion, and might obtain a differential rotation. The WD is supported by its rotation even when its mass exceeds M_{Ch} . Subsequently, the differential rotation of the WD is gradually decreases due to the redistribution of angular momentum by some mechanisms, e.g., hydrodynamical viscosity, magnetic fields, meridional circulation. Then, the rotation support weakens, the WD contracts and increases its central density. Finally, the CO WD would lead to an SN Ia explosion from the central carbon ignition. In such the delayed explosion SD scenario, a non-degenerate companion could evolve to a WD and not be detected at the time of the explosion if the spin-down timescale is sufficiently longer than the lifetime of the companion ($> 10^8 \text{ yr}$)¹⁸. Therefore, the spin-up/down SD scenario might be able to avoid some of the above observational limits, e.g., the absence of companions in the nearby supernova remnant (SNR), non-detection of signatures from SN ejecta-companion interaction (e.g., Di Stefano and Kilic, 2012).

The delay time distribution (DTD) of SNe Ia is one of possible indicators for SN Ia progenitor models (e.g., Yungelson and Livio, 2000; Greggio, 2005). The DTD is the time distribution of SN Ia rate after a bursting star formation. In the DD model, the DTD could be estimated from the orbital

¹⁷Both of them assumed the wind velocity of 100 km s^{-1}

¹⁸This scenario could also explain the super-Chandrasekhar SNe Ia, whose masses are considered to exceed M_{Ch} (e.g., Hachisu et al., 2012a; Hachisu et al., 2012b), because differentially rotating WDs is considered to be able to support the larger mass than M_{Ch} (e.g., Hachisu, 1986; Yoon and Langer, 2004; Yoon and Langer, 2005).

separation a distribution of double WD binaries immediately after common envelope phase, $dN/da \propto a^\alpha$, and the dependence of merging time on a , $t_{\text{merge}} \propto a^\gamma$, after the production of CO WDs ceases, i.e., the lifetime of stars with $\sim 2 M_\odot$, about 1 Gyr from the star burst. Then, the DTD is estimated as $\propto t^\beta$, where $\beta = -1 + (1 + \alpha)/\gamma$. Here, $\gamma = 4$ for angular momentum loss by gravitational wave radiation. Though α would be given by a binary population synthesis, it has some uncertainties. However, since $\gamma = 4$, the effect from the separation distribution becomes relatively small, and the DTD would be $\sim t^{-1}$ as long as γ is sufficiently large¹⁹.

Totani et al. (2008) derived observational DTD of SNe Ia ranging 0.1 \sim 10 Gyr by observing SNe Ia in the local elliptical galaxies, and found a good agreement with t^{-1} distribution. Thus, they considered that the contribution from the DD progenitors were dominant.

On the other hand, the DTD predicted in the SD model could not produce t^{-1} naturally in several theoretical studies (see Maoz et al., 2014, and references therein), although Hachisu et al. (2008b) succeeded reproducing the theoretical DTD being consistent with the observations by adopting the optically thick winds blown off from an accreting WD and stripping mass from the companion.

One of the direct evidence of the DD model is detection of a DD binary which has the mass exceeds M_{Ch} and merges within the Hubble time. Santander-García et al. (2015) recently claimed that there would be a super-Chandrasekhar double WD binary in the center of Henize 2-428, a bipolar planetary nebula. According to their observations, the DD system could merge within 700 Myr, which is shorter than the Hubble time. It is the first detection of possible progenitors of the DD model if their interpretation is correct²⁰.

From above discussion, although the definitive conclusion has not existed yet, there are some observational clues preferring to the DD model²¹.

1.3.2 Theoretical studies

Single degenerate model

In the SD model, one of the most important problems is whether a CO WD could accrete matter from its non-degenerate companion with keeping stable hydrogen burning (e.g., Nomoto, 1982a). If its accretion rate keeps the consumption rate of hydrogen by nuclear burning, hydrogen burns stably and the CO WD could grow its mass up to nearly M_{Ch} , finally explode as an SN Ia. On the other hand, if the accretion rate exceeds the upper boundary for stable hydrogen burning, \dot{M}_{cr} , matter from the companion are not

¹⁹Some BPS calculations showed more complex separation distribution at post-common envelope than a simple power law, and the derived DTD of the DD model deviates from t^{-1} (e.g., Yungelson and Kuranov, 2017).

²⁰According to Badenes and Maoz (2012), such super-Chandrasekhar DD systems in our Galaxy seem to be too rare to explain the entire Galactic SNe Ia. This is one of the shortcomings of the DD model in the observational studies. We will go back to this issue in Section 4

²¹There are several possible evidences supporting the SD progenitors, too.

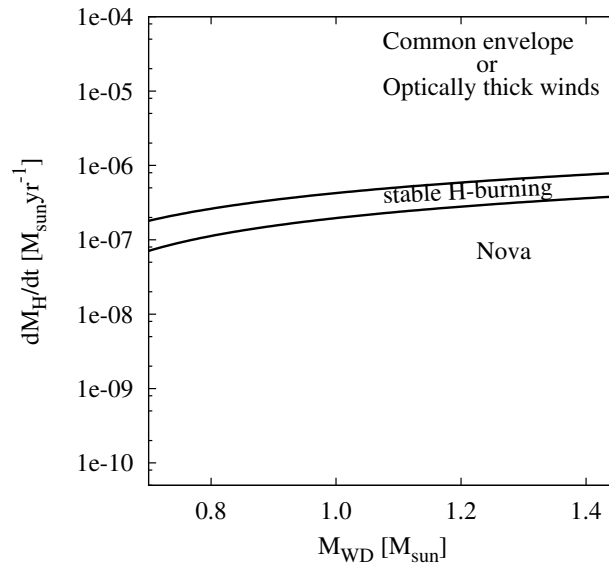


FIGURE 1.6: The range of mass accretion rate keeping stable hydrogen burning. The upper black solid line depicts the upper bound for stable hydrogen burning \dot{M}_{cr} , while the lower one does the lower bound \dot{M}_{stable} . As long as the accretion rate lies between them, a CO WD can accumulate matter from its companion stably and increase its mass to M_{Ch} . Here, we adopt the formulae of Kato et al. (2014) for \dot{M}_{cr} and \dot{M}_{stable} .

completely consumed and expands consequently. Due to expanding matter, the accreting WD becomes a red giant-like structure, and, as a result, the system would go into the common envelope phase. In the common envelope phase, because the system shrinks its orbital separation and blow off its envelope by using the orbital energy, they would finally merge or form a DD system.

If the accretion rate goes below the lower limit, \dot{M}_{stable} , hydrogen burning ceases, the accreted matter piles up on the WD surface and get cold. When the mass of accreting matter exceeds the critical value, a hydrogen burning flash ignites and all accreting matter is ejected. This is the same as a nova explosion. Because the WD matter is dredged up to the envelope by convection, a part of the WD matter is ejected and the mass of WD possibly decreases at the nova explosion. Therefore, the WD could not increase its mass and lead to an SN Ia.

When the mass accretion rate stays at the value between \dot{M}_{cr} and \dot{M}_{stable} , stable hydrogen burning is going on and the WD can get mass from its companion stably. As shown in Figure 1.6, the range of stable hydrogen burning is narrow, about $10^{-7\sim-6} M_{\odot} \text{yr}^{-1}$. Here, we derive the formulae of \dot{M}_{cr} and \dot{M}_{stable} from Equations 4 and 5 in Kato et al. (2014), which are described as

$$\dot{M}_{\text{stable}} = 4.17 \times 10^{-7} \left(\frac{M}{M_{\odot}} - 0.53 \right) M_{\odot} \text{yr}^{-1}, \quad (1.2)$$

$$\dot{M}_{\text{cr}} = 8.18 \times 10^{-7} \left(\frac{M}{M_{\odot}} - 0.48 \right) M_{\odot} \text{yr}^{-1}, \quad (1.3)$$

where M is the mass of an accreting WD. In the range of accretion rate, the WD would be observed as a super soft X-ray source (e.g., van den Heuvel et al., 1992). However, several observations suggested that the number of such SSXSs might be too small to explain the majority of SNe Ia along the SD model (e.g., Gilfanov and Bogdán, 2010; Di Stefano, 2010).

Hachisu et al. (1996) and Hachisu et al. (1999) proposed that an SD system could avoid forming common envelope despite its accretion rate exceeding \dot{M}_{cr} by optically thick winds from the accreting WD driven by its nuclear burning luminosity (e.g., Kato and Hachisu, 1994). Such strong winds eject extra-matter which can not be consumed by nuclear burning, suppress high accretion rate by stripping outer mass of the companion (see also Hachisu et al., 2008a). As a result, a self-regulation mechanism maintaining mass accretion rate close to \dot{M}_{cr} works, and various SD systems might be able to lead to SNe Ia. Moreover, the winds would reduce the soft X-ray emission from the accreting WD by absorption, so provide a possible solution of the paucity of SSXSs (e.g., Hachisu et al., 2010)²².

Because there have been large theoretical uncertainties yet, we can not have the definitive conclusion whether the SD model could explain the entire SNe Ia.

Double degenerate model

In theoretical studies, some difficulties have been presented for the DD model. After double CO WD binaries merge, the disrupted secondary (less massive) WD falls onto the primary (more massive) WD. Due to high mass accretion rate (nearly the Eddington accretion limit), off-center carbon burning ignites. The carbon burning flames propagate into the center of the primary CO WD, and convert it into an oxygen-neon-magnesium (ONeMg) WD (e.g., Nomoto and Iben, 1985; Saio and Nomoto, 1985; Saio and Nomoto, 1998; Saio and Nomoto, 2004). When the mass of the ONeMg WD exceeds M_{ig} , electron capture on Ne and Mg occurs and the pressure at the center decreases. At last, the WD gravitationally collapses to a neutron star (NS) instead of exploding as an SN Ia (accretion induced collapse, AIC, Nomoto and Kondo, 1991).

Benz et al. (1990) firstly performed three-dimensional (3D) simulations of double CO WD mergers, using their smoothed particle hydrodynamics (SPH) code (e.g., Gingold and Monaghan, 1977; Lucy, 1977), although their simulations had only low resolutions (a few thousands particles) due to the computational capability. Recently, owing to the improvement of numerical performance, many studies have performed 3D SPH simulations of binary WD mergers with high resolutions ($> 10^5$ particles). Such simulations and studies showed the possibilities of SN Ia explosion in the DD model.

The DD mergers can be divided into several sub scenarios by the dynamical phases when an SN Ia explosion occurs. We introduce them in the time-series order. At first, if the accretion of the secondary WD onto the primary is violent enough to initiate carbon detonation at the surface of the primary, an explosion occurs during the merger, i.e., the dynamical merger

²²Di Stefano (2010) proposed winds from a companion star as the possible mechanism hiding the soft X-ray emission of SSXSs.

phase. This phase corresponds to < 100 s after the start of the Roche lobe over flow (RLOF) of the secondary. As mentioned above, such successful explosion model is called the violent merger scenario (e.g., Pakmor et al., 2010).

If carbon detonation does not occur during the merger phase, the secondary is completely disrupted and surrounds the primary. Kashyap et al. (2015) found that the spiral instability is generated in the surrounding matter and it prompts the matter to rapidly fall onto the primary, and as a result, carbon detonation occurs. They showed that the detonation waves finally blow off the system and the explosion would be observed as an SN Ia. They called this mechanism the spiral instability model, although they performed only the very massive model of $1.1 + 1.0 M_{\odot}$.

When the violent merger and the spiral instability failed, the merger system approaches gradually a quasi-stationary, axisymmetric configuration, and forms a merger remnant at last. We call this phase the early remnant phase, about $100 \sim 1000$ s after the secondary is completely disrupted (e.g., Shen et al., 2012; Kashyap et al., 2015).

Many studies simulating mergers of WDs have shown that the merger remnants consist of three components. They are the cold core mainly composed of the primary, the hot envelope and rotational disk, both of which are composed of the disrupted secondary. The hot envelope has high temperature and is supported by heat pressure and centrifugal force by its rapid rotation.

The merger remnant goes to the viscous evolution phase, $10^4 \sim 10^8$ s after the merger (e.g., Schwab et al., 2012; Shen et al., 2012; Ji et al., 2013). In this phase, the merger remnant evolves in the viscous timescale. Angular momentum of the hot envelope is transferred by physical viscosity, e.g., magnetic fields. Matter of the envelope gradually accrete onto the cold core and increase the temperature and density of the envelope by compression. If the angular momentum of the hot envelope is efficiently removed by the viscosity, mass accretion rate onto the core becomes high enough to ignite central carbon burning in some cases, e.g., mergers of WDs with equal masses (van Kerkwijk et al., 2010). van Kerkwijk et al. (2010) suggested that such systems can explode as an SN Ia even if their total masses are below M_{Ch} .

The next phase is the thermal evolution phase, which is $> 10^3$ years (e.g., Saio and Nomoto, 1985; Yoon et al., 2007; Shen et al., 2012). Accretion of the hot envelope still continues during this phase, and mass of the core gradually increases. When the core's mass exceeds M_{ig} , central carbon burning ignites and an SN Ia explosion would occur. This explosion mechanism is the classical DD model (Iben and Tutukov, 1984; Webbink, 1984), and we call it the accretion induced explosion (AIE) scenario.

If temperature of the hot envelope is high enough to ignite off-center carbon burning during the three phases after the formation of a merger remnant, quiescent carbon burning is initiated near the boundary between the hot envelope and the cold core, and burning flames propagate into the center of the core. The cold core, which is composed of C and O firstly, is converted to ONeMg core by the burning flames (e.g., Nomoto and Iben, 1985; Saio and Nomoto, 1985; Saio and Nomoto, 1998; Saio and Nomoto, 2004). Finally, the merger system would collapse to an NS when the mass

of the core exceeds M_{ig} , i.e., the AIC scenario (e.g., Nomoto and Kondo, 1991).

If the total mass of the system is less massive than M_{ig} , an ONeMg WD would be formed. If neither carbon detonation during the dynamical merger phase nor off-center carbon burning in the hot envelope occurs, the CO WD merger would result in the formation of a single massive CO WD. We summarize the timescales of each phase in Table 1.2.

Dynamical phase	timescale (s)
Dynamical merger phase	$< 10^2$
Early remnant phase	$10^2 \sim 10^3$
Viscous evolution phase	$10^4 \sim 10^8$
Thermal evolution phase	$> 10^{10}$

TABLE 1.2: Summary of the evolutionary phases of CO WD mergers and the corresponding timescales in seconds.

1.4 Aim of this thesis

Here, we describe previous studies and aim of our study. We briefly summarize numerical configurations of those studies in Table 1.3. This thesis uses almost same configurations as Sato et al. (2015) and Sato et al. (2016).

Yoon et al. (2007) performed 3D SPH simulations of CO WD mergers of $0.9 + 0.6 M_{\odot}$, with $\sim 2 \times 10^5$ particles, and followed further evolution of its merger remnant using 1D stellar evolution code. They found that the primary could increase its mass accreting matter of the disrupted secondary without off-center carbon burning when several conditions are satisfied. In those cases, the primary approaches M_{Ch} and the merger remnant would explode as an SN Ia at last.

Pakmor et al. (2010) and Pakmor et al. (2011) simulated mergers of CO WDs having $\sim 0.9 M_{\odot}$, with $\sim 2 \times 10^6$ particles. In some of their simulations, the disrupted secondary violently accretes onto the primary, increases its density and temperature by compression, and ignites carbon detonation at the surface of the primary during the dynamical merger. The detonation waves propagate through, and blow off the merger system. They called this explosion mechanism the violent merger scenario. They also performed simulations of nucleosynthesis and radiative transfer using the results of their merger simulations, and showed that such explosions would be able to explain light curves and spectra of subluminous and fast-decay SNe Ia populations, SN 1991bg-like events (e.g., Filippenko et al., 1992b; Leibundgut et al., 1993).

Pakmor et al. (2012a) performed merger simulations of more massive model ($1.1 + 0.9 M_{\odot}$), and showed that it can reproduce typical observational features of normal SNe Ia. In this way, recent theoretical studies including above ones indicate theoretical possibilities of CO WD mergers leading to an SN Ia, i.e., the DD scenario would be one of possible progenitor scenarios of SNe Ia.

However, detailed conditions of mergers leading to an SN Ia are still uncertain. In particular, mass range of merging CO WDs for successful SN Ia explosions is one of the most important issues in the progenitor problem of SNe Ia. For examples, in the violent merger scenario, if carbon detonation waves initiate and propagate through the primary CO WD with converting it to radioactive nickels, an SN Ia-like explosion would occur even if a total mass of a merging CO WD binary does not exceed M_{Ch} .

In this study, we performed 3D SPH simulations of mergers of CO WD binaries with very wide mass range ($0.5 \sim 1.1 M_{\odot}$), high resolution up to $500k$ particles per 1 solar mass (here, $k = 1,024$), and plausible initial conditions.

Although some previous studies have already performed similar parameter surveys (Dan et al., 2012; Dan et al., 2014; Zhu et al., 2013), their simulations had a few shortcomings. For examples, Dan et al. (2012) and Dan et al. (2014) had only very low resolutions $\sim 4 \times 10^4$ particles, and Zhu et al. (2013) had lower resolution $\sim 2 \times 10^5$ than ours and adopted approximate initial conditions (see also Section 2.3.2). As discussed later, numerical resolution and initial condition are very important for results of merger simulations (see also, Dan et al., 2011; Pakmor et al., 2012b; Sato et al., 2015; Sato et al., 2016; Tanikawa et al., 2015).

Using results of our simulations, we derive a relation between mass combinations of merging CO WDs and merger outcomes, especially, the mass range leading to an SN Ia. In our study, we focus our interests on four sub scenarios of the DD scenario, that is (1) the violent merger, (2) AIE, (3) AIC, (4) formation of a massive CO WD. As mentioned later, our SPH simulations of CO WD mergers are insufficient to identify whether a merger system leads to the AIE or AIC. When you interpret our results and discussion represented in this thesis, you have to mind that. Using the derived relation, we estimate ratio of DD mergers leading to SNe Ia to the entire WD mergers, perform comparisons with previous studies, and predict the final fate of the central binary system of Henize 2-428.

This thesis is organized as follows. In Chapter 2, we summarize our numerical methods. Chapter 3 shows results of our simulations and we discuss them in Chapter 4. Finally, we present summary and conclusions of this thesis in Chapter 5. In this thesis, we reprint some of figures published in Sato et al. (2015) and Sato et al. (2016) under the permission from the IOPscience.

Refs.	EOS	N.R.	I.C.	Mass(M_{\odot})	Reso.(M_{\odot}^{-1})
Benz et al., 1990	Chandrasekhar, 1939	No	approximate	1.2 + 0.9	$\sim 3 \times 10^3$
Guerrero et al., 2004	mixed ¹	Yes	approximate	0.8 + 0.6, 1.0 + 0.6, 1.0 + 0.8	$\sim 3 \times 10^4$
Yoon et al., 2007	Timmes and Arnett, 1999	Yes	approximate	0.9 + 0.6	$\sim 1.3 \times 10^5$
Lorén-Aguilar et al., 2009	mixed ¹	Yes	approximate	0.5 + 0.3, 0.6 + 0.6, 0.8 + 0.4, 0.8 + 0.6, 1.2 + 0.6	$\sim 4 \times 10^5$
Pakmor et al., 2010,2011	Timmes and Swesty, 2000	Yes	approximate	0.9 + 0.9 \sim 0.7	$\sim 10^6$
Dan et al., 2011	Timmes and Swesty, 2000	Yes	synchronized	many ²	$2 \times 10^4, 10^5$
Raskin et al., 2012	Timmes and Swesty, 2000	Yes	synchronized	many ³	5×10^5
Pakmor et al., 2012a	Timmes and Swesty, 2000	Yes	synchronized	1.1 + 0.9	10^6
Dan et al., 2012,2014	Timmes and Swesty, 2000	Yes	synchronized	0.2 \sim 1.2 + 0.2 \sim 1.05	2×10^4
Zhu et al., 2013	Timmes and Swesty, 2000	No	approximate	many ⁴	2×10^5
Sato et al., 2015,2016	Timmes and Swesty, 2000	No	synchronized	0.5 \sim 1.1 + 0.5 \sim 1.1	$10^4 \sim 5 \times 10^5$

TABLE 1.3: A summary of numerical configurations of recent simulations of mergers of double WD binaries. Ref., EOS, N.R., I.C., Reso. are references, equation of state, nuclear reaction, initial condition, resolution (number of particles per 1 solar mass). The details of "approximate" and "synchronized" in the I.C. terms are described in Section 2.3.2.

¹ideal gas + fermi pressure + radiation

²0.3 + 0.2, 0.4 + 0.3, 0.6 + 0.3, 0.67 + 0.45, 0.8 + 0.2, 0.9 + 0.45, 0.9 + 0.6, 1.1 + 0.3, 1.2 + 0.5, 1.2 + 0.9

³0.64 + 0.64, 0.81 + 0.81, 0.96 + 0.64, 0.96 + 0.81, 0.96 + 0.96, 1.06 + 0.64, 1.06 + 0.81, 1.06 + 0.96, 1.06 + 1.06

⁴The combinations in 0.4, 0.5, 0.55, 0.6, 0.65, 0.7, 0.8, 0.9, 1.0, and 0.65 + 0.575, 0.65 + 0.625, 0.65 + 0.64

Chapter 2

Numerical Methods

In this Chapter, we describe a brief explanation of SPH, summary of our numerical configuration, and initial setup of our simulations.

2.1 Overview of SPH

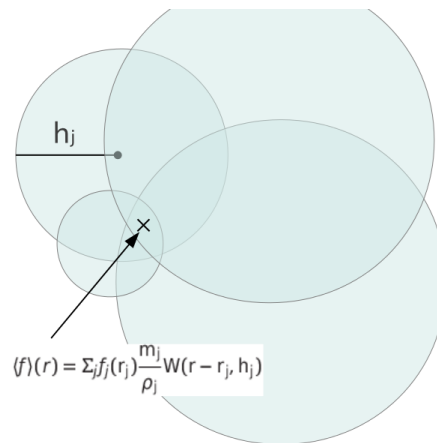


FIGURE 2.1: A schematic figure of SPH. Physical quantities of fluid are described by superposition of SPH particles having spatial extents. f , h , $W(r, h)$ are a physical quantity, smoothing length, and kernel function, respectively.

Smoothed particle hydrodynamics (SPH) is the Lagrangian mesh-free particle method to describe fluid phenomena. In this scheme, fluids are expressed as aggregate of SPH particles having spatial width, which are similar to fluid elements. Physical parameters of fluids are given by superposition of those of particles. We represent a simple schematic picture of SPH in Figure 2.1. SPH was developed for treating astrophysical fluid phenomena, e.g., fission of protostar (e.g., Lucy, 1977; Gingold and Monaghan, 1977). It is now used in various fields, not only astrophysics. Merits of using the SPH scheme to simulate mergers of CO WDs binaries are follows. (1) The conservation of mass, energy, angular momentum are achieved well by its formulation. (2) Spatial resolution is optimized automatically. For example, a large number of SPH particles exist in a dense region, such like a core of a star. On the other hand, a sparse region has only a small number of particles. If we try to implement such a mechanism adjusting spatial resolutions into a finite difference method, we need a more complicated one such like the Adaptive mesh refinement (AMR). (3) It is easy to implement

a multi-dimensional hydrodynamic code.

t	time	h	smoothing length
\mathbf{r}	position	ρ	density
\mathbf{v}	velocity	P	pressure
$\boldsymbol{\Omega}$	angular velocity	u	specific internal energy
m	mass	α	viscosity coefficient
h	smoothing length	Δt	timestep

TABLE 2.1: Definitions of variables using in this Chapter.

There are several formulations for SPH. Recent good reviews of SPH present details of them (e.g., Monaghan, 2005; Rosswog, 2009). In this study, we use a formulation called the "vanilla ice" SPH formulation in Rosswog (2009). Here, we describe our formulation briefly. Definitions of variables using here are shown in Table 2.1. Numerical subscripts indicate IDs of SPH particles. For example, m_i means mass of i -th particle. In this thesis, we define scalar and vector variables having two subscripts, e.g., A_{ij} and \mathbf{B}_{ij} , as

$$A_{ij} = \frac{1}{2}(A_i + A_j)$$

$$\mathbf{B}_{ij} = \mathbf{B}_i - \mathbf{B}_j.$$

Basic equations which we have to solve are the equation of continuity, equation of motion, and energy equation. We write down their Lagrangian formulations here.

$$\frac{d\rho}{dt} = -\rho(\nabla \cdot \mathbf{v}) \quad (2.1)$$

$$\frac{d\mathbf{v}}{dt} = -\frac{\nabla P}{\rho} + \mathbf{F} \quad (2.2)$$

$$\frac{du}{dt} = -\frac{P}{\rho}(\nabla \cdot \mathbf{v}) + S \quad (2.3)$$

\mathbf{F} is a body force, e.g., self-gravity, and S is a source term, e.g., nuclear reaction, neutrino cooling. Given the equation of state (EOS), we can solve them.

SPH describes fluids as the aggregate of particles, i.e., discretizes continuum. We consider a SPH particle having its mass m_i and spatial width h called smoothing length. Mass density of fluid is expressed as distribution of SPH particles.

$$\rho(\mathbf{r}) = \sum_i m_i W(\mathbf{r} - \mathbf{r}_i, h) \quad (2.4)$$

$W(\mathbf{r} - \mathbf{r}_i, h)$ is a kernel function which indicate spatial extent of a SPH particle. This function is spherically symmetric and has features described as

$$\lim_{r \rightarrow \infty} W(\mathbf{r}, h) = 0 \quad (2.5)$$

$$\lim_{h \rightarrow 0} W(\mathbf{r}, h) = \delta(\mathbf{r}) \quad (2.6)$$

$$\int W(\mathbf{r}, h) d\mathbf{r}^3 = 1. \quad (2.7)$$

Using these features, we can get total mass of the fluid as

$$M_{\text{tot}} = \int \rho(\mathbf{r}) d\mathbf{r}^3 = \sum_i m_i \int W(\mathbf{r} - \mathbf{r}_i, h) d\mathbf{r}^3 = \sum_i m_i.$$

The total mass of fluid is conserved in SPH simulations from this formulation. In this study, we adopt a third-ordered spline kernel function as $W(\mathbf{r}, h)$.

$$W(\mathbf{r}, h) = \frac{1}{\pi h^3} \begin{cases} 1 - \frac{3}{2}\hat{r}^2 + \frac{3}{4}\hat{r}^3 & (0 \leq \hat{r} \leq 1) \\ \frac{1}{4}(2 - \hat{r})^3 & (1 < \hat{r} \leq 2) \\ 0 & (\hat{r} > 2) \end{cases} \quad (2.8)$$

Here, $\hat{r} \equiv |\mathbf{r}|/h$. Because a derivative of Equation 2.8 approaches zero when distance between particles becomes smaller, pressure gradient which is proportional to $\nabla W(\mathbf{r}, h)$ become smaller. As a result, numerical concentration of particles occurs (pairing instability). We prevent this instability by adopting a formulation of Thomas and Couchman (1992), that is,

$$\nabla W(\mathbf{r}, h) = \frac{-1}{\pi h^3} \begin{cases} 1 & (0 \leq \hat{r} \leq \frac{2}{3}) \\ \frac{3}{4}\hat{r}(4 - 3\hat{r}) & (\frac{2}{3} < \hat{r} \leq 1) \\ \frac{3}{4}(2 - \hat{r})^2 & (1 < \hat{r} \leq 2) \\ 0 & (\hat{r} > 2). \end{cases} \quad (2.9)$$

Using the kernel function $W(\mathbf{r}, h)$, we describe distribution of a physical value $f(\mathbf{r})$ in SPH as

$$\begin{aligned} \tilde{f}(\mathbf{r}) &= \int f(\mathbf{r}') W(\mathbf{r} - \mathbf{r}', h) d^3 \mathbf{r}' \\ &= \int \frac{f(\mathbf{r}')}{\rho(\mathbf{r}')} W(\mathbf{r} - \mathbf{r}', h) \rho(\mathbf{r}') d^3 \mathbf{r}'. \end{aligned} \quad (2.10)$$

Its discretized formulation is

$$\tilde{f}(\mathbf{r}) \sim \sum_i \frac{m_i}{\rho(\mathbf{r}_i)} f(\mathbf{r}_i) W(\mathbf{r} - \mathbf{r}_i, h). \quad (2.11)$$

We use an approximation $\rho(\mathbf{r}')d^3\mathbf{r}' \sim m_i$, and replace integral with summation to convert Equation 2.10 to Equation 2.11. Derivative of f is

$$\begin{aligned}\widetilde{\nabla}f(\mathbf{r}) &= \int \nabla' f(\mathbf{r}')W(\mathbf{r} - \mathbf{r}', h)d^3\mathbf{r}' \\ &= - \int f(\mathbf{r}')\nabla'W(\mathbf{r} - \mathbf{r}', h)d^3\mathbf{r}' \\ &= \int f(\mathbf{r}')\nabla W(\mathbf{r} - \mathbf{r}', h)d^3\mathbf{r}'.\end{aligned}\quad (2.12)$$

Using Equation 2.4, we can derive

$$\sum_i \frac{m_i}{\rho(\mathbf{r})}W(\mathbf{r} - \mathbf{r}_i, h) = 1. \quad (2.13)$$

Combining Equation 2.12 and 2.13,

$$\begin{aligned}\widetilde{\nabla}f(\mathbf{r}) &= \sum_i m_i \int \frac{f(\mathbf{r}')}{\rho(\mathbf{r}')}W(\mathbf{r}' - \mathbf{r}_i, h)\nabla W(\mathbf{r} - \mathbf{r}', h)d^3\mathbf{r}' \\ &\sim \sum_i m_i \frac{f(\mathbf{r}_i)}{\rho(\mathbf{r}_i)}\nabla W(\mathbf{r} - \mathbf{r}_i, h).\end{aligned}\quad (2.14)$$

Here, we use an approximation $W(\mathbf{r}' - \mathbf{r}_i, h) \sim \delta(\mathbf{r}' - \mathbf{r}_i)$ assuming h is much smaller than a size of the system.

We transfer the basic equations, Equation 2.2, 2.3, to their SPH formulations. Using Equation 2.11, 2.13, 2.14, their formulations are discretized as

$$\frac{d\mathbf{v}_i}{dt} = -\frac{1}{\rho_i} \sum_j \frac{m_j}{\rho_j} P_j \nabla_i W(\mathbf{r}_{ij}, h) \quad (2.15)$$

$$\frac{du_i}{dt} = \frac{P_i}{\rho_i^2} \sum_j m_j \frac{d}{dt} W(\mathbf{r}_{ij}, h). \quad (2.16)$$

Here, we ignore \mathbf{F} and S for simplicity. Since the mass conservation is automatically satisfied in SPH, we have not to solve the equation of continuity.

Because these formulations do not satisfy the law of action and reaction, the total (angular) momentum does not conserve. For example, we consider balance between i -th particle and j -th one. Hydrodynamical force from j -th particle to i -th one is

$$\mathbf{G}_{ji} = -\frac{m_i}{\rho_i} \frac{m_j}{\rho_j} P_j \nabla_i W(\mathbf{r}_{ij}, h).$$

On the other hand, that from i to j is

$$\begin{aligned}\mathbf{G}_{ij} &= -\frac{m_j}{\rho_j} \frac{m_i}{\rho_i} P_i \nabla_j W(\mathbf{r}_{ji}, h) \\ &= \frac{m_i}{\rho_i} \frac{m_j}{\rho_j} P_i \nabla_i W(\mathbf{r}_{ij}, h).\end{aligned}$$

You should note that $\mathbf{G}_{ji} \neq -\mathbf{G}_{ij}$ because $P_i \neq P_j$ in general. We have to make a term of pressure gradient in Equation 2.2 symmetric for i and j ,

like,

$$\frac{\nabla P}{\rho} = \nabla \left(\frac{P}{\rho} \right) + P \frac{\nabla \rho}{\rho^2}.$$

Using this expression, we derive

$$\frac{d\mathbf{v}_i}{dt} = - \sum_j m_j \left(\frac{P_i}{\rho_i^2} + \frac{P_j}{\rho_j^2} \right) \nabla_i W(\mathbf{r}_{ij}, h) + \mathbf{F}_i. \quad (2.17)$$

Assuming that all particles have an equal mass, the above formulation is symmetric for i and j when we ignore \mathbf{F}_i . In our simulations, each particles has a different smoothing length h_i . We replace h in $W(\mathbf{r}_{ij}, h)$ with h_{ij} for the symmetry of Equation 2.17 (Rosswog, 2009).

We also modify the energy equation using

$$\begin{aligned} \frac{dW(\mathbf{r}_{ij}, h)}{dt} &= \frac{d\mathbf{r}_{ij}}{dt} \cdot \frac{\partial W(\mathbf{r}_{ij}, h)}{\partial \mathbf{r}_{ij}} \\ &= \mathbf{v}_{ij} \cdot \frac{\partial W(\mathbf{r}_{ij}, h)}{\partial \mathbf{r}_i} \\ &= \mathbf{v}_{ij} \cdot \nabla_i W(\mathbf{r}_{ij}, h). \end{aligned}$$

Equation 2.16 is modified as

$$\frac{du_i}{dt} = \frac{P_i}{\rho_i^2} \sum_j m_j \mathbf{v}_{ij} \cdot \nabla_i W(\mathbf{r}_{ij}, h) + S_i. \quad (2.18)$$

Equation 2.17 and 2.18 are the basic equations in SPH.

2.2 Numerical configuration

We summarize numerical configurations of our simulations in this Section.

2.2.1 Numerical code and computational environment

Our numerical code is "OcTree On OpenCL"(OTOO) code, which was developed to perform particle simulations of various astrophysical hydrodynamical phenomena (Nakasato et al., 2012). OTOO implements the octree method (Barnes and Hut, 1986) to rapidly calculate interactions of particles, e.g., gravity and SPH neighbor particles. This code is optimized for computational environment with multiple CPU and GPU cores to utilize heterogeneous resources efficiently. Due to using OpenCL, machine-dependence of OTOO code is relatively low.

We perform our simulations on HA-PACS, which is a supercomputer at the Center for Computational Sciences, University of Tsukuba. We utilize a single node of HA-PACS for our simulations, and a single node has two CPUs and four GPUs.

2.2.2 Gravity

We calculate gravity acting on i -th particle as superposition of that from all particles. Its formulation is

$$\mathbf{g}_i = - \sum_j \frac{Gm_i m_j \mathbf{r}_{ij}}{(|\mathbf{r}_{ij}|^2 + \epsilon^2)^{3/2}}, \quad (2.19)$$

where G is the gravitational constant, and ϵ is a Plummer softening parameter which avoids numerical divergence. In this study, we fix $\epsilon = 3 \times 10^6$ cm (e.g., Aarseth, 1963). For suppression of numerical costs of calculating gravity, we use the octree method, in which multipole moment of gravity from distant particles are approximated (e.g., Barnes and Hut, 1986). More details are found in Nakasato et al. (2012)

2.2.3 Smoothing length

We determine a smoothing length of i -th particle to keep the number of neighbor particles constant (e.g., Thacker et al., 2000). It is described as

$$h_i(t + \Delta t) = h_i(t)(1 - A + As), \quad (2.20)$$

where Δt is a time step, $s = (N_s/N_i(t))^{1/3}$, N_s and $N_i(t)$ are the average number of neighbor particles and the number of neighbor particles at t , respectively. A is

$$A = \begin{cases} 0.2(1 + s^2) & (s < 1) \\ 0.2(1 + 1/s^3) & (s \geq 1). \end{cases}$$

$N_i(t)$ is calculated as $N_i(t) = \sum_{j \neq i} W_{\text{nn}}(\mathbf{r}_{ij}, h_{ij})$, where W_{nn} is

$$W_{\text{nn}}(\mathbf{r}, h) = \begin{cases} 1 & (0 \leq \hat{r} < 3/2) \\ \pi h^3 W(4(|\mathbf{r}| - 3h/2), h) & (3/2 \leq \hat{r} \leq 2). \end{cases}$$

We set $N_s = 25$ in our simulations, which correspond to keeping the number of neighbor particles about 75 in all the way of simulations.

2.2.4 EOS and Nuclear reaction

We use the Helmholtz EOS of Timmes and Swesty (2000), which includes four pressure components, thermal radiation, ideal gas, electron-positron gas with arbitrary degeneracy, and the coulomb correction effect (Yakovlev and Shyalybkov, 1989). This EOS returns various thermodynamical values when a set of density, temperature, and composition are given. In our simulations, we derive temperature T_i , pressure P_i , sound speed $c_{s,i}$ of i -th particle from its density ρ_i and specific internal energy u_i .

Because ρ_i and u_i have some numerical fluctuations, the derived thermodynamical values also have those. In particular, if nuclear reactions are included in simulations, the fluctuation of temperature would be highly enhanced and might cause unphysical effect on results of simulations (see also

Zhu et al., 2013; Sato et al., 2015; Tanikawa et al., 2015). In order to avoid such effect, and reduce computational costs, we do not include any nuclear reactions in our simulations basically. As mentioned later, we test the effect of inclusion of nuclear reactions by performing several simulations with a simple carbon burning (Section 4.2.2).

We assume uniform chemical composition of CO WDs with 50% carbon and 50% oxygen in mass fraction. This composition does not change in all the way of our simulations due to non-inclusion of nuclear reactions.

2.2.5 Artificial viscosity

In SPH scheme, it is usual to introduce an artificial viscosity Π_{ij} to treat shocks, although there are other methods (e.g., Inutsuka, 2002). We adopt a formulation after Monaghan (1992),

$$\Pi_{ij} = \max(\Pi_{ij,i}, \Pi_{ij,j}) \quad (2.21)$$

$$\Pi_{ij,k} = \begin{cases} \frac{-\alpha_k c_{s,ij} \mu_{ij} + 2\beta_k \mu_{ij}^2}{\rho_{ij}} & (\mathbf{r}_{ij} \cdot \mathbf{v}_{ij} < 0) \\ 0 & (\text{otherwise}) \end{cases} \quad (2.22)$$

$$\mu_{ij} \equiv \frac{h_{ij} \mathbf{v}_{ij} \cdot \mathbf{r}_{ij}}{|\mathbf{r}_{ij}|^2 + 0.01 h_{ij}^2}, \quad (2.23)$$

where α_k and β_k are the viscosity coefficients of k -th particle with a relation as $\beta_k = 2\alpha_k$. We modify α_k as a time-dependent formulation to suppress the artificial viscosity where no shock exists (Morris and Monaghan, 1997). It is,

$$\frac{d\alpha_k}{dt} = -\frac{\alpha_k - \alpha_{\min}}{\tau_k} + \max[-(\nabla \cdot \mathbf{v})_k (\alpha_{\max} - \alpha_k), 0]$$

$$\tau_k \equiv \frac{h_k}{0.25 c_{s,k}},$$

where α_{\min} and α_{\max} are the minimum and maximum of viscosity coefficients. Usually, $\alpha_k = \alpha_{\min}$ in no shock regions. We take $\alpha_{\min} = 0.05$ and $\alpha_{\max} = 1.5$ in our simulations.

We introduce the Balsara switch to shut off the artificial viscosity from shear motions (Balsara, 1995). The formulation is

$$\bar{f}_i = \frac{|(\nabla \cdot \mathbf{v})_i|}{|(\nabla \cdot \mathbf{v})_i| + |(\nabla \times \mathbf{v})_i| + 10^{-4} c_{s,i} / h_i}. \quad (2.24)$$

Now, we rewrite the basic equations 2.17 and 2.18 with adding terms of the artificial viscosity,

$$\frac{d\mathbf{v}_i}{dt} = -\sum_j m_j \left(\frac{P_i}{\rho_i^2} + \frac{P_j}{\rho_j^2} + \bar{f}_{ij} \Pi_{ij} \right) \nabla_i W(\mathbf{r}_{ij}, h) + \mathbf{g}_i \quad (2.25)$$

$$\frac{du_i}{dt} = \frac{P_i}{\rho_i^2} \sum_j m_j \mathbf{v}_{ij} \cdot \nabla_i W(\mathbf{r}_{ij}, h) + \frac{1}{2} \sum_j m_j \bar{f}_{ij} \Pi_{ij} \mathbf{v}_{ij} \cdot \nabla_i W(\mathbf{r}_{ij}, h) (+ \epsilon_{\text{nuc},i}), \quad (2.26)$$

where we replace F_i and S_i with gravity g_i and energy generation by nuclear reactions $\epsilon_{\text{nuc},i}$, respectively. Equation 2.25 and 2.26 are the basic equations which we solve in our SPH simulations.

2.2.6 Time integration

We adopt the second-order leap frog scheme as our time integration method. The hydrodynamical time step Δt_{hyd} is determined as

$$\Delta t_{\text{hyd}} = \min(\Delta t_{\text{hyd},i}) \quad (2.27)$$

$$\Delta t_{\text{hyd},i} = \frac{Ch_i}{h_i(\nabla \cdot \mathbf{v})_i + c_{s,i} + 1.2\alpha_i c_{s,i}}, \quad (2.28)$$

where α_i is the viscosity coefficient of i -th particle, and C is the Courant number. We take $C = 0.3$ in our simulations. We calculate $\Delta t_{\text{hyd},i}$ for each particle and take the minimum of them as the time step.

If other physics with different timescales are included in simulations, the time step is determined by the shortest timescale corresponding to the physics. If nuclear reactions are included, we derive the time step Δt as

$$\Delta t = \min(\Delta t_{\text{hyd}}, \Delta t_{\text{nuc}}), \quad (2.29)$$

where Δt_{nuc} is the time step of nuclear reactions, which is determined as

$$\Delta t_{\text{nuc}} = \min(\Delta t_{\text{nuc},i}) \quad (2.30)$$

$$\Delta t_{\text{nuc},i} = 0.1 \frac{C_{P,i} T_i}{\epsilon_{\text{nuc},i}}. \quad (2.31)$$

Here, $C_{P,i}$ and $\epsilon_{\text{nuc},i}$ are the specific heat at constant pressure and nuclear energy generation rate of i -th particle, respectively.

2.3 Initial setup

We show the way to make the initial conditions of our simulations of CO WD mergers. Since our methods are almost same as those of Rasio and Shapiro (1995), Dan et al. (2011), and Pakmor et al. (2012b), you may also see them.

2.3.1 Single CO WD

At the first step, we produce single CO WD models with each mass. We derive one-dimensional (1D) density profile of a perfect degenerate CO WD model with a uniform temperature 10^6 K, and map SPH particles in 3D as the distributions of their densities and internal energies are consistent with those of the 1D model. In order to reduce numerical noises, we relax SPH particles for ~ 20 s physical times. We ignore evolution of internal energy, and add a damping force to the right hand of Equation 2.25. Our

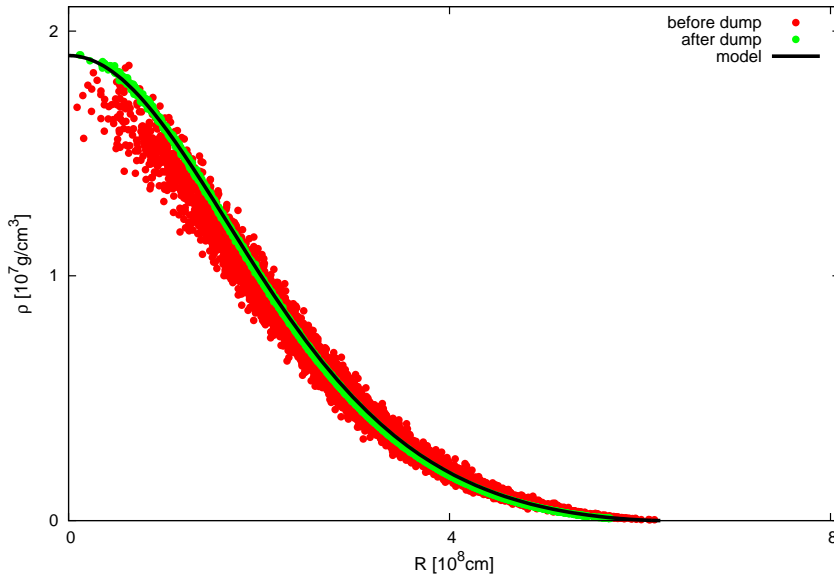


FIGURE 2.2: Example of relaxation for a single $0.9 M_{\odot}$ CO WD. Relaxation produces more accurate density profile (green points) similar to the 1D perfect degenerate one (a black line) than before that (red points). Here, we use a code in [http : //cococubed.asu.edu/code_pages/coldwd.shtml](http://cococubed.asu.edu/code_pages/coldwd.shtml) to produce the 1D density profile of a perfect degenerate CO WD.

formulation of the damping force acting on i -th particle is

$$\left(\frac{d\mathbf{v}_i}{dt}\right)_{\text{damp}} = -\frac{\mathbf{v}_i}{C_{\text{damp}}\Delta t}, \quad (2.32)$$

where Δt of the right hand is the time step, and C_{damp} is an inverse of the relaxation timescale, and we fix $C_{\text{damp}} = 128.0$ in our simulations. Figure 2.2 is the case of a $0.9 M_{\odot}$ CO WD. It shows that the relaxation can reduce numerical noises of SPH particles.

2.3.2 Binary CO WD

Next, we place two single CO WDs which are produced in the way of previous Section 2.3.1 in the same frame, and start the merger. In several previous studies (e.g., Lorén-Aguilar et al., 2009; Zhu et al., 2013), they set initial separation a_{ini} between the primary and secondary in order that the secondary fills its Roche lobe radius, using an approximate formulation of Eggleton (1983),

$$a_{\text{ini}} = \left(\frac{0.49q^{2/3}}{0.6q^{2/3} + \ln(1 + q^{1/3})}\right)^{-1} R_2, \quad (2.33)$$

where R_2 is the radius of the secondary. $q \equiv M_2/M_1$ is mass ratio, where M_1 and M_2 are masses of the primary and secondary respectively. Because the effect of tidal interaction between the primary and secondary is not treated

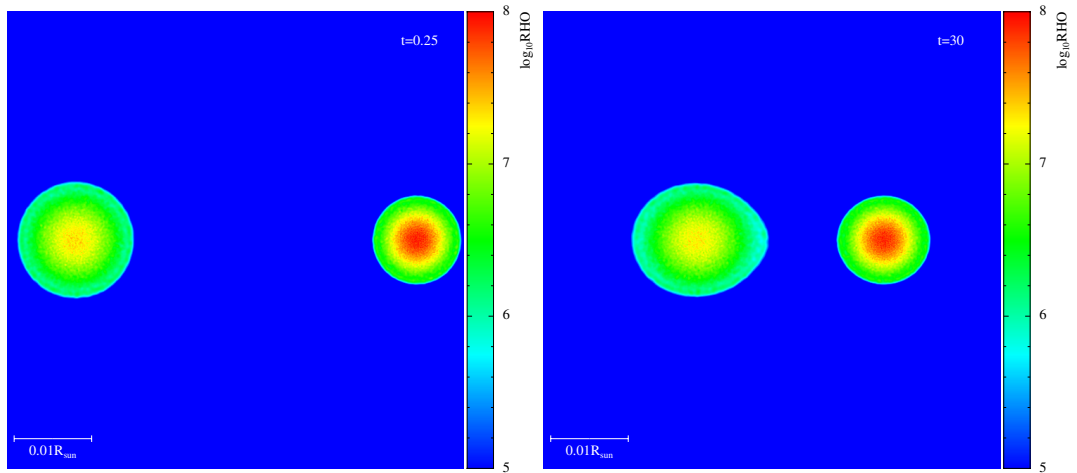


FIGURE 2.3: Density profiles on the x - z plane of $1.1 + 0.9 M_{\odot}$ WDs. The left panel is a profile at the start of relaxation process, and the right is one at the end of that. The secondary WD ($0.9 M_{\odot}$) is deformed by tidal interaction with the primary.

precisely in this formulation, the initial separation would be too small, and mass transfer from the secondary to the primary becomes unphysically unstable (e.g., Dan et al., 2011). We call this initial condition the "approximate" one.

In order to make more plausible initial conditions, we adopt methods proposed by Rasio and Shapiro (1995) and Dan et al. (2011). At first, we set a_{ini} as the Roche lobe radius of the secondary equals to twice as its radius, i.e.,

$$a_{\text{ini}} = \left(\frac{0.49q^{2/3}}{0.6q^{2/3} + \ln(1 + q^{1/3})} \right)^{-1} (2 \times R_2). \quad (2.34)$$

Next, we put the binary system into co-rotation frame under assumption that spins of the primary and secondary synchronize with the binary orbital motion¹. Here, we assume a circular orbit. In that frame, we gradually decrease separation of the binary system by hand, and relax the system introducing the same damping force as Equation 2.32. We solve evolution of internal energy in this relaxation process. As a result, the terms added to the right hand side of Equation 2.25 are

$$\left(\frac{d\mathbf{v}_i}{dt} \right)_{\text{damp}} = -\boldsymbol{\Omega} \times (\boldsymbol{\Omega} \times \mathbf{r}_i) - 2\boldsymbol{\Omega} \times \mathbf{v}_i - \frac{\mathbf{v}_i}{C_{\text{damp}} \Delta t}, \quad (2.35)$$

where $\boldsymbol{\Omega}$ is spin (orbital) angular velocity vector, which derived from the Kepler law for a separation of the binary. We decrease the separation a at

¹On the other hand, the approximate initial conditions usually assume irrotational models, i.e., WDs have no spin.

every Δt_{decay} seconds as

$$\begin{aligned}\Delta a_{\text{decay}} &= \frac{a}{\tau_{\text{decay}}} \Delta t_{\text{decay}}, \\ \tau_{\text{decay}} &= \frac{1}{\epsilon_{\text{decay}} \sqrt{G \bar{\rho}_2}},\end{aligned}\tag{2.36}$$

where $\bar{\rho}_2$ is the average density of the secondary. We adopt $\Delta t_{\text{decay}} = 1/64$ s and $\epsilon_{\text{decay}} = 0.05$. We continue to decrease the separation and relax the system until the RLOF of the secondary starts. Identification of the secondary's RLOF is judged by whether any SPH particles of the secondary satisfy

$$|\mathbf{r}_{2,i} - \mathbf{r}_{L1}| < 0.2R_2,\tag{2.37}$$

where $\mathbf{r}_{2,i}$ is a position vector of i -th SPH particle belonging to the secondary, \mathbf{r}_{L1} is that of L1 Lagrange point, and R_2 is the radius of the secondary. If there are any particles satisfying Equation 2.37, we stop decreasing the separation, and transfer the binary system from the co-rotation frame to a rest one. Figure 2.3 shows the density profiles of $1.1 + 0.9 M_{\odot}$ WDs in the x-z plane, at the start of the relaxation process (left panel), and at the end of that (right panel). You can see that the secondary is highly deformed and elongated by tidal interaction and the secondary's RLOF starts at larger separation than that derived from Equation 2.33. We call this initial condition the "synchronized" one.

Although it is still controversial whether synchronization between spins and orbital motion is achieved by a merger, there are some studies which support that (Marsh et al., 2004; Fuller and Lai, 2014). In this study, we assume that the synchronization can be achieved in all our models. In Section 4.2.2, we compare the results of synchronized models with those of approximate ones.

Resolution dependence of initial condition

N (M_{\odot}^{-1})	a_{ini} (10^9 cm)	P_{orb} (s)	L_{tot} (10^{50} g cm ² s ⁻¹)
10k	1.639	25.58	7.012
50k	1.652	25.88	7.028
100k	1.666	26.22	7.046
500k	1.673	26.39	7.053

TABLE 2.2: Summary of the initial orbital parameters of $1.1 + 0.9 M_{\odot}$ for each numerical resolutions N (M_{\odot}^{-1}). We define $k = 1024$. The orbital separation at the end of our binary setup a_{ini} (10^9 cm), the corresponding orbital period P_{orb} (s), the total angular momentum L_{tot} (10^{50} g cm² s⁻¹).

Table 2.2 shows the orbital parameters of $1.1 + 0.9 M_{\odot}$, the initial binary orbital separations a_{ini} , the initial orbital periods P_{orb} , the total angular momenta L_{tot} , for four different numerical resolutions, 10k, 50k, 100k, 500k

particles per 1 solar mass, where $k = 1024$. We find a general tendency that the values of those parameters increase with their resolution. In other words, the RLOF from the secondary WD to the primary tends to start at larger distance as we increase the numerical resolution. This is because the cases with higher numerical resolution can resolve outer layer of WDs. In our simulations, a mass of a SPH particle is determined as $m_i = M_\odot/N$ and remains constant all the way of the simulation. Thus, larger number of SPH particles can reproduce outer structure of WDs.

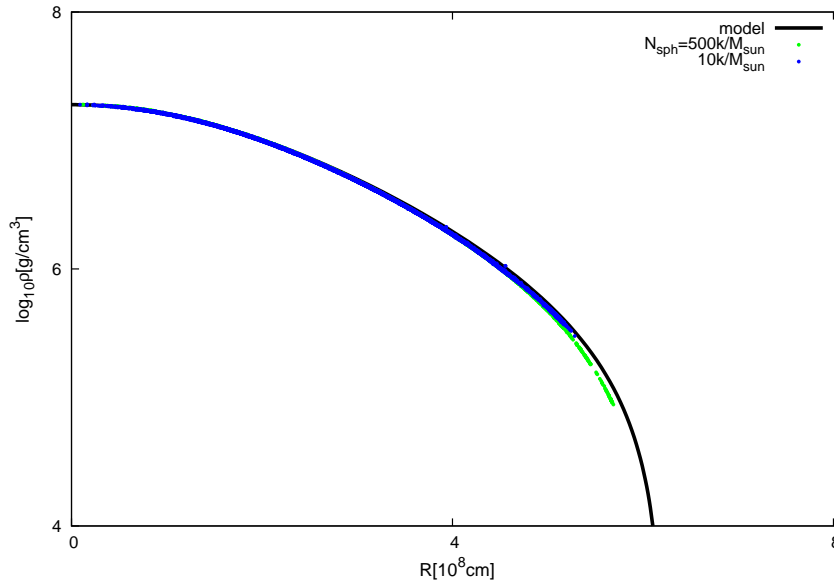


FIGURE 2.4: Density profiles of $0.9 M_\odot$ WD for different resolutions on a logarithmic scale. Blue points represent the case with $10k M_\odot^{-1}$, while green ones are $500k M_\odot^{-1}$. A black solid line shows 1D perfect degenerate WD model, same as Figure 2.2.

Figure 2.4 shows a density profiles of $0.9 M_\odot$ for the cases with $10k M_\odot^{-1}$ (blue points) and $500k M_\odot^{-1}$ (green points). We also present the 1D perfect degenerate CO WD model as a black solid line. We find that the higher resolution model ($500k M_\odot^{-1}$) can reproduce more outer region of the WD than the model of $10k M_\odot^{-1}$. Since a_{ini} is determined where the most outer materials flow out from the Roche lobe of the secondary WD, models in which the more outer region is resolved, i.e., models with higher resolution, have the larger orbital parameters.

The differences of a_{ini} from the numerical resolutions are less than 5% in our study.

Figure 2.5 depicts numerical tendency of the orbital parameters a_{ini} normalized by the values in the cases with $10k M_\odot^{-1}$. We present our results with numerical resolutions ranging $10k \sim 500k M_\odot^{-1}$ for the models of $1.1 + 0.9 M_\odot$, $1.1 + 0.8 M_\odot$, $1.1 + 0.5 M_\odot$, $0.9 + 0.8 M_\odot$, and $0.8 + 0.8 M_\odot$. The general trend discussed above can be confirmed for them. Similar tendencies could be seen in Dan et al. (2011) and Dan et al. (2014)

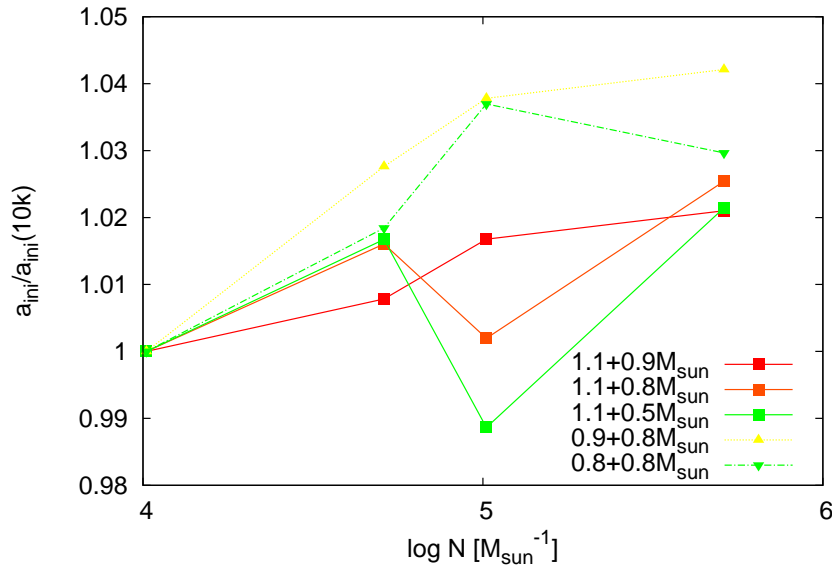


FIGURE 2.5: The numerical dependence of a_{ini} normalized by the values at $10k M_{\odot}^{-1}$, for the mass combinations of $1.1 + 0.9 M_{\odot}$, $1.1 + 0.8 M_{\odot}$, $1.1 + 0.5 M_{\odot}$, $0.9 + 0.8 M_{\odot}$, $0.8 + 0.8 M_{\odot}$.

2.4 Simulation run

The mass range of our CO WD models is $0.5 \sim 1.1 M_{\odot}$, which almost covers the minimum and maximum masses of CO WDs. We simulate mergers of almost 50 CO WD binary models from the start of the secondary's RLOF to the formation of the merger remnant (the end of the early remnant phase, about several hundred seconds after the secondary disruption). In order to investigate dependence of our results on numerical resolution, we perform the same simulations with different numbers of SPH particles, that is $10k$, $50k$, $100k$, $500k$ particles per 1 solar mass, where $k = 1024$. We also performed simulations for a few mass combinations with $1000k$, $2000k$ particles per 1 solar mass.

Chapter 3

Simulation Results

We present results of our SPH simulations of mergers of CO WD binaries. Although we performed merger simulations with several different resolutions (see Section 2.4), we focus on results of our simulations whose numerical resolutions are $500k/M_\odot$ here. Finally, we calculate the ratio of CO WD mergers exploding as SNe Ia to the entire WD mergers, estimate SN Ia rate arising from CO WD mergers in our Galaxy, compare it with observations, and discuss whether or not the DD model could be main progenitors of Galactic SNe Ia.

We summarize the results of our simulations as Table A1 in Appendix A.

3.1 Overview

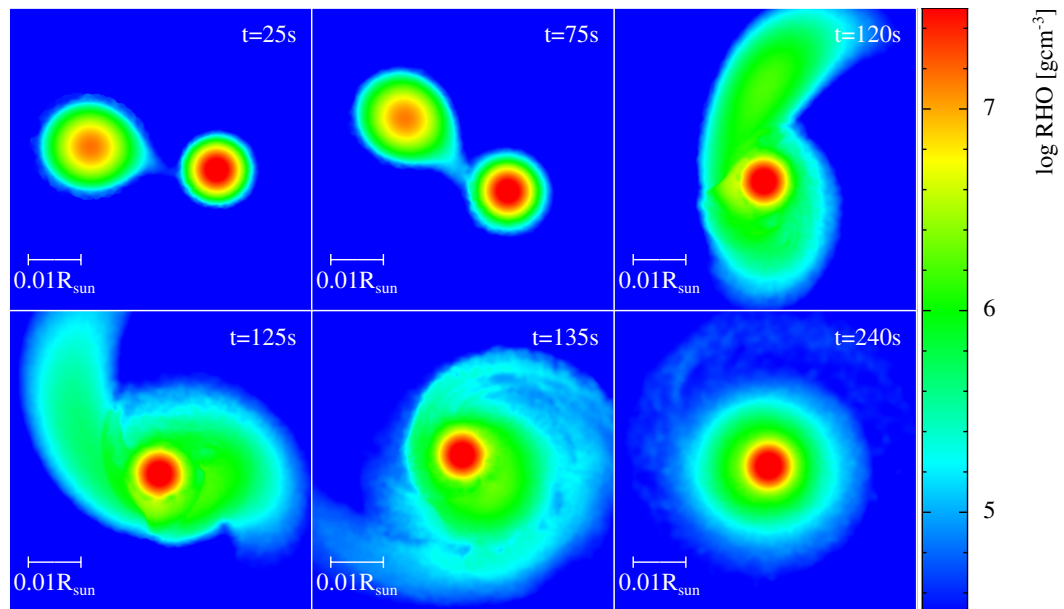


FIGURE 3.1: The dynamical evolution of our merger simulation of $1.1 + 0.9 M_\odot$ WDs. Its resolution is $500k M_\odot^{-1}$. Panels show density profiles in the equatorial plane. Color bar indicates mass density on a logarithmic scale. This figure is taken from Figure 1 of Sato et al. (2015).

Figure 3.1 shows the evolution of density profiles of our simulation of $1.1 + 0.9 M_\odot$ WDs merger in the equatorial plane, whose numerical resolution is $500k M_\odot^{-1}$. We can see that the secondary ($0.9 M_\odot$) WD is disrupted

and violently accretes onto the primary ($1.1 M_{\odot}$) one, and form a quasi-stationary merger remnant finally. We divide dynamical evolution of CO WD mergers into two phases, which are the dynamical merger phase and the (early) remnant phase (see also Section 1.3.2). In Figure 3.1, the dynamical merger phase corresponds to the first to fifth panel, and the (early) remnant phase does to the sixth panel. Their morphological structures are similar to those of merger simulations with the same mass combination performed in the previous studies (see e.g., Pakmor et al., 2012a).

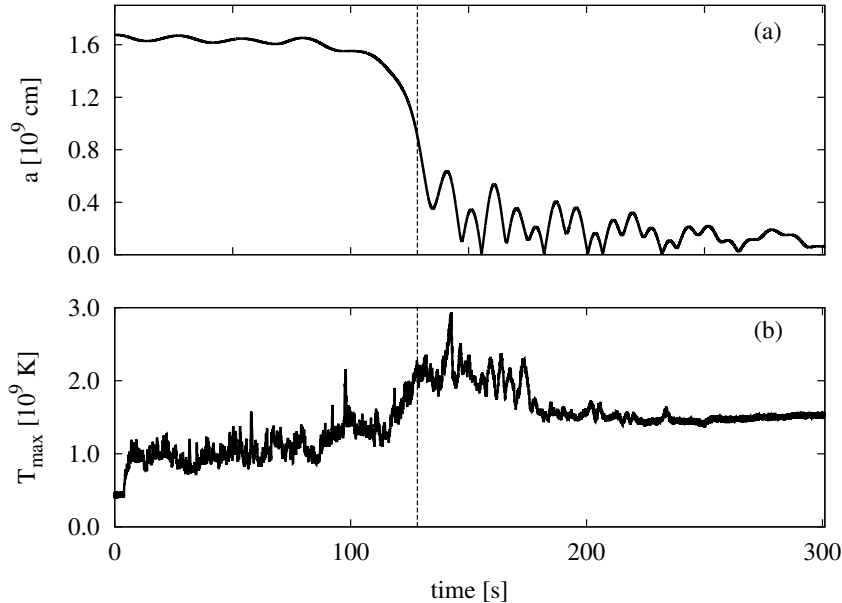


FIGURE 3.2: Time evolution of (a) the orbital separation and (b) the maximum temperature of $1.1 + 0.9 M_{\odot}$. Vertical dashed lines show the time when the first detonating particle appears. This figure is taken from Figure 1 of Sato et al. (2016).

Figure 3.2 shows the time evolution of binary orbital separation and the maximum temperature of $1.1 + 0.9 M_{\odot}$. Here, we define the binary orbital separation as separation between the centers of mass of the primary and that of the secondary. The maximum temperature increases drastically as the separation rapidly decreases. This indicates that high temperature regions are formed by violent accretion of the disrupted secondary. After 200 s, the orbital separation and the maximum temperature become almost steady, which indicates that the merger system goes to the (early) remnant phase from the dynamical merger phase. This is consistent with the evolution of density profiles shown in Figure 3.1. These behaviors are also consistent with the previous studies.

From the next section, we investigate the possibility that the merger leads to an SN Ia in each dynamical phase. First, we check whether dynamical carbon burning ignites in the dynamical merger phase for all our simulations because it is one of necessary conditions for an SN Ia explosion in the violent merger scenario. Next, we check whether steady off-center carbon burning occurs in the (early) remnant phase. If off-center carbon burning starts in the remnant phase, it would convert a CO core of the

merger remnant into an ONeMg WD and the remnant collapses to a neutron star instead of exploding as an SN Ia at last.

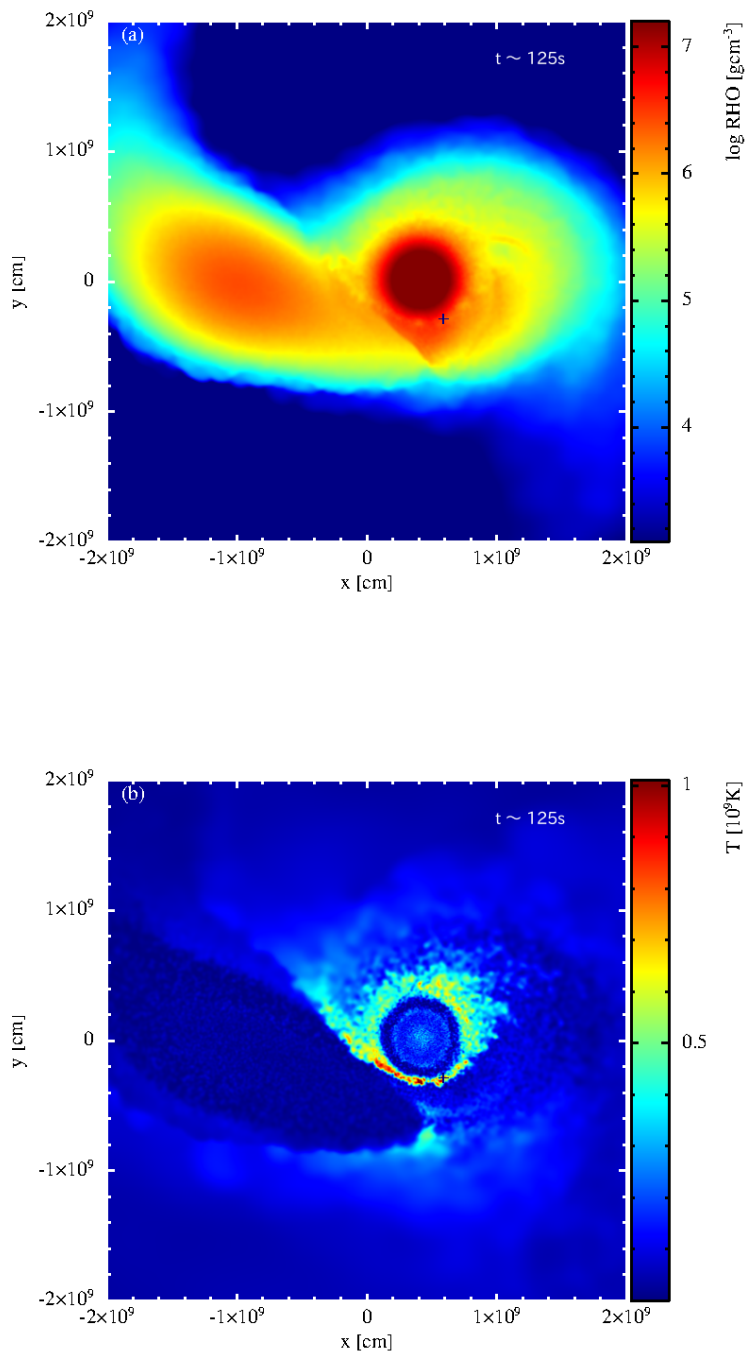


FIGURE 3.3: Profiles of (a) density and (b) temperature on the equatorial plane at the time shown by black dashed lines in Figure 3.2. Its mass combination is $1.1 + 0.9 M_{\odot}$ and numerical resolution is $500k M_{\odot}^{-1}$. Black crosses indicate the location of the first detonating particle. This figure is taken from Figure 2 of Sato et al. (2016).

3.2 Dynamical merger phase

3.2.1 Violent merger scenario

Figure 3.3 is a snap shot in the dynamical merger phase. It shows (a) density and (b) temperature profiles on the equatorial plane at the time which is indicated by dashed lines in Figure 3.2, in the same case as Figure 3.1. In the dynamical merger phase, the secondary WD starts mass transfer to the primary by the RLOF. It is disrupted by the primary, and matter of the disrupted secondary violently accrete onto the surface of the primary. Accreting matter are heated by a shock before they reach the surface. After falling on the surface, they are compressed by the following accreted matter and heated up further. As a result, they form high temperature regions.

Pakmor et al. (2010) and Pakmor et al. (2012a) suggested that carbon ignites dynamically and carbon detonation occurs in high temperature regions. They showed that the detonation waves propagate into the primary CO WD, and convert it into iron group elements. The detonation waves also convert the secondary into intermediate elements (e.g., silicon, sulfur). Consequently, the binary system explodes as an SN Ia. They called such an explosion mechanism the violent merger scenario.

Since our simulations cannot directly resolve initiation of detonation because of non-inclusion of nuclear reactions, we try to judge it from occurrence of dynamical carbon burning in the high temperature regions, which is a necessary condition for the violent merger scenario.

3.2.2 Conditions for the violent merger scenario

As mentioned above, it is crucial for the violent merger explosion whether carbon detonation occurs during the dynamical merger phase. Some previous studies (Pakmor et al., 2010; Pakmor et al., 2011; Pakmor et al., 2012a) used results of Seitenzahl et al. (2009), as their detonation condition ($\rho > 2 \times 10^6 \text{ g cm}^{-3}$ and $T > 2.5 \times 10^9 \text{ K}$), which calculated 1D detonation simulations of CO mixtures. However, treatment of detonation condition is still controversial. In our study, we judge the initiation of carbon detonation by condition whether the dynamical carbon burning occurs, that is, a carbon burning timescale becomes shorter than a dynamical timescale.

We calculate the dynamical timescale τ_{dyn} (e.g., Fowler and Hoyle, 1964; Nomoto, 1982a) from

$$\tau_{\text{dyn}} = \frac{1}{\sqrt{24\pi G\rho}}, \quad (3.1)$$

and the carbon burning timescale τ_{CC} from

$$\tau_{\text{CC}} = \frac{C_P T}{\epsilon_{\text{CC}}}, \quad (3.2)$$

for each SPH particle. Here, ρ and T are density and temperature of a SPH particle respectively, G is the gravitational constant, and C_P is the specific heat at constant pressure, which is derived from ρ and T using the

Helmholtz EOS (Timmer and Swesty, 2000), and ϵ_{CC} is the energy generation rate of carbon burning, i.e., $^{12}\text{C} + ^{12}\text{C}$ reaction. We adopt same formulation of ϵ_{CC} as Dan et al. (2014), proposed by Fowler et al. (1975) and Blinnikov and Khokhlov (1987),

$$\begin{aligned} \epsilon_{CC} &= q_C \rho A_T Y_C^2 \exp(-Q/T_{9a}^{1/3} + f_{CC}) [\text{erg g}^{-1} \text{s}^{-1}], \\ A_T &\equiv 8.54 \times 10^{26} T_{9a}^{5/6} T_9^{-3/2} [\text{s}^{-1} \text{mol}^{-1} \text{cm}^3], \end{aligned} \quad (3.3)$$

where $q_C = 4.48 \times 10^{18} \text{ erg mol}^{-1}$ (Blinnikov and Khokhlov, 1987), $T_9 = T/10^9 \text{ K}$, $T_{9a} = T_9/(1 + 0.067T_9)$, $Q = 84.165$ (Fowler et al., 1975), Y_C carbon abundance derived as $Y_C = n_C/(\rho N_a) = 0.0417 \text{ mol g}^{-1}$, where n_C and N_a are number density of carbon and the Avogadro constant, respectively, and f_{CC} is the screening factor and we ignore it in this study, because the electron screening effect is negligibly small in density range of $\rho = 10^6 - 10^7 \text{ g cm}^{-3}$ and temperature of $T = 2 \times 10^9 \text{ K}$, where carbon burning would occur. When there are any particles which satisfy $\tau_{CC} < \tau_{\text{dyn}}$, carbon burning would ignite dynamically.

If the condition $\tau_{CC} < \tau_{\text{dyn}}$ is satisfied, carbon burning increases temperature more rapidly than cooling due to hydrodynamic expansion, and the nuclear burning is accelerated. The temperature would finally increase high enough to satisfy carbon detonation condition, such as the results of Seitzzahl et al. (2009). In this study, we consider our condition of the dynamical carbon burning, $\tau_{CC} < \tau_{\text{dyn}}$, as our carbon detonation condition in cases without nuclear reactions. We confirm the validity of this consideration later by performing several merger simulations with effect of simple $^{12}\text{C} + ^{12}\text{C}$ reaction in Section 4.2.2.

Figure 3.4 shows density and temperature of SPH particles which have the smallest $\tau_{CC}/\tau_{\text{dyn}}$ ratio for each our simulations with $500k M_\odot^{-1}$. Colors and shapes of symbols indicate the total mass and the primary mass of our model, respectively. A black line depicts where $\tau_{CC} = \tau_{\text{dyn}}$. We regard that carbon detonation occurs and results in a violent merger SN Ia explosion for models whose symbols lie above that line. In Figure 3.3, black crosses depict the location of the first particle which satisfies our detonation condition in the simulation of $1.1 + 0.9 M_\odot$. Morphological structure in which the first detonating particle appears is almost consistent with the previous studies (e.g., Pakmor et al., 2012a).

As mentioned in Section 2.2.4, temperature of a particle is possibly affected by numerical fluctuations in our SPH simulations. If the temperature is enhanced by the noises, we might incorrectly judge the carbon detonation condition. In order to reduce the influence of the temperature fluctuations, we examine whether a particle continuously satisfies $\tau_{CC} < \tau_{\text{dyn}}$ for at least its dynamical timescale (e.g., $\tau_{\text{dyn}} \sim 0.4 \text{ s}$ at $\rho \sim 10^6 \text{ g cm}^{-3}$). If satisfied, we consider that the dynamical carbon burning definitely starts, and carbon detonation occurs. For examples, mergers of $0.8 + 0.8 M_\odot$ and $0.75 + 0.75 M_\odot$, whose symbols are surrounded by black lines in Figure 3.4, both satisfy $\tau_{CC} < \tau_{\text{dyn}}$. However, in the case of $0.75 + 0.75 M_\odot$, there is no particle which continuously satisfy our detonation condition during the dynamical timescale. In the case of $0.8 + 0.8 M_\odot$, on the other hand, three particles keep satisfying the detonation condition for longer than τ_{dyn} , in the dynamical merger phase. Thus, we conclude that carbon detonation

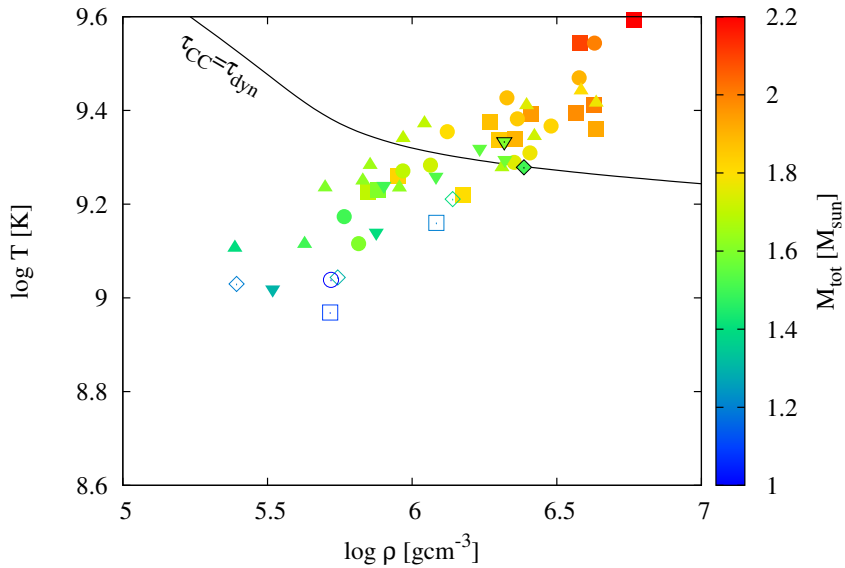


FIGURE 3.4: Density and temperature of particles with the smallest τ_{CC}/τ_{dyn} ratio for each CO WD merger model. Colors of symbols indicate total mass of the system. As it becomes redder, the total mass increases. Shapes of symbols describe the mass of the primary. The filled squares are $1.1 M_{\odot}$, the filled circles $1.0 M_{\odot}$, the filled triangles $0.9 M_{\odot}$, the filled inverted triangles $0.8 M_{\odot}$, the filled diamonds $0.75 M_{\odot}$, the open diamonds $0.7 M_{\odot}$, the open squares $0.6 M_{\odot}$, and the open circles $0.5 M_{\odot}$. The symbols surrounded by black frames indicate $0.8 + 0.8 M_{\odot}$ (filled inverted triangle) and $0.75 + 0.75 M_{\odot}$ (filled diamonds), respectively. The solid black line depicts $\tau_{CC} = \tau_{dyn}$. This figure is taken from Figure 3 of Sato et al. (2016).

does occur in $0.8 + 0.8 M_{\odot}$ model and it eventually leads to an SN Ia in the violent merger scenario.

3.2.3 The critical mass ratio for violent merger scenario

In Figure 3.4, we find a trend that density and temperature generally become higher as total mass increases. This trend can be explained by two main factors. First, as the primary becomes more massive, its gravitational well becomes deeper and compressional heating of matter on the primary surface becomes stronger. Second, in models with the same primary mass, more violent mass transfer occurs (e.g., Marsh et al., 2004) and compression by accretion stream becomes stronger as the secondary mass becomes more massive. In other words, carbon detonation occurs and the violent merger explosion would success more easily as a merger system has a more massive primary and its mass ratio approaches unity. From above discussion, it is required to obtain the "critical mass ratio", above which the violent merger scenario is realized.

Pakmor et al. (2011) first investigated the critical mass ratio (q_{cr}) performing 3D SPH simulations of mergers of CO WDs. They found that $q_{cr} = 0.8$ for $M_1 = 0.9 M_{\odot}$. Dan et al. (2012) and Dan et al. (2014)

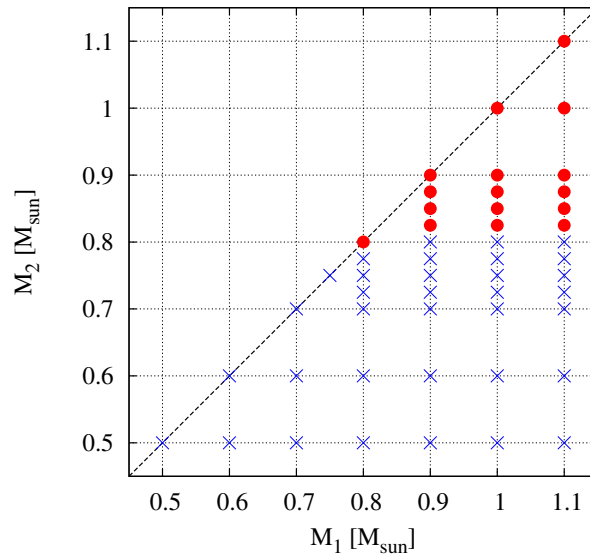


FIGURE 3.5: $M_1 - M_2$ diagram shows the results of our investigation whether each model satisfies our detonation condition. Red filled circles denote models which satisfy the condition, while blue crosses depict models which do not. The black dashed line is where the mass ratio becomes unity. This figure is taken from Figure 4 of Sato et al. (2016).

performed similar SPH simulations for a wide mass range $0.2 - 1.2 M_\odot$, and found that the dynamical carbon burning occurs only in very massive models, e.g., $1.1 + 1.1 M_\odot$. However, numerical resolutions of their simulations were very low ($\sim 2 \times 10^4$ particles). Numerical resolution is one of important factors to investigate initiation of the dynamical carbon burning in merger simulations (e.g., Pakmor et al., 2012b; Sato et al., 2015; Tanikawa et al., 2015). Sato et al. (2015) suggested that $> 5 \times 10^5 M_\odot^{-1}$ should be needed. Although Pakmor et al. (2011) performed their merger simulations with relatively high resolution ($\sim 10^6$ particles per star), they studied only $M_1 = 0.9 M_\odot$. Thus, a detailed study of the critical mass ratio is required to investigate the violent merger scenario.

Here, we show our results, whether each merger model satisfies our carbon detonation condition, $\tau_{CC} < \tau_{\text{dyn}}$, and derive the critical mass ratio for each mass of the primary, i.e., $q_{\text{cr}}(M_1)$.

Figure 3.5 shows the results of our simulations in the $M_1 - M_2$ diagram. The black dashed line depicts $M_1 = M_2$. The red filled circles indicate the models which satisfy our carbon detonation condition while the blue crosses denote the models which do not. Figure 3.5 indicates that the only models whose primary and secondary masses are more massive than $\sim 0.8 M_\odot$ satisfy our carbon detonation condition. In these models, the dynamical carbon burning occurs in the dynamical merger phase, carbon detonation initiates, and finally, they would explode as an SN Ia in the violent merger scenario. We find that none of CO WD mergers with a total mass less than Chandrasekhar limit could explode in the violent merger scenario. Here, we perform simulations of CO WD mergers with smaller

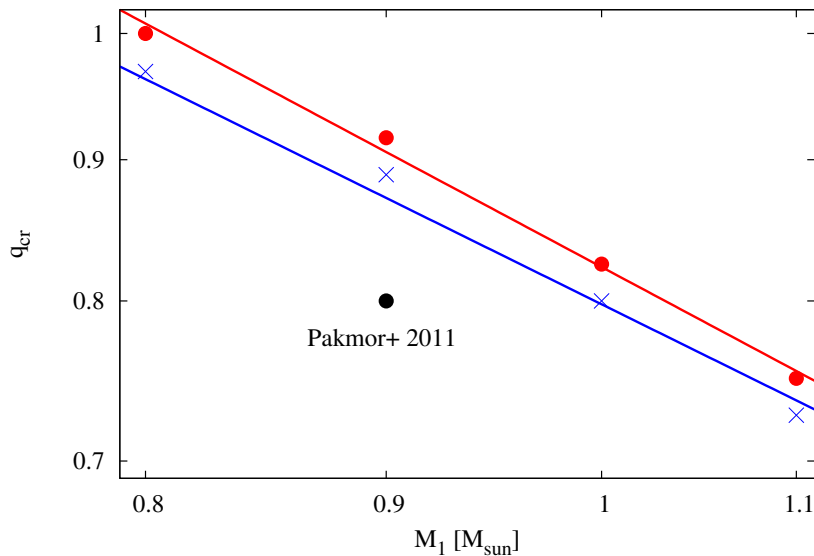


FIGURE 3.6: The critical mass ratio q_{cr} for the violent merger scenario against the primary mass. The red solid line denotes an upper bound represented by Equation 3.4, while the blue solid line is a lower bound represented by Equation 3.5. We also present the critical mass ratio as a black point for $0.9 M_{\odot}$ derived by Pakmor et al. (2011).

mass step ($= 0.025 M_{\odot}$) in range of $0.7 M_{\odot} < M_2 < 0.9 M_{\odot}$ than other mass ranges because the critical mass ratio would be expected within the range.

Using these results, we derive approximate formulae of the critical mass ratio of the violent merger scenario as a function of the primary mass, $q_{\text{cr}}(M_1)$. We plot them in Figure 3.6 together with the result of the previous study (Pakmor et al., 2011), which is $q_{\text{cr}}(0.9 M_{\odot}) = 0.8$ (a black point). The red solid line is an approximate formula for an upper bound, while the blue solid line is for a lower bound. They are represented by,

$$q_{\text{cr}}(M_1) = 0.82 \left(\frac{M_1}{M_{\odot}} \right)^{-0.91} \quad (\text{upper bound}), \quad (3.4)$$

$$q_{\text{cr}}(M_1) = 0.80 \left(\frac{M_1}{M_{\odot}} \right)^{-0.84} \quad (\text{lower bound}), \quad (3.5)$$

respectively. If we consider the lowest mass ratios in which models satisfy our carbon detonation condition, we derive Equation 3.4. On the other hand, we derive Equation 3.5 from the highest mass ratios in which models do not satisfy the condition.

We note that our critical mass ratio, which is $q_{\text{cr}} \sim 0.9$ at $M_1 = 0.9 M_{\odot}$, is larger than that of Pakmor et al. (2011), which is $q_{\text{cr}} = 0.8$ at the same mass. We will discuss what causes this difference in Section 4.2.2.

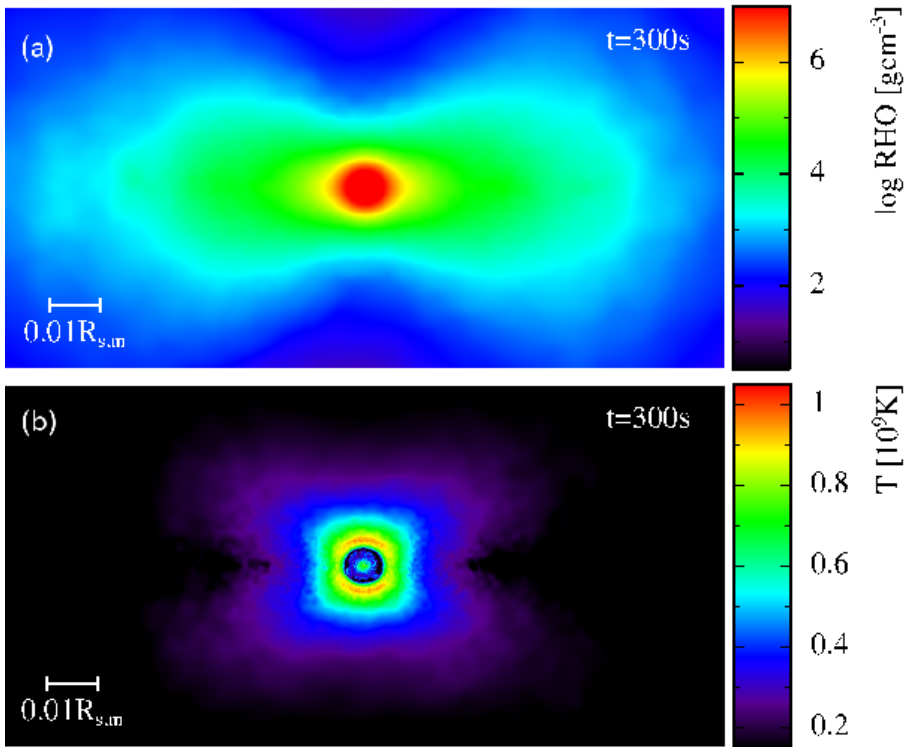


FIGURE 3.7: The structure of merger remnant of $1.1 + 0.9 M_{\odot}$ with $500k M_{\odot}^{-1}$ particles at the end of the early remnant phase. (a) The density profile on a logarithmic scale in the x - z plane, while (b) the temperature profile on a linear scale. The center of the remnant is slightly heated by numerical noises and the artificial viscosity. It has no physical meaning. This figure is taken from Figure 3 of Sato et al. (2015).

3.3 Remnant phase

If the dynamical carbon burning does not occur in the dynamical merger phase, a model fails to explode in the violent merger scenario and goes into a quasi-stationary state, the (early) remnant phase, and eventually forms a merger remnant at the end of the phase. Figure 3.7 presents (a) density and (b) temperature profiles in the x - z plane of the merger remnant in $1.1 + 0.9 M_{\odot}$ with $500k M_{\odot}^{-1}$ particles. As mentioned in Section 1.3.2, structures of merger remnants were studied by many previous works. They showed that it consists of a cold core made from the primary, hot envelope, and outer Keplerian disk. Although there are small differences among the previous works, their results are almost consistent with each other. As Figure 3.7 indicates, our results are also consistent with them. Although its central region becomes slightly hot, it is not physical effect because the heating is due to numerical noises and the artificial viscosity. Thus, we ignore that here.

Kashyap et al. (2015) performed merger simulations of $1.1 + 1.0 M_{\odot}$. They found that a spiral instability occurs in the accretion disk during the dynamical merger process. The instability drives violent mass accretion

and makes a hot spot with $\rho \sim 10^7 \text{ g cm}^{-3}$ and $T \sim 3 \times 10^9 \text{ K}$. They suggested that carbon detonation initiates at this hot spot and the merger system explodes as an SN Ia. Tanikawa et al. (2015), which used the same SPH code as this study, performed simulations of CO WDs merger of the same mass combination as Kashyap et al. (2015). Tanikawa et al. (2015) found that a second temperature peak appears after the first peak is produced by the violent merger. They showed the appearance of a spiral and hot spot which are similar to those of Kashyap et al. (2015) although they did not have any conclusion. Our simulation of $1.1 + 0.9 M_{\odot}$ with $500k M_{\odot}^{-1}$ particles has a similar second peak of temperature in Figure 3.2, around $t \sim 160 \text{ s}$. However, since we did not examine the spiral instability and hot spot in this study, we do not discuss them anymore.

The hot envelope gradually accretes onto the cold core because of angular momentum loss due to some mechanisms, e.g., viscosity or magnetic fields. Temperature at the base of the hot envelope increases with accretion, and off-center carbon burning would start quiescently (e.g., Nomoto and Iben, 1985). The burning front propagates into the cold core, and it is finally converted into an ONeMg core (e.g., Saio and Nomoto, 1985; Saio and Nomoto, 1998; Saio and Nomoto, 2004). If the core grows its mass by accretion and approaches M_{Ch} , its central density increases and electron capture on neon and magnesium decreases its central pressure. At last, the core would collapse to a neutron star instead of an SN Ia explosion (e.g., Nomoto and Kondo, 1991). Such a scenario has been called the accretion induced collapse (AIC)¹.

On the other hand, if off-center carbon burning does not occur, the cold core remains a CO WD. In such cases, if matter surrounding the core fall onto the core and its mass approaches M_{Ch} , it would explode as an SN Ia. We call this explosion scenario the accretion induced explosion (AIE) here. It is critically important for the final fate of a merger remnant to examine whether off-center carbon burning occurs in the remnant phase.

We examine whether or not off-center carbon burning occurs, at the time when our merger model almost form a quasi-stationary merger remnant, i.e., the end of the (early) remnant phase. We assume that carbon quiescently ignites if carbon burning timescale τ_{CC} becomes shorter than that of neutrino cooling τ_{ν} in the hot envelope of merger remnants. Thus, our condition of occurrence of off-center carbon burning is the existence of particles which satisfy $\tau_{\text{CC}} < \tau_{\nu}$, where τ_{CC} is the same as Equation 3.2 and τ_{ν} is derived from Itoh et al. (1996) using density and temperature of each SPH particle. For example, Figure 3.8 shows a $\rho - T$ profile of the merger remnant in the same as Figure 3.7. The hot envelope corresponds to the peak of temperature. We find that particles lying above the dashed line of $\tau_{\text{CC}} = \tau_{\nu}$ satisfy our off-center burning condition. Thus, we consider that our model of $1.1 + 0.9 M_{\odot}$ with $500k M_{\odot}^{-1}$ ignites carbon burning in the hot envelope and it would lead to the AIC at last, although it would already explode as an SN Ia in the violent merger scenario during the dynamical merger phase (Section 3.2). Figure 3.9 (a) describes densities and temperatures of SPH

¹Recently, Jones et al. (2016) performed 3D hydrodynamical simulations of oxygen deflagration in ONeMg WDs. They found that the oxygen deflagration blows off almost $1 M_{\odot}$ if ignition occurs at relatively low central density proposed by Schwab et al. (2015). Although a sub-Chandrasekhar bound remnant remains after the explosion, it does not collapse to a neutron star.

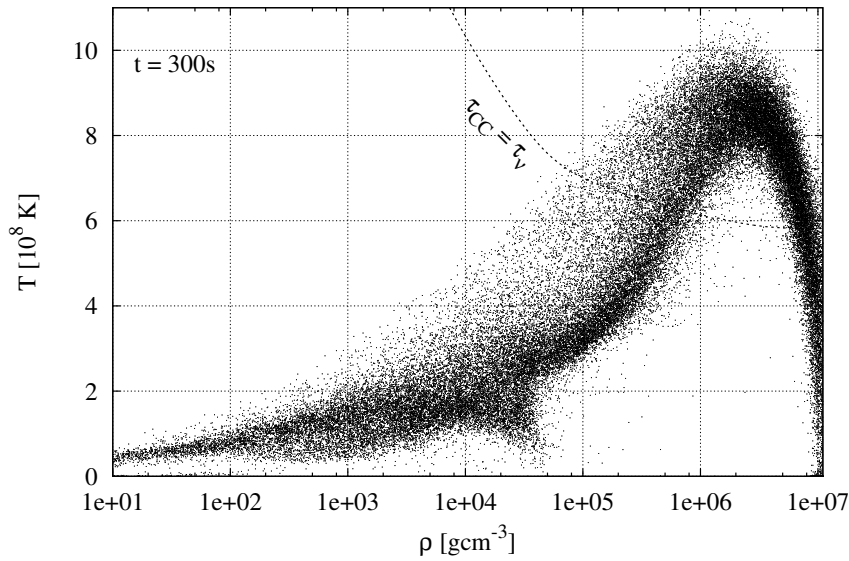


FIGURE 3.8: $\rho - T$ profile of $1.1 + 0.9 M_{\odot}$ with $500k M_{\odot}^{-1}$ at $t = 300$ s, the same as Figure 3.7. A dashed line indicates $\tau_{CC} = \tau_{\nu}$. Particles lying above the line satisfy $\tau_{CC} < \tau_{\nu}$.

particles having the highest temperature in the hot envelope at the end of the remnant phase. The black line depicts $\tau_{CC} = \tau_{\nu}$, the same as Figure 3.8. Models whose symbols lie above the line satisfy our condition of off-center carbon burning.

We judge the occurrence of off-center carbon burning from the density and temperature of the particle in Figure 3.9 (a). However, as mentioned in Section 2.2.4 and Section 3.2.2, it would be affected by the numerical noises. When we judged the dynamical carbon burning during the dynamical merger phase in Section 3.2.2, we use the duration time in which a particle continues satisfying our detonation condition to remove effect of the numerical noises. However, in the present cases, a timescale of neutrino cooling with a typical density and temperature of a hot envelope is too long to follow in our SPH simulations. For example, when $\rho = 10^6 \text{ g cm}^{-3}$ and $T = 6 \times 10^8 \text{ K}$, $\tau_{\nu} > 8 \times 10^3 \text{ yr}$ using Itoh et al. (1996). Figure 3.7 (b) indicates that the hot envelope, where off-center carbon burning would occur, has a large spatial size, while the hot region where carbon detonation would occur has much smaller scale (see Figure 3.3 (b)). Thus, we use the smoothed temperature T_s , which was introduced in Dan et al. (2014). It is derived as

$$T_{s,i} = \sum_j \frac{m_j}{\rho_j} T_j W(\mathbf{r}_{ij}, h_{ij}), \quad (3.6)$$

where the definitions of variants are the same as in Chapter 2. Usage of T_s could prevent from choosing a particle whose temperature is enhanced by the noises because spatial smoothing can reduce the numerical effect. Figure 3.9 (b) shows the results using T_s . We find that the symbols generally move to lower temperature and some models, which are judged satisfying our condition of off-center carbon burning in Figure 3.9 (a), do not satisfy that in Figure 3.9 (b).

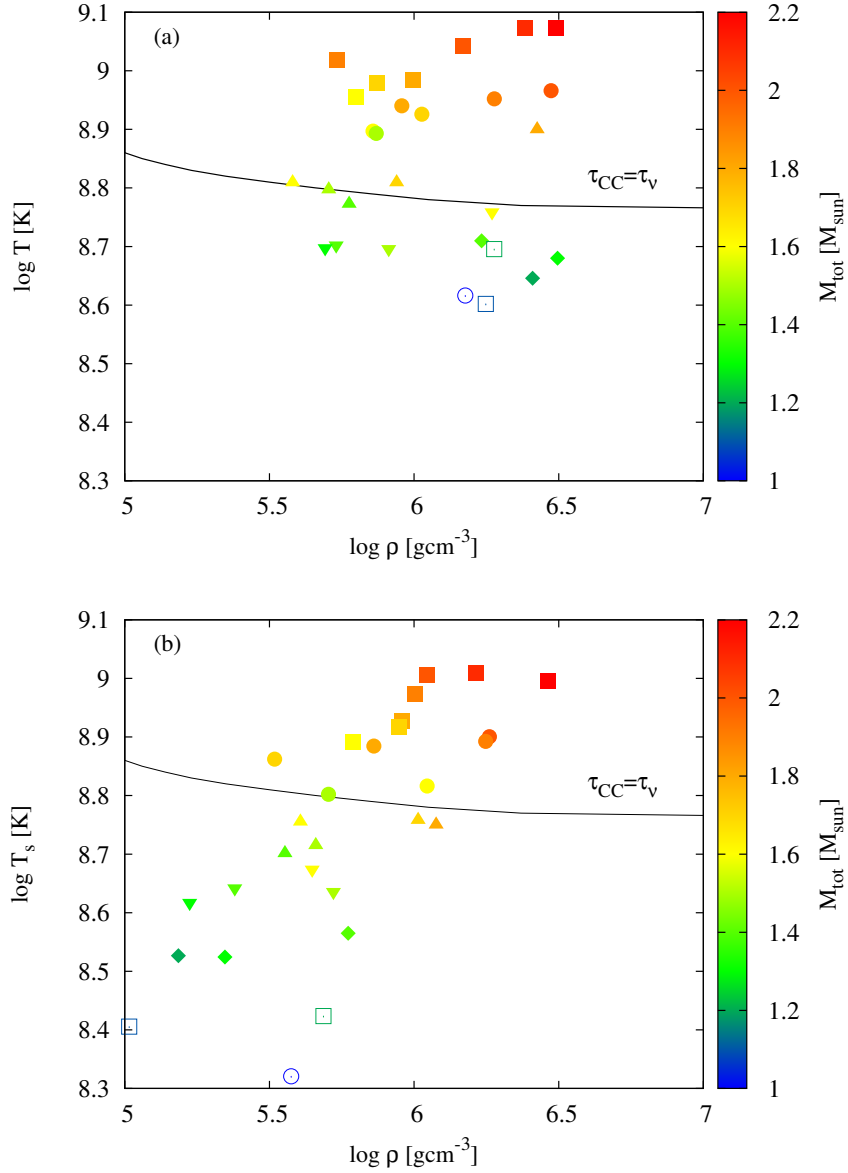


FIGURE 3.9: Density and temperature of a particle with the highest temperature at the time when the merger remnant reach almost a quasi-stationary state. Colors and shapes of the symbols have the same meanings as Figure 3.4, but filled diamonds indicate models with $M_1 = 0.7 M_{\odot}$. (a) The result for the raw temperature. (b) For the smoothed temperature T_s . See text for details. Both axes are on the logarithmic scale. This figure is taken from Figure 4 of Sato et al. (2015).

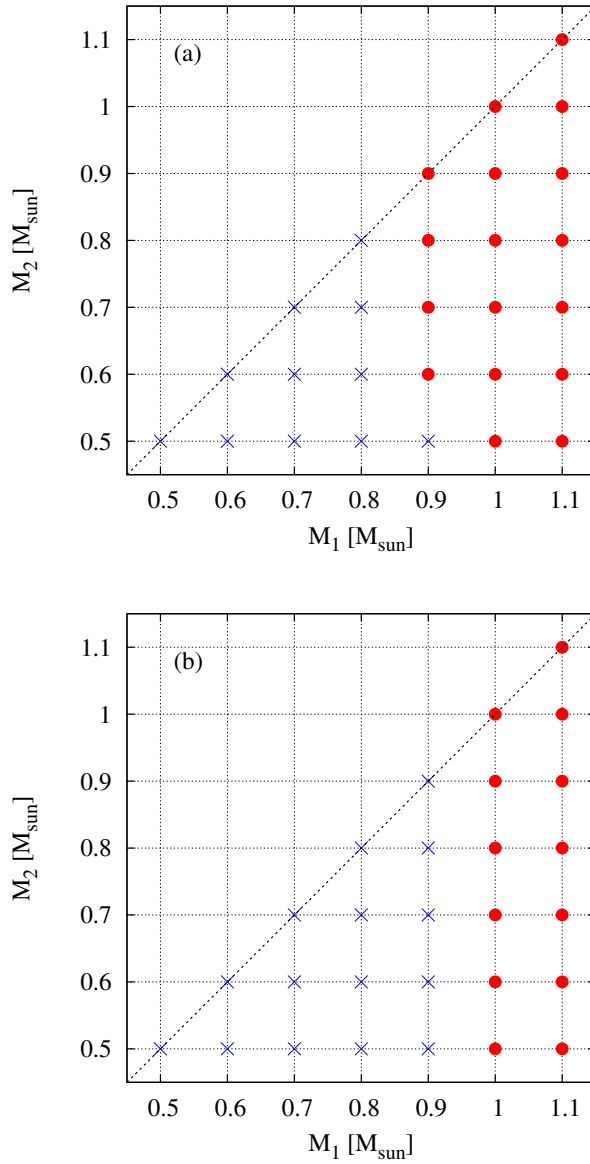


FIGURE 3.10: $M_1 - M_2$ diagram shows the results of our investigation whether each model satisfies our off-center carbon burning condition. The red filled circles denote models which satisfy the condition, while the blue crosses depict models which do not. The black dashed line is where the mass ratio becomes unity. (a) The results using raw temperature T , while (b) those for smoothed temperature T_s .

We summarize our results whether or not off-center carbon burning occurs in Figure 3.10, which is similar to Figure 3.5. We do not investigate models whose secondary mass is within $0.7 M_{\odot} < M_2 < 0.9 M_{\odot}$ here. Our models with $M_1 \geq 0.9 M_{\odot}$ are judged to ignite off-center carbon burning near the boundary between the cold core and hot envelope when we adopt raw temperature (Figure 3.10 (a)). On the other hand, when we use the smoothed temperature T_s , we find that models with $M_1 \geq 1 M_{\odot}$ satisfy $\tau_{CC} < \tau_{\nu}$ (Figure 3.10 (b)).

If total mass ($M_1 + M_2$) of a merger remnant exceeds M_{Ch} and it satisfies our condition of off-center carbon burning, the remnant is considered to collapse to a neutron star in the AIC scenario, not explode as an SN Ia². When $M_1 + M_2 \geq M_{Ch}$ and the merger remnants do not satisfy the condition, we regard that their cores approach M_{Ch} by accumulating surrounding matter and would lead to an SN Ia in the AIE scenario, at last. If $M_1 + M_2 < M_{Ch}$, the merger would form a single massive CO WD eventually.

In order to obtain a definitive conclusion, we have to follow the viscous and thermal evolution phases (see also Section 1.3.2). However, we stop our SPH simulations at the end of the early remnant phase when a merger system form a quasi-stationary remnant because we do not introduce any physical viscosities, e.g., that generated by magnetic rotational instability (MRI). The hot envelope and outer disk further accrete onto the cold core, and compress matter on the surface of the core. The density and temperature of accreted matter gradually increase further. As a result, off-center carbon burning might ignite even in the cases in which it does not occur in the early remnant phase. In fact, Schwab et al. (2012) calculated the viscous evolution of several merger remnants in 2D hydrodynamical simulations, and showed that off-center carbon burning could starts in some models (e.g., $0.9 + 0.6 M_{\odot}$, see their Figure 3). Similarly, Shen et al. (2012) followed the viscous and thermal evolution phases for several models in 1D simulations. They found that some of them, e.g., $0.8 + 0.6 M_{\odot}$, would ignite carbon burning in the hot envelope in the thermal evolution phase³ (see their Figure 6). Yoon et al. (2007) performed SPH simulations of CO WD merger whose mass combination is $0.9 + 0.6 M_{\odot}$ and further followed the viscous and thermal evolution of the merger remnant with a 1D stellar evolution code. They showed that off-center carbon burning can be avoided when the temperature of the hot envelope is lower than the threshold of carbon ignition, the timescale of angular momentum loss is longer than τ_{ν} , and the mass accretion rate satisfies $\dot{M} \leq 5 \times 10^{-6}$ to $10^{-5} M_{\odot} \text{ yr}^{-1}$. In this study, our condition of off-center carbon burning is posed only for the early remnant phase but not applied yet to the viscous and thermal evolution phase. In this sense, our results do not show the definitive answers yet.

Recently, several studies of stellar evolution suggested that propagation of carbon burning front might be quenched due to mixing at convective boundary before it reaches the center of a CO core (e.g., Denissenkov et al.,

²If the total mass is lower than M_{Ch} , we consider that it would form an ONeMg WD finally. In our simulations, however, such models do not appear.

³In our simulations, a remnant of $0.9 + 0.6 M_{\odot}$ does not satisfy our off-center carbon burning condition using the smoothed temperature, and $0.8 + 0.6 M_{\odot}$ does not in both cases of raw and smoothed temperature.

2013; Chen et al., 2014). As a result, the core is converted into a hybrid CONe WD, which consists of an unburned CO core and ONe mantle surrounding it. In such cases, when mass of the core approaches M_{Ch} , central carbon ignition occurs and it might lead to an SN Ia-like explosion instead of AIC. Kromer et al. (2015) performed 3D hydrodynamical simulations of explosions of such hybrid WDs, and found that such explosions would be observed as faint SNe Ia. However, Lecoanet et al. (2016), which performed 3D hydrodynamical simulations of convective mixing at carbon burning flame, found that convective plumes are not dense enough to intrude into the flame. They concluded that hybrid CONe WDs would be not common products in standard stellar evolution. Moreover, Brooks et al. (2017) suggested that mixing between core and mantle occurs during cooling of a hybrid WD and its central carbon abundance would decrease consequently. It is still unclear whether a hybrid WD experiencing the mixing can explode as an SN Ia. Although the present situation of studies on the AIE/AIC is still unclear, we adopt the classical AIC scenario in this study. Thus, we assume that if off-center carbon burning ignites in a hot envelope of a merger remnant, a CO core is converted into an ONeMg WD, and collapses into a neutron star when its total mass is above M_{Ch} .

3.4 Merger outcomes

Using the results described in Section 3.2 and Section 3.3, we derive a relation between masses of merging CO WDs and the outcome produced from their merger, and identify the mass range leading to an SN Ia explosion. Here, we assume four scenarios of merger outcomes. (1) If there are any SPH particles satisfying our condition of carbon detonation $\tau_{\text{CC}} < \tau_{\text{dyn}}$ during violent accretion of the secondary, we consider that the merger model explodes as an SN Ia in the violent merger scenario. (2) Among models which do not satisfy our carbon detonation condition, the models which have the total mass $\geq M_{\text{Ch}}$ would explode as an SN Ia in the AIE scenario if any particles do not satisfy our condition of off-center carbon burning at the end of the remnant phase. (3) On the other hand, we regard models, which have the total mass $\geq M_{\text{Ch}}$ and satisfy our off-center carbon burning condition, would collapse to a neutron star along the AIC scenario at last. (4) Mergers whose total mass does not exceed M_{Ch} , which do not satisfy both our conditions of carbon detonation and off-center carbon burning, form single massive CO WDs. In our study, we consider the violent merger and AIE paths are possible paths to SNe Ia among these four scenario.

Figure 3.11 is $M_1 - q$ diagram that show merger outcomes for each mass combination of CO WD binaries. Color hatched regions indicate mass ranges for each merger outcome. The red hatched region corresponds to the mass range of the violent merger (VM) scenario. The green hatched region is that of the AIE scenario, while the blue one depicts the AIC. The magenta hatched region is the mass range where the final fate of CO WD merger is a formation of a massive WD (MWD). As mentioned above, more studies on the evolution of a merger remnant after our remnant phase is necessary to identify whether the final fate of the remnant is the AIE or AIC. Thus, we label the AIE region as the AIE/AIC here. The black dotted line denotes where $M_1 + M_2 = M_{\text{Ch}}$. We use Equation 3.5 as a lower boundary of the

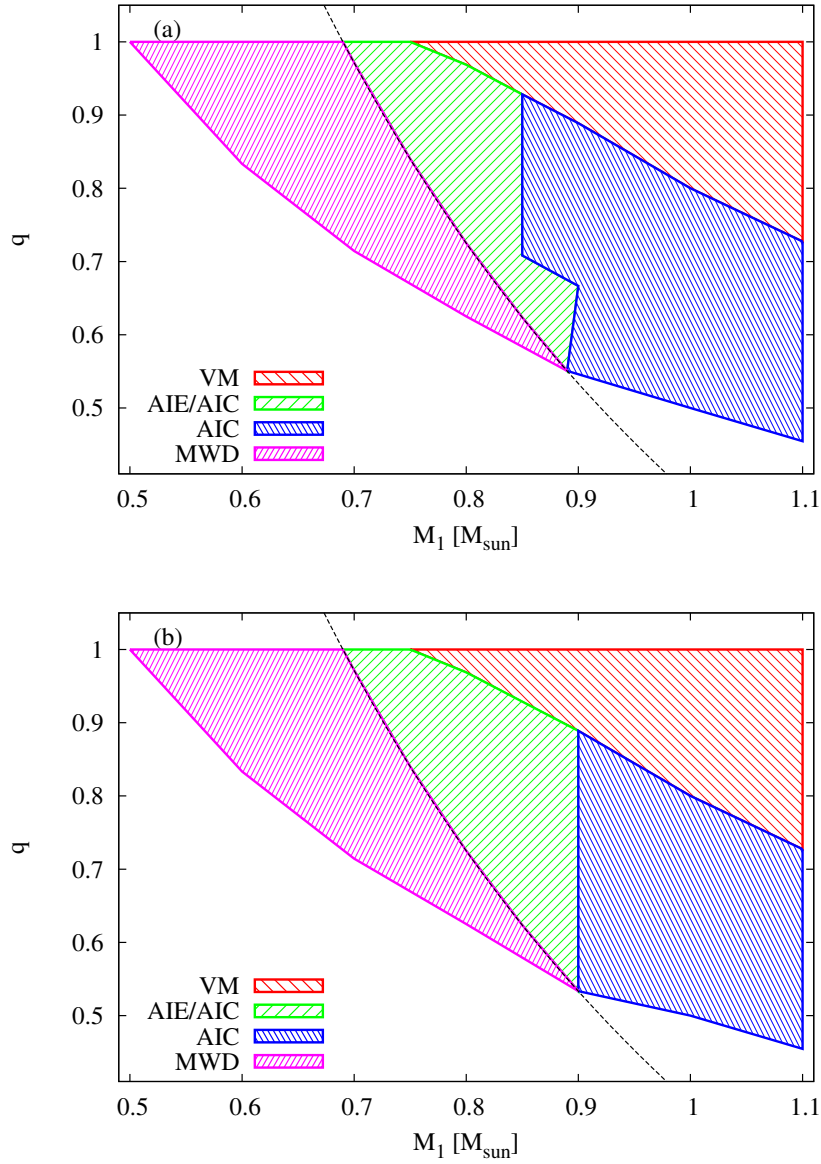


FIGURE 3.11: This $M_1 - q$ diagram indicates mass ranges of each merger outcome derived from our results. The red hatched region is the violent merger (VM), green the AIE (or lead to AIC due to post-merger evolution after the end of our simulations), blue the AIC, and magenta the formation of a single massive CO WD (MWD). The black dotted line corresponds to $M_1 + M_2 = M_{\text{Ch}}$ and the lower boundary of the VM region is Equation 3.5. (a) We use the raw temperature to judge occurrence of off-center carbon burning, while (b) we adopt the smoothed temperature.

VM region. Panel (a) indicates results where we use the raw temperature to identify the off-center carbon burning. In panel (b), we adopt the smoothed temperature T_s derived from Equation 3.6. In the next Chapter, we discuss these results.

Our results suggested that massive mergers, whose masses are nearly or over $2 M_\odot$, would lead to the violent merger or the AIC. This implies that super-Chandrasekhar SNe Ia with large ejecta mass $> 2 M_\odot$ (e.g., Howell et al., 2006; Hicken et al., 2007; Scalzo et al., 2010; Yamanaka et al., 2009), whose possible progenitors are considered as DD systems, might not be explained by CO WD mergers⁴, because the amount of radioactive nickels produced from the violent merger is similar to normal SNe Ia, less than $1 M_\odot$ (e.g., Sim et al., 2010; Pakmor et al., 2012a). However, Moll et al. (2014) performed radiative hydrodynamical simulations of the violent merger SNe Ia of very massive models, calculated their light curves, and found that they could reproduce the peak luminosity of super-Chandrasekhar SNe Ia ($\sim 3 \times 10^{43}$ erg s⁻¹) due to viewing angle effect from their asymmetric configurations.

3.4.1 Ratio of WD mergers leading to SNe Ia

Before we go to discussion, we briefly estimate the ratio of CO WD mergers leading to SNe Ia, under some assumptions. First, we consider that all CO WD binaries, whose $M_1 \geq 0.8 M_\odot$ and mass ratio exceeds q_{cr} described as Equation 3.5, can explode within the violent merger scenario. We assume that systems satisfying our conditions for the AIE scenario also lead to SNe Ia. The conditions are $M_1 \leq 0.9 M_\odot$, $M_1 + M_2 \geq M_{Ch}$, the mass ratio $q < 2/3$ for $M_1 = 0.9 M_\odot$, and $q \leq q_{cr}$ for $M_1 < 0.9 M_\odot$, when we adopt the raw temperature (Figure 3.11 (a)). On the other hand, using the smoothed temperature (Figure 3.11 (b)), the conditions are $M_1 \leq 0.9 M_\odot$, $M_1 + M_2 \geq M_{Ch}$, and $q \leq q_{cr}$. Mass distribution of WDs in binary systems is still uncertain because there are only small samples, even in our neighborhood. We assume that both the primary and the secondary in Galactic WD binaries follow the mass distribution of single DA WDs in our Galaxy derived from SDSS-DR7 (Kleinman et al., 2013). Then, we can estimate the ratios of CO WD mergers exploding within the violent merger scenario and the AIE scenario to the all WD mergers. The ratio of CO WD mergers leading to SNe Ia in the violent merger is about 1% of all WD mergers, and that of CO WD mergers leading to SNe Ia in the AIE scenario is about 3.9% using the results of raw temperature (6.4% using those of smoothed temperature). If all SNe Ia originating from WD mergers explode in the violent merger or the AIE, 4.9%(7.4%) of all CO WD mergers lead to SNe Ia⁵.

⁴Super-Chandrasekhar SNe Ia could be also explained by the spin-up/down scenario in the SD model (e.g., Hachisu et al., 2012a; Hachisu et al., 2012b).

⁵Strictly speaking, for the violent merger scenario, the dynamical carbon burning is only a necessary but not sufficient condition of carbon detonation, so it is nontrivial whether models within the VM region can lead to an SN Ia. And, we have to follow further evolution of our merger remnant models for much longer time (e.g., Yoon et al., 2007; Shen et al., 2012) in order to identify whether they explode as an SN Ia or collapse to a neutron star. Thus, our estimate might be too optimistic.

Badenes and Maoz (2012) estimated that Galactic merger rate of WD binaries as $1.4 \times 10^{-13} \text{ yr}^{-1} M_{\odot}^{-1}$. When we adopt their results, the merger rate of CO WD binaries leading to an SN Ia in the violent merger is estimated about $1.4 \times 10^{-15} \text{ yr}^{-1} M_{\odot}^{-1}$. Merger rate for the AIE with the raw temperature is about $5.4 \times 10^{-15} \text{ yr}^{-1} M_{\odot}^{-1}$, while that with smoothed temperature is about $8.9 \times 10^{-15} \text{ yr}^{-1} M_{\odot}^{-1}$. The total merger rate of CO WD binaries leading to SNe Ia is up to $\sim 10^{-14} \text{ yr}^{-1} M_{\odot}^{-1}$ in our Galaxy.

We compare our rate of CO WD mergers leading to SNe Ia with an observational SNe Ia rate in our Galaxy. SN Ia rate is assumed to depend on the Hubble types and stellar mass of host galaxies. According to Li et al. (2011c), in SBc-type galaxies with similar stellar mass to that of our Galaxy $\sim 6.4 \times 10^{10} M_{\odot}$ (McMillan, 2011), the specific SN Ia rate is about $1.1 \times 10^{-13} \text{ yr}^{-1} M_{\odot}^{-1}$. Our estimate suggests that contribution from SNe Ia arising from CO WD mergers is less than one-tenth of the entire Galactic SNe Ia. Therefore, DD systems might not be major progenitors of SNe Ia in our Galaxy⁶ Of course, because this estimate has large uncertainties, the definitive conclusion has not been obtained yet (see below).

Performing binary population synthesis (BPS), Yungelson and Kuronov (2017) studied the delay time distribution (DTD) of SNe Ia originating from DD mergers. In order to estimate the maximum contribution to entire Galactic SN Ia rate, they took three extreme assumptions. (1) All mergers of CO WDs whose total mass exceeds M_{Ch} can explode as SNe Ia. (2) When CO WDs whose masses are larger than $0.47 M_{\odot}$ merge with He or CO WDs exceeding $0.37 M_{\odot}$, SN Ia explosions occur in the double detonation mechanism⁷ (Dan et al., 2012). (3) Mergers of CO WDs whose masses are larger than $0.9 M_{\odot}$ and ONeMg WDs can explode as SNe Ia. They combined their DTD and a theoretical star formation history modeling that of our Galaxy, and derived Galactic merger rate of DD systems exploding as SNe Ia as $6.5 \times 10^{-3} \text{ yr}^{-1}$, which can be comparable to the observational value. When they assumed only the violent merger as a possible path to SNe Ia and adopted our Equation 3.5 as the critical mass ratio, they found that contribution from DD mergers to SNe Ia becomes about one-twentieth of the maximum one. This is almost consistent with our estimate.

Maoz and Hallakoun (2016) used data derived from the ESO-VLT Supernova-Ia Progenitor survey (SPY, Napiwotzki et al., 2001), and reestimated Galactic WD merger rate $\sim 7.3 \times 10^{-13} \text{ yr}^{-1} M_{\odot}^{-1}$, which is several times larger than that of Badenes and Maoz (2012). If we adopt this value, our estimate of merger rate leading to the violent merger and the AIE goes up to $\sim 7 \times 10^{-14} \text{ yr}^{-1} M_{\odot}^{-1}$, whose contribution exceeds 60% of the entire Galactic SN Ia rate. If further surveys and studies for double degenerate systems will be done, these estimates could change further.

⁶According to Badenes and Maoz (2012), merging WDs whose total masses exceed M_{Ch} can account for only 10% of all WD mergers. Because the total merger rate is comparable to the Galactic SN Ia rate, mergers of super-Chandrasekhar DD systems cannot explain the entire SNe Ia.

⁷In their study, they considered that CO WDs whose masses are within $0.32 \sim 0.6 M_{\odot}$ have He envelope with $0.2 \sim 0.01 M_{\odot}$.

Chapter 4

Discussion

We discuss results of our simulations of CO WD mergers in this Chapter. First of all, we investigate dependence of our results on the numerical resolution of our simulations, and discuss their numerical trends. Second, we present comparison with the previous studies performing similar merger simulations to ours. In the next section, we predict a merger outcome of the central DD system of Henize 2-428, which is a bipolar planetary nebula, using our $M_1 - q$ diagram (Figure 3.11).

4.1 Dependence on the numerical resolution

The numerical resolution of our SPH simulations corresponds to the number of particles. As the number of particles increases, we can resolve structures in a smaller size. Pakmor et al. (2012b) suggested that the numerical resolution of SPH simulations is one of the most important factors to identify the initiation of carbon detonation in the dynamical merger phase because high temperature regions where the detonation occurs have a small spatial size in general. On the other hand, several studies showed that structure of a merger remnant at the end of the early remnant phase is not so dependent on the numerical resolution. For examples, Raskin et al. (2012) performed merger simulations of $0.81 + 0.81 M_\odot$ with $10^5 \sim 2 \times 10^6$ particles per star, and concluded that their results of the merger remnants, e.g., the masses of cold cores, angular velocities of disks, and half-mass radii of disk, almost converged at $\geq 5 \times 10^5$ particles per star. Zhu et al. (2013) investigated the numerical dependence of remnant structures of $0.65 + 0.625 M_\odot$ with about $5 \times 10^4 \sim 5 \times 10^5 M_\odot^{-1}$. They obtained similar results for each resolution although that of their lowest resolution had relatively large deviations. Dan et al. (2014)¹ also found that there are only less than 20% differences for several parameters of merger remnants, between resolutions $4 \times 10^4 M_\odot^{-1}$ and $2 \times 10^5 M_\odot^{-1}$. In particular, because the hot envelope where off-center carbon burning occurs has larger spatial size than the hot region formed in the dynamical merger phase, the identification of off-center carbon burning, or AIE/AIC, would be relatively independent of the numerical resolution than the case of carbon detonation.

In order to examine the dependence of our results on the numerical resolution, we perform merger simulations with the same mass combinations, but four different numbers of particles, i.e., $10k$, $50k$, $100k$, $500k$ per 1 solar mass. Since we are interested in the identifications of carbon detonation and off-center carbon burning in each merger phase, we focus on the numerical

¹The results with $2 \times 10^5 M_\odot^{-1}$ were obtained from Dan et al. (2011).

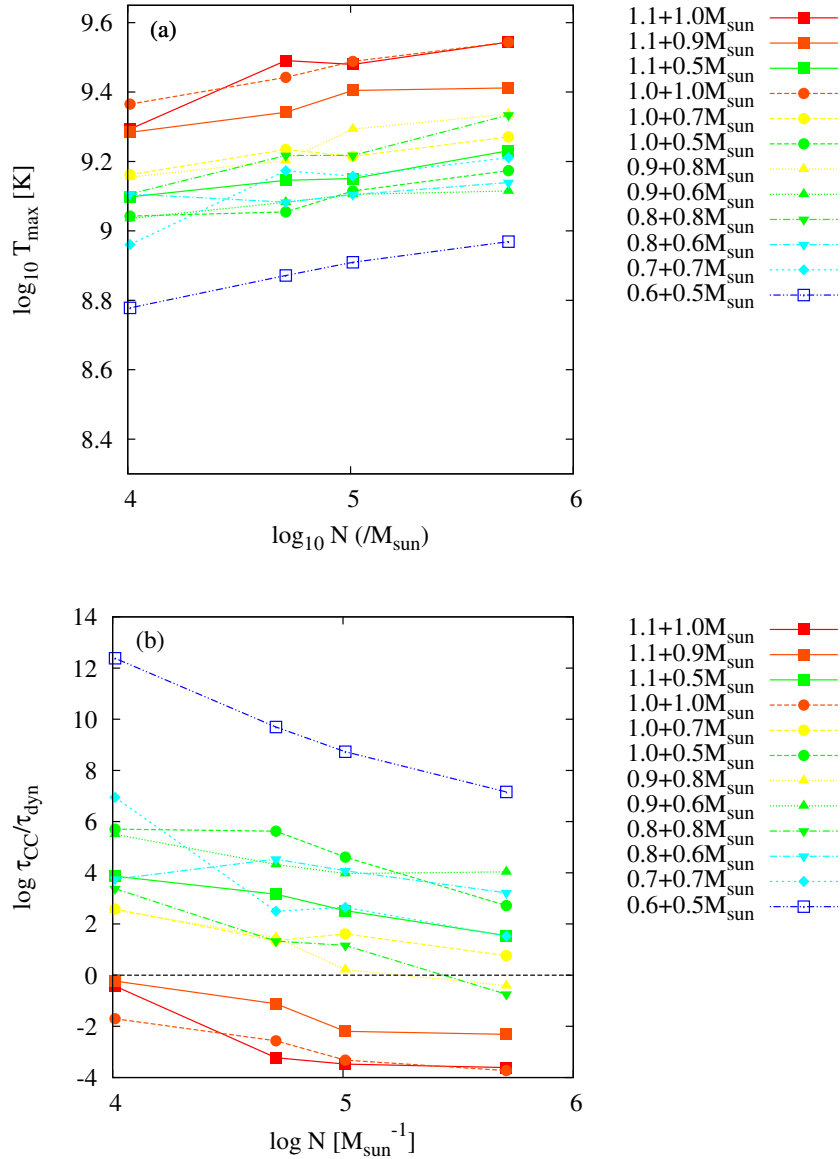


FIGURE 4.1: Dependence of (a) the highest temperature, (b) the smallest ratio of $\tau_{\text{CC}}/\tau_{\text{dyn}}$ in the dynamical merger phase. We present results of several our models. The horizontal axis is the number of SPH particles per 1 solar mass on the logarithmic scale. The shapes and colors of symbols are the same as in Figure 3.4. The horizontal black dashed line in panel (b) indicates $\tau_{\text{CC}}/\tau_{\text{dyn}} = 1.0$. The highest temperature (the smallest $\tau_{\text{CC}}/\tau_{\text{dyn}}$) tends to increase (decrease) with numerical resolution. These figures are taken from Figure 8 and 9 of Sato et al. (2015).

convergence of the maximum temperature (and the minimum timescale ratio $\tau_{\text{CC}}/\tau_{\text{dyn}}$) in the dynamical merger phase and at the end of the remnant phase. We could confirm that morphological structures of CO WD mergers are not so sensitive to the numerical resolution.

Figure 4.1 shows the numerical dependence of (a) the maximum temperature and (b) the minimum ratio of $\tau_{\text{CC}}/\tau_{\text{dyn}}$ in the dynamical merger phase on the numerical resolution. (a) The maximum temperature generally increases with the number of SPH particles. In other words, the results of our simulations do not converge yet and merger products of some models could be changed from the AIC (or AIE) to the violent merger since the dynamical carbon burning could easily occur at higher temperature. Similar tendency was also reported in Pakmor et al. (2012b) and Tanikawa et al. (2015)². In this sense, we must further increase the numerical resolution to at least more than $500k M_{\odot}^{-1}$ to definitely identify the initiation of carbon detonation, i.e., the violent merger scenario. (b) The minimum ratio of $\tau_{\text{CC}}/\tau_{\text{dyn}}$ decreases with the numerical resolution. This trend is consistent with that of the maximum temperature. A black dashed line in Figure 4.1(b) denotes where τ_{CC} becomes equal to τ_{dyn} . The models lying below the line satisfy our detonation condition, and they would explode as SNe Ia in the violent merger scenario. In particular, the two merger models in Figure 4.1(b), $0.9 + 0.8 M_{\odot}$ and $0.8 + 0.8 M_{\odot}$, satisfy in the numerical resolution $500k M_{\odot}^{-1}$, while they do not in the lower resolutions.

Figure 4.2 shows the maximum temperature for the (a) raw and (b) smoothed temperatures of merger remnants, respectively. Compared with the results in the dynamical merger phase, Figure 4.1(a), those barely depend on the numerical resolution. Especially for the case of the smoothed temperature in Figure 4.2(b), they seem to converge for almost all models in the figure. This weak dependence of the maximum temperature in the merger remnants is consistent with tendencies reported in previous studies (Raskin et al., 2012; Zhu et al., 2013; Dan et al., 2014). Thus, we conclude that the identification whether off-center quiescent carbon burning ignites (and merger systems lead to the AIE or AIC) almost converges against the number of SPH particles.

4.2 Comparison with the previous studies

Here, we compare our results with those of the previous studies. At first, we compare two individual models of our merger simulations, $1.1 + 0.9 M_{\odot}$ and $0.9 + 0.6 M_{\odot}$, with the previous studies because these mass combinations were well examined in the previous studies. We also discuss the difference of the critical mass ratio q_{cr} between our results and that of Pakmor et al. (2011), and compare the peak magnitude distribution derived from our q_{cr} with Ruiter et al. (2013), which used q_{cr} of Pakmor et al. (2011). Finally, we mention the previous studies performing similar parameter surveys to ours (Dan et al., 2012; Dan et al., 2014; Zhu et al., 2013).

²Sato et al. (2015) and Sato et al. (2016) also presented similar results to ours.

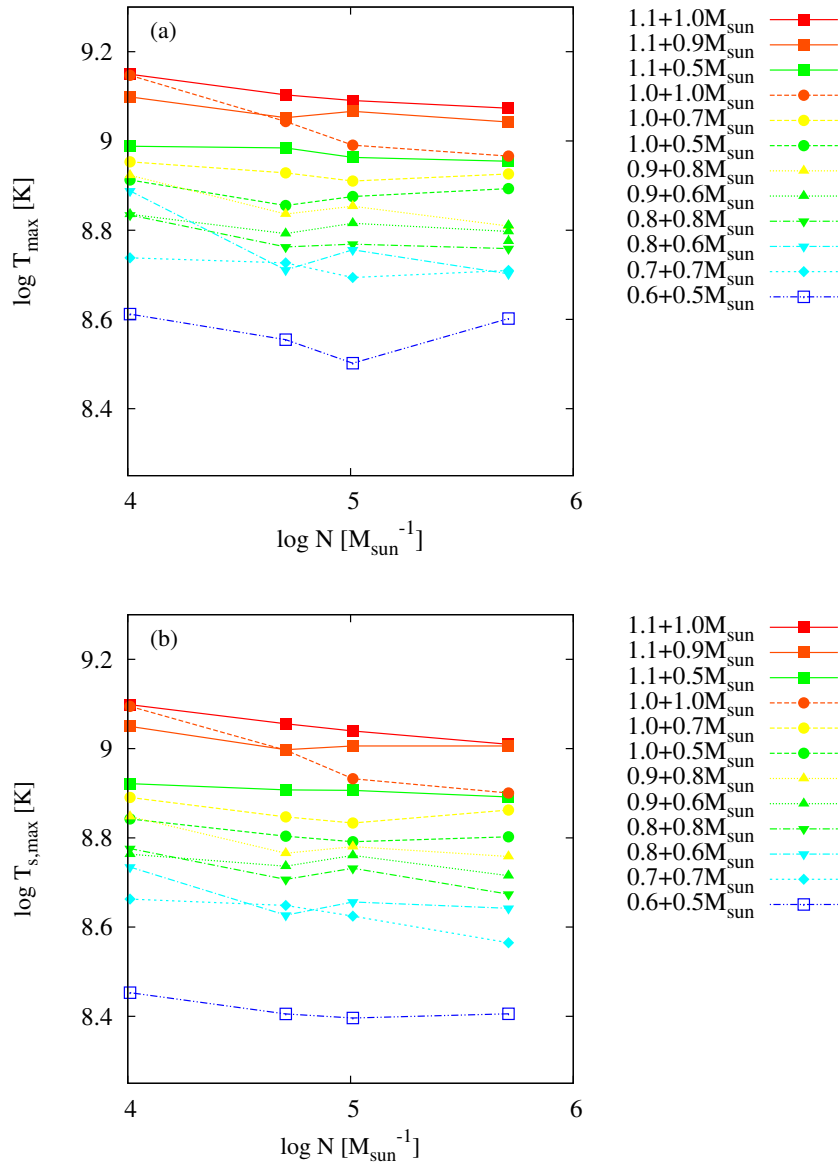


FIGURE 4.2: Similar to Figure 4.1 but for the remnant phase. (a) The highest raw temperature and (b) the highest smoothed temperature in the hot envelope of merger remnants at the end of remnant phase. These seem to converge against the numerical resolution. These figures are taken from Figure 10 of Sato et al. (2015).

4.2.1 Individual models

We mainly focus on the well studied models, $1.1 + 0.9 M_{\odot}$ and $0.9 + 0.6 M_{\odot}$ in this section.

The case of $1.1 + 0.9 M_{\odot}$

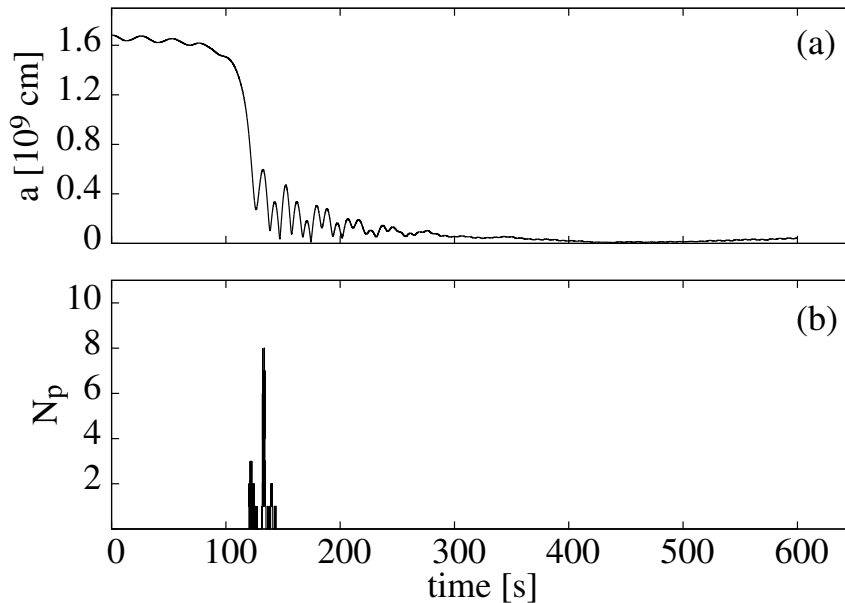


FIGURE 4.3: Time evolution of (a) the orbital separation and (b) the number of particles having high temperature ($\geq 2 \times 10^9$ K). The mass combination of WDs is $1.1 + 0.9 M_{\odot}$ and numerical resolution is $100k M_{\odot}^{-1}$. This figure is taken from Figure 6 of Sato et al. (2015).

At first, we compare our $1.1 + 0.9 M_{\odot}$ model with $100k M_{\odot}^{-1}$ (i.e., the total number of SPH particles is about 1.8×10^5) with that of Pakmor et al. (2012b) having a similar numerical resolution. We can confirm that morphological difference does not appear. Figure 4.3 shows the time evolution of (a) the orbital separation and (b) the number of hot particles whose temperature exceeds 2×10^9 K. We compare Figure 4.3 with results of Pakmor et al. (2012b)³.

It should be noted that WDs in our model merge more quickly (about 100 s) than those in Pakmor et al. (2012b) with their "exact" initial condition (about 600 s) although we adopt a similar initial condition to their "exact" one (see Section 2.3). This is because our initial separation ($\sim 1.67 \times 10^9$ cm) is less than that of Pakmor et al. (2012b) ($\sim 1.93 \times 10^9$ cm). Indeed, the time evolution of the binary separation in Figure 4.3 (a) resembles a case of their smaller initial separation (called the "approximate" initial condition in that paper), rather than a case with the "exact" one. We suppose that the main reason of this difference is relaxation methods of a single WD. As mentioned in Section 2.3.1, we relax a single WD with a velocity-dependent damping force but without time evolution of internal energy.

³Figure 4 and Table 1 in Pakmor et al. (2012b) should be compared with ours. Our model resembles their model with 1.8×10^5 particles and the approximate initial condition.

We fix our damping timescale by the end of this initial set up of a single WD. On the other hand, Pakmor et al. (2012b) changed the timescale and formulation of their damping force as it gradually decreases⁴. When we adopt similar relaxation method to Pakmor et al's, the radii of relaxed WDs are a few percent larger than our original ones. As a result, the initial separations where the RLOF starts would become larger than ours and they result in a longer merging time.

If the initial separation becomes smaller, mass transfer tends to occur more violently and the secondary is completely disrupted within a few orbital periods (Dan et al., 2011). As a result, accreted matter are more strongly heated by a shock and ensuing compression. The dynamical carbon burning would ignite more easily. Although Pakmor et al. (2012b) concluded that the initial condition is not so important for the dynamical carbon burning as the numerical resolution, we should note that our maximum temperatures in the dynamical merger phase could be overestimated. In other words, our identifications of the violent merger scenario might be slightly optimistic.

The case of $0.9 + 0.6 M_{\odot}$

We also compare our results of $0.9 + 0.6 M_{\odot}$ and $100k M_{\odot}^{-1}$ with models having the same mass combination as in Yoon et al. (2007), Dan et al. (2011), and Zhu et al. (2013). Since these studies applied similar numbers of SPH particles (about a few $\times 10^5$), they are suitable for comparison, although structures of merger remnants are considered to be insensitive to the numerical resolution (Section 4.1). Figure 4.4 describes (a) the time evolution of the orbital separation, (b) that of the maximum temperature, and (c) density and temperature profiles of a merger remnant at the almost quasi-stationary state, for $0.9 + 0.6 M_{\odot}$ with $100k M_{\odot}^{-1}$. In Figure 4.4 (c), the colors indicate temperature, and the white contours do density on the logarithmic scale. The most inner contour corresponds to 10^6 g cm^{-3} , while the most outer one does 10^2 g cm^{-3} . Each step between contours is $10^{0.5}$. The highest temperature is about $6 \times 10^8 \text{ K}$ when the merger remnant approaches a quasi-stationary state ($\geq 400 \text{ s}$), and this is consistent with the above three previous studies. The profiles of density and temperature of the merger remnant are also similar among all the studies including ours.

We compare the maximum temperature of our $0.9 + 0.6 M_{\odot}$ model in the dynamical merger phase with that of Yoon et al. (2007)⁵. Their maximum temperature (about $1.7 \times 10^9 \text{ K}$) is higher than ours (about $1.2 \times 10^9 \text{ K}$), although dynamical carbon burning does not occur in the both cases. We suppose that difference of the maximum temperature comes from that of the initial conditions, as also discussed in Dan et al. (2011) and Dan et al. (2014). In Yoon et al. (2007), they constructed CO WDs without spins, and their relaxation process of a binary system is relatively rough, while we assume the spin-orbit synchronization and relax CO WD binaries more carefully (see Section 2.3). Mass transfer becomes more violently in a binary

⁴We can find these differences if we compare our Equation 2.32 with Equation 14 of Pakmor et al. (2012b).

⁵See Figure 4 in Yoon et al. (2007) for comparison of our Figure 4.4 (a).

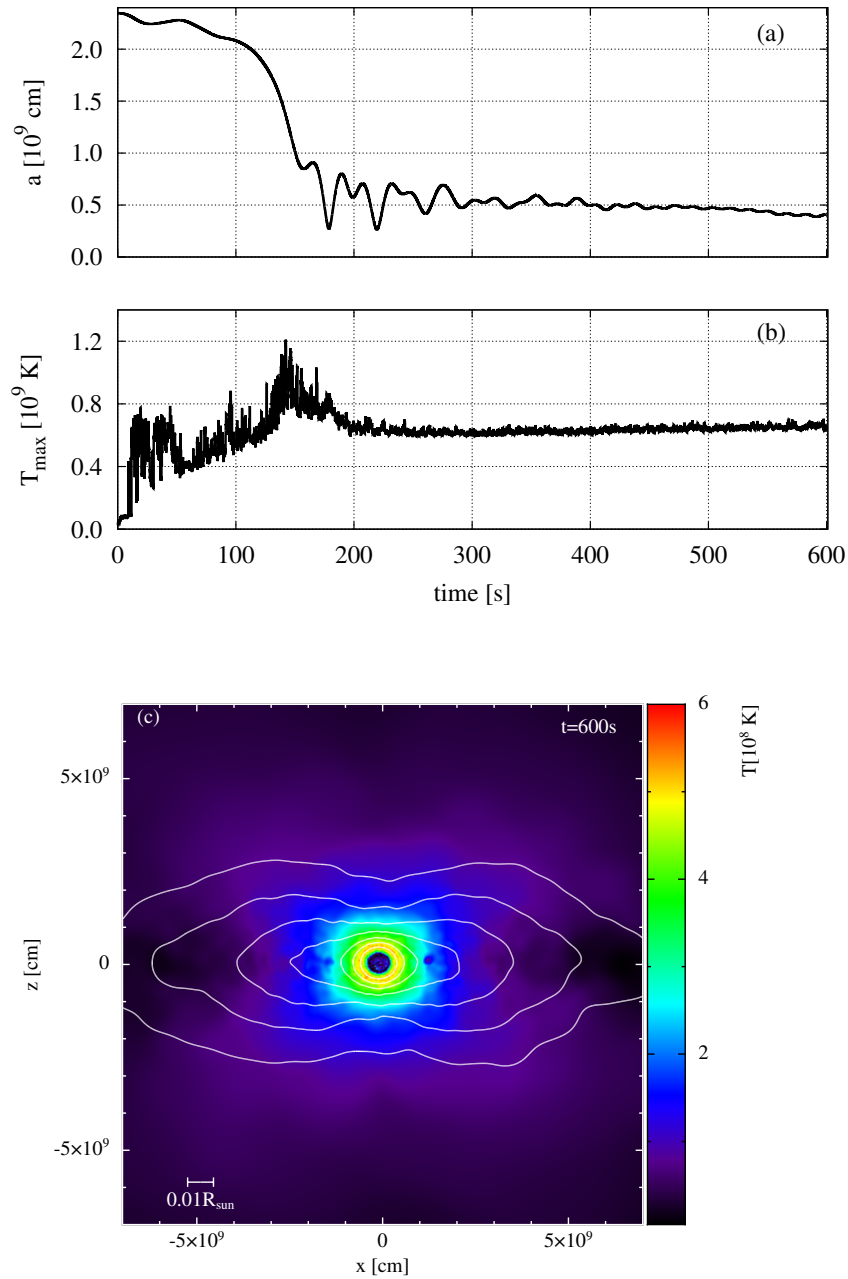


FIGURE 4.4: The time evolution of (a) the orbital separation and (b) the highest temperature. Its mass combination is $0.9 + 0.6 M_{\odot}$ and numerical resolution is $100k M_{\odot}^{-1}$. (c) Temperature profile of the merger remnant with density contours ranging from 10^2 g cm $^{-3}$ to 10^6 g cm $^{-3}$.

relaxed roughly, and velocity differences between accreted matter and surface of the primary WD are larger in a non-synchronized system than synchronized one. As a result, in the dynamical merger phase, temperature near the surface of the primary would increase.

Although our initial condition is referred to Dan et al. (2011), our initial separation of $0.9 + 0.6 M_{\odot}$ (about 2.4×10^9 cm) is smaller than that of Dan et al. (2011). Because the initial condition of Dan et al. (2011) is almost same as Pakmor et al. (2012b), we suppose that the difference of the initial separation between ours and theirs is caused by the same reason as that discussed in the previous section, i.e., the method of relaxing a single WD. We find that temperature of hot envelope in the merger remnant is almost the same as that of Dan et al. (2011). Therefore, the occurrence of off-center carbon burning would be not affected significantly. A similar discussion appeared in Tanikawa et al. (2015). However, Dan et al. (2011) reported that the morphological structure of a merger remnant could be affected by the initial condition. They found that a remnant whose initial separation is larger has a longer trailing arm than one whose initial separation is smaller⁶. This is because initial angular momentum of a merger system becomes larger in a longer initial separation. We find that our merger remnant of $0.9 + 0.6 M_{\odot}$ has a similar trailing arm to that of the smaller initial separation case of Dan et al. (2011).

According to Zhu et al. (2013) and Dan et al. (2014), initial spin states of WDs could also affect the structure of a merger remnant, especially for mergers of CO WDs with nearly equal masses. Zhu et al. (2013) and Dan et al. (2014) performed merger simulations of non-spinning WDs whose mass ratio is almost unity, and found that the structure of such merger remnants are different from those in mergers of synchronized systems. In the non-spinning cases, high temperature regions are formed near the center of the merger remnant, and carbon burning might occur in those regions consequently (van Kerkwijk et al., 2010). Since it is still uncertain whether a WD binary achieves synchronization until its merger, our results for the AIE and AIC scenarios might be slightly changed.

4.2.2 The critical mass ratio

Pakmor et al. (2011) performed several simulations of merging CO WD binaries and examined whether carbon detonation initiates in the dynamical merger phase, and the violent merger scenario succeeds. They obtained $q_{\text{cr}} \sim 0.8$ at $M_1 = 0.9 M_{\odot}$. Our results show a different value of $q_{\text{cr}} \sim 0.9$ at $M_1 = 0.9 M_{\odot}$. We present their models by open and filled squares in Figure 4.5. Their mass combinations are $M_1 = 0.9 M_{\odot}$ and $M_2 = 0.70, 0.76, 0.81, \text{ and } 0.89 M_{\odot}$. The filled squares indicate their models which satisfy their condition of carbon detonation (Seitenzahl et al., 2009). On the other hand, the open one could not satisfy that condition. We can find that our q_{cr} is larger for the violent merger scenario than that of Pakmor et al. (2011). This discrepancy could arise from differences in (1) inclusion of nuclear burning, (2) initial condition, and (3) numerical resolution. We discuss these three effects in this section. Using our q_{cr} , we

⁶See Figure 10 of Dan et al. (2011).

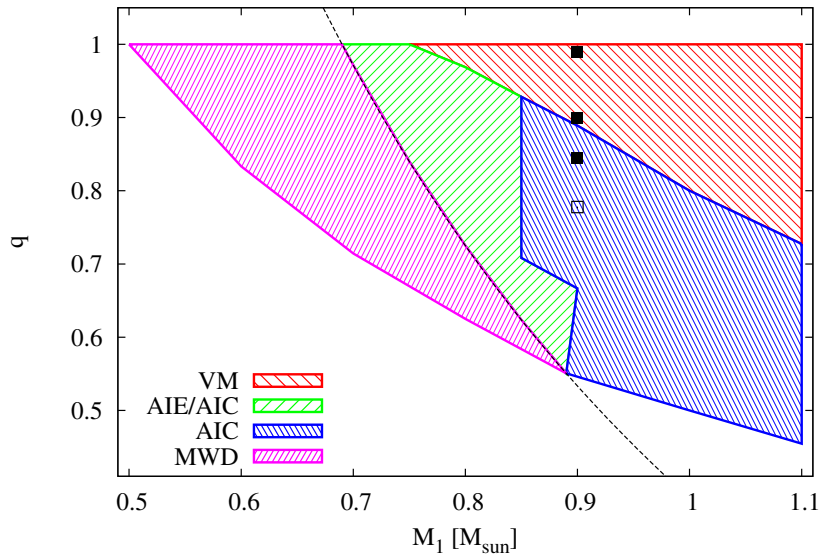


FIGURE 4.5: Same $M_1 - q$ diagram as Figure 3.11(a), but we include the results of Pakmor et al. (2011). The filled black squares are their models which satisfy their detonation condition, while the open black one is a model that does not.

also estimate the brightness distribution of the violent merger-induced SNe Ia, and compare our results with those of the previous study (Ruiter et al., 2013).

Nuclear burning

Inclusion of nuclear reactions is one of the largest differences between merger simulations in Pakmor et al. (2011) and ours, and leads to different results. The influence of nuclear reactions might be significant for identification of carbon detonation because Pakmor et al. (2011) found that particles with high temperature ($\geq 2 \times 10^9$ K) did not appear in $0.9 + 0.81 M_\odot$ without nuclear reactions. On the other hand, they appeared with nuclear reactions.

In order to evaluate the effect of nuclear energy release, we performed additional simulations, including nuclear burning, for some models whose mass ratios are slightly below our q_{cr} . Our numerical resolution is $500k M_\odot^{-1}$. In these simulations, we include only simple carbon burning, i.e., $^{12}\text{C} + ^{12}\text{C}$ reaction, to avoid large computational costs to solve a nuclear reaction network. Because the initiation of carbon detonation can be judged by this reaction, such a simple treatment of nuclear reactions would be sufficient for our purpose. We use the formulation of energy generation rate of carbon burning described as Equation 3.3 (Fowler et al., 1975; Blinnikov and Khokhlov, 1987).

Figure 4.6 represents comparison between our simulations with and without carbon burning for $0.9 + 0.8 M_\odot$. The red lines indicate a case with the carbon burning, while the black ones do one without. It shows the time evolution of (a) the orbital separation, (b) maximum temperature, and (c) energy generation release from the carbon burning. Although the orbital evolution is almost the same, the maximum temperature in the dynamical

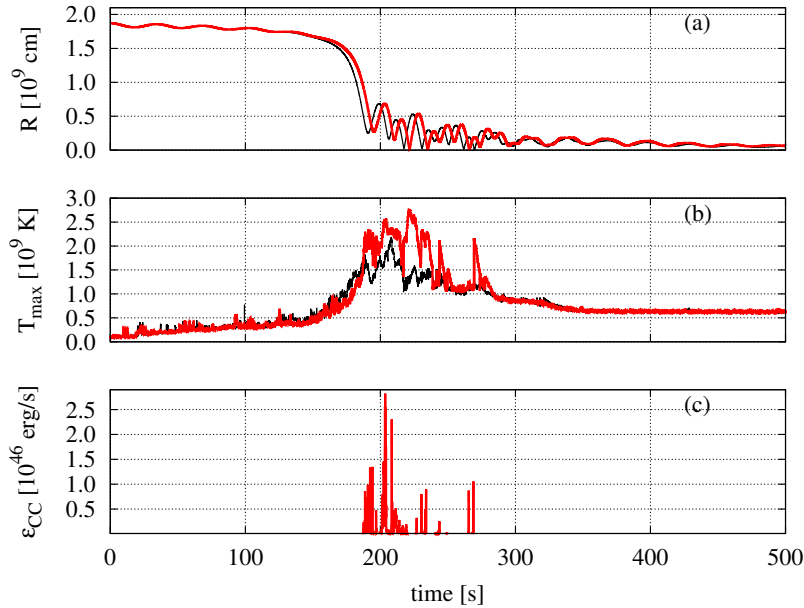


FIGURE 4.6: The time evolution of (a) the orbital separation, (b) the highest temperature, (c) the luminosity of carbon burning for a merger of $0.9 + 0.8 M_{\odot}$, with $500k M_{\odot}^{-1}$. The red lines indicate the case with carbon burning, while the black lines do the case without that. This figure is taken from Figure 7 of Sato et al. (2016).

merger phase is different. The maximum temperature in the case with carbon burning becomes higher than without that. We consider that this discrepancy would come from the nuclear reactions because the time when the carbon burning energy generation release becomes prominent is consistent with the time when peaks of temperature appear. Thus, we confirm that the inclusion of nuclear reactions increases the maximum temperature in the dynamical merger phase. Figure 4.7 is almost the same as Figure 3.4. It summarizes density and temperature of a particle which has the smallest $\tau_{\text{CC}}/\tau_{\text{dyn}}$ for all the models we resimulate, including the carbon burning. The symbols surrounded by black frames are results of models with the carbon burning. Comparing models without nuclear reactions, we find that those with the carbon burning generally move to higher temperature region.

On the other hand, we find that temperature of hot envelope of merger remnants does not have significant difference between models with and without the carbon burning. Therefore, inclusion of nuclear reactions would not affect ignition of off-center carbon burning in merger remnants.

We identify the initiation of carbon detonation in models with the carbon burning using the same condition without carbon burning. Then, we can expect that the inclusion of carbon burning lowers our q_{cr} of the violent merger scenario. We summarize the results of our merger simulations with the carbon burning in Figure 4.8. In Figure 4.8 (a), the green triangles are models with the carbon burning which satisfy our detonation condition, although they do not without the carbon burning. Thus, our expectation seems to be confirmed.

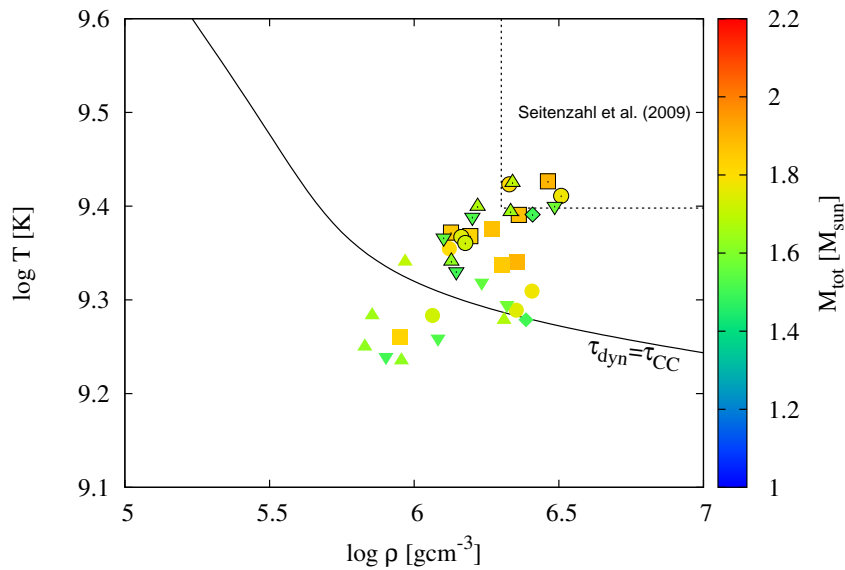


FIGURE 4.7: Same as Figure 3.4, but for models including the simple carbon burning. Colors and shapes of symbols have the same meanings as Figure 3.4. Symbols surrounded by black frames are models with carbon burning, while those without black frames are without. The black solid line depicts $\tau_{CC} = \tau_{\text{dyn}}$. The black dashed line is the demarcation of the carbon detonation condition by Seitenzahl et al. (2009). This figure is taken from Figure 8 of Sato et al. (2016).

However, our detonation condition, whether the dynamical carbon burning occurs, is considered under the situation without nuclear reactions, so it would no longer be valid in models including nuclear burning. Therefore, for direct comparison with the results of Pakmor et al. (2011), we adopt the same detonation condition as theirs, i.e., whether there are any particles satisfying $\rho > 2 \times 10^6 \text{ g cm}^{-3}$ and $T > 2.5 \times 10^9 \text{ K}$ (Seitenzahl et al., 2009), in the dynamical merger phase. That detonation condition is depicted as black dashed lines in Figure 4.7. Our results is presented in Figure 4.8(b). Although the boundary satisfying the detonation condition becomes slightly lower than that of Figure 3.5, their difference is small. Thus, we consider that our carbon detonation condition, i.e., whether SPH particles satisfy $\tau_{CC} < \tau_{\text{dyn}}$ during the dynamical merger phase, is plausible for models without nuclear reactions.

We derive similar approximated lines of $q_{\text{cr}}(M_1)$ in the cases with the carbon burning to those of the cases without, shown in Figure 3.6. Those are presented as dashed lines in Figure 4.9, where the red (blue) dashed line indicates an upper (lower) bound. $q_{\text{cr}}(M_1)$ with the carbon burning is slightly lower than without the carbon burning. The lower bound without the carbon burning (Equation 3.5) almost agrees with the upper bound including the carbon burning. Although q_{cr} is lowered due to inclusion of nuclear burning, our critical mass ratio for the violent merger scenario is still larger than that of Pakmor et al. (2011). Therefore, our results would not change essentially and the effect of nuclear reactions is not a main reason for the difference between our results and those of Pakmor et al. (2011).

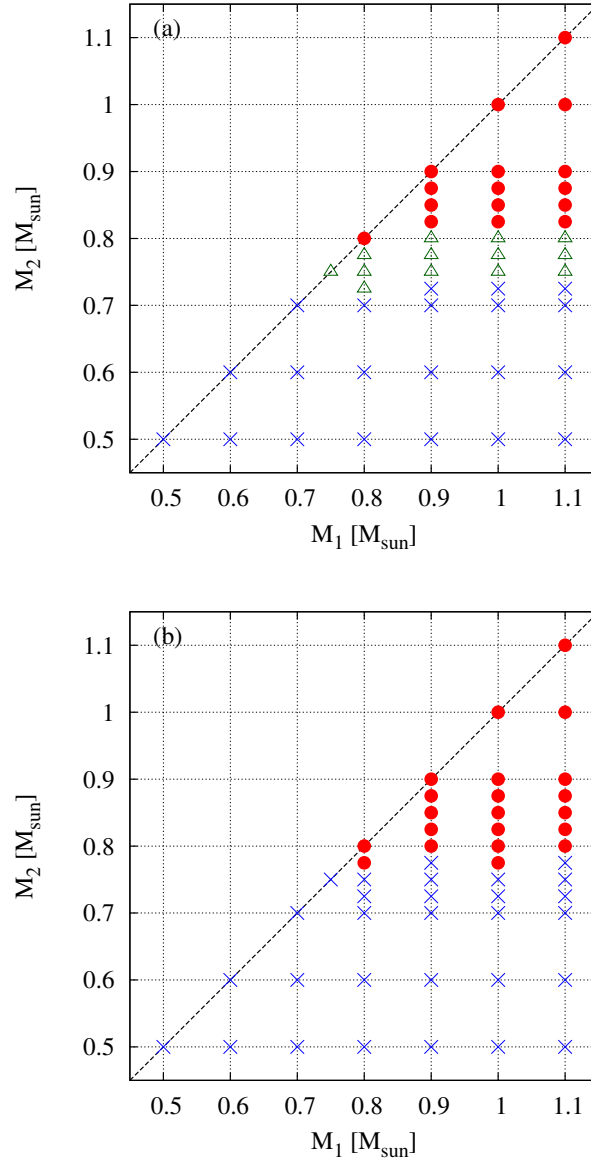


FIGURE 4.8: Similar $M_1 - M_2$ diagram to Figure 3.5, but for models including the carbon burning, (a) our detonation condition, (b) the condition of Seitenzahl et al. (2009). Red filled circles and blue crosses have the same meanings in Figure 3.5. Green triangles indicate models which satisfy our detonation condition with the carbon burning, although they do not satisfy the condition without the carbon burning. This figure is taken from Figure 10 of Sato et al. (2016).

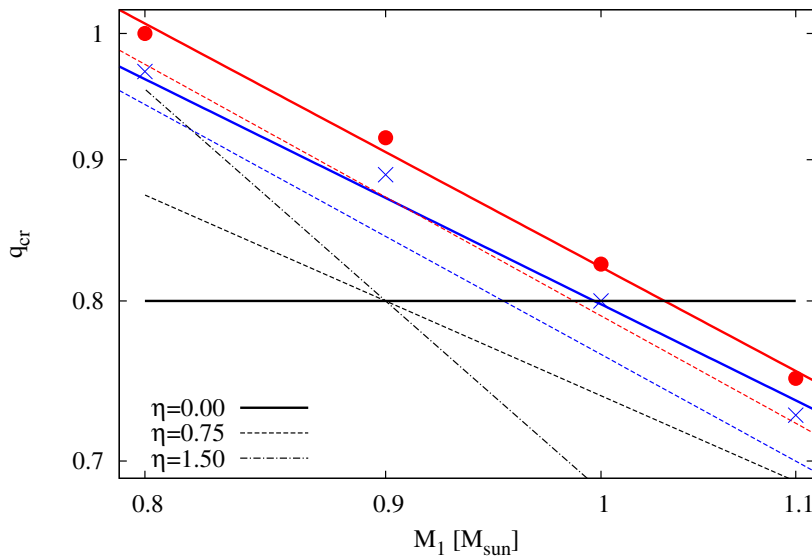


FIGURE 4.9: Same as Figure 3.6, but we add the results including nuclear reactions. The red and blue solid lines, red filled circles, and blue crosses have the same meanings as those in Figure 3.6. The red and blue dashed lines correspond to the approximated ones of the critical mass ratio for the violent merger scenario in the cases with the carbon burning. The red dashed line indicates an upper bound, while the blue one is a lower bound. $q_{\text{cr}}(M_1)$ adopted by Ruiter et al. (2013) are also depicted by the black solid, dashed, and dashed-dotted lines. See text for more details.

This figure is taken from Figure 5 of Sato et al. (2016).

Since our simulations include only a simple $^{12}\text{C} + ^{12}\text{C}$ reaction, the effect of nuclear burning might be underestimated. To check this effect, we perform post-processing calculations using an α -chain reaction network containing 13 species from ^4He to ^{56}Ni (Timmes and Arnett, 1999). Figure 4.10 shows the results for a particle which has the highest temperature in $0.9 + 0.8 M_{\odot}$. This calculation is done for a period in which the carbon burning continues. The red lines indicate a case including the α -chain reaction network, while green lines do one including only the carbon burning. Because we find essentially no difference between them, our simulations including only the carbon burning are appropriated to estimate the effect of nuclear burning, and being consistent with the previous studies using similar α -chain reaction networks (Pakmor et al., 2010; Pakmor et al., 2011; Pakmor et al., 2012a; Pakmor et al., 2012b; Dan et al., 2011; Dan et al., 2012; Dan et al., 2014; Raskin et al., 2012), at least until the initiation of detonation.

Initial condition

Next, we focus on the difference of initial conditions. Pakmor et al. (2011) used non-spinning WDs and set them at the initial separation where the RLOF just starts, which is derived from the approximate formulation of

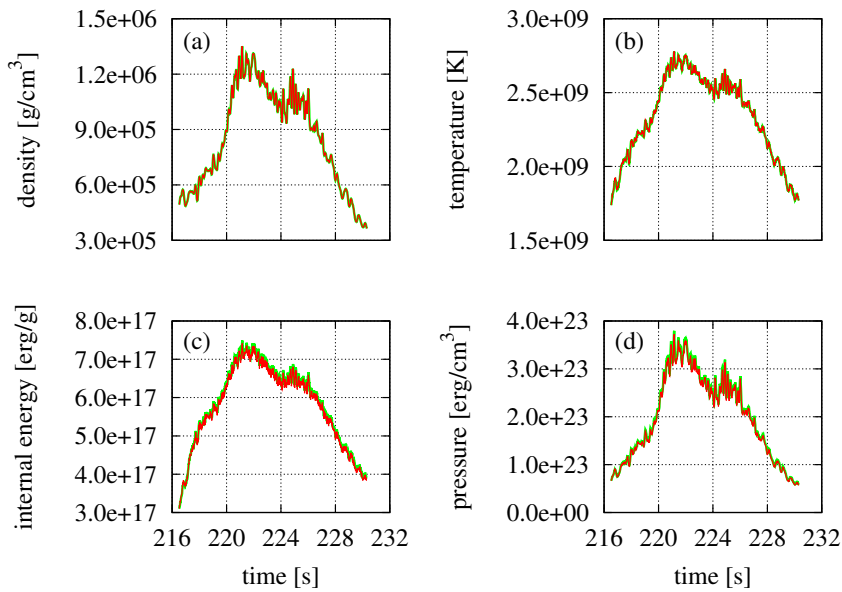


FIGURE 4.10: The results of post-processing calculation for $0.9 + 0.8 M_{\odot}$ model. We adopt a 13 species α -chain reaction network (Timmes and Arnett, 1999) to derive nuclear energy generation release. The green lines denote a case including only the carbon burning described as Equation 3.3, while the red lines indicate one including the reaction network. The time evolution of (a) density, (b) temperature, (c) specific internal energy, (d) pressure of a particle having the highest temperature. The period of this calculation is during the carbon burning turning on. This figure is taken from Figure 9 of Sato et al. (2016).

Eggleton (1983). In summary, they adopted the approximate initial condition as defined in Section 2.3. On the other hand, as also mentioned in Section 2.3, we assume that spins of WDs synchronize with their orbital motion, and set them at the initial separation expressed by Equation 2.34. We decrease the orbital separation with relaxing the WDs until the RLOF of the secondary WD starts.

In Pakmor et al. (2011), the secondary accretes onto the primary more violently than for cases adopting the same initial condition as ours (e.g., Rasio and Shapiro, 1995; Dan et al., 2011). Furthermore, in mergers of non-spinning WDs, accreting matter has larger velocity differences from the primary's surface than those of synchronous systems. As a result, temperature near the surface of the primary increases (see also Section 4.2.1). Therefore, carbon detonation would occur easily in the initial condition adopted by Pakmor et al. (2011), compared with our initial setups.

We examine a merger of $0.9 + 0.75 M_{\odot}$ in an initial condition similar to that of Pakmor et al. (2011)⁷. Figure 4.11 shows the time evolution of (a) the orbital evolution, (b) the maximum temperature. The black lines indicate the case adopting the Pakmor et al.'s initial condition (labeled "No-Sync"),

⁷We adopt the same numerical resolution as $500k M_{\odot}^{-1}$ and do not include any nuclear reactions.

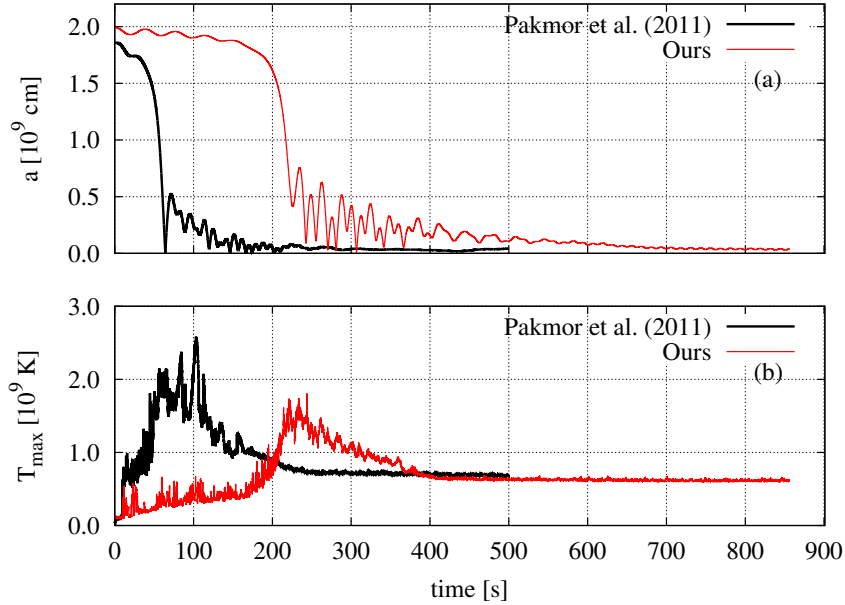


FIGURE 4.11: The results of $0.9 + 0.75 M_{\odot}$ for the two cases with the initial condition of ours (red lines) and Pakmor et al. (2011) (black lines). The time evolution of (a) the orbital separation and (b) the highest temperature.

while the red ones do one with our initial condition (labeled "Sync"). In Figure 4.11 (a), the initial orbital separation of the Pakmor et al.'s initial condition is about 7% less than that of our initial condition. We also note that the orbital evolution is much more rapid in the Pakmor et al.'s initial condition than ours, which implies that more violent mass transfer occurs. Figure 4.11 (b) shows that the maximum temperature during the dynamical merger is highly enhanced in the Pakmor et al.'s initial condition. Therefore, carbon detonation could occur easily. Figure 4.12 represents density and temperature of a particle which takes the minimum $\tau_{CC}/\tau_{\text{dyn}}$ for the both cases. We can see that a symbol of our initial condition (red triangle) lies below the line $\tau_{CC} = \tau_{\text{dyn}}$, so the dynamical carbon burning does not occur in this model. However, in the case of the Pakmor et al.'s initial condition, because its symbol (black triangle) locates above $\tau_{CC}/\tau_{\text{dyn}}$ line, the dynamical carbon burning occurs and would ignite carbon detonation. Adopting the Pakmor et al.'s initial condition, we find that 16 particles which satisfy our carbon detonation condition in the dynamical merger phase appear, although such particles do not when we use our original initial condition (see Figure 3.5).

From the above discussion, we conclude that the initial condition would have large impact on the estimate of q_{cr} . Although no definite conclusion has been reached yet, the several numerical studies suggest that close WD binaries would reach synchronization before they merge due to angular momentum dissipation by tidally excited gravity waves (e.g., Fuller and Lai, 2014, and references therein)

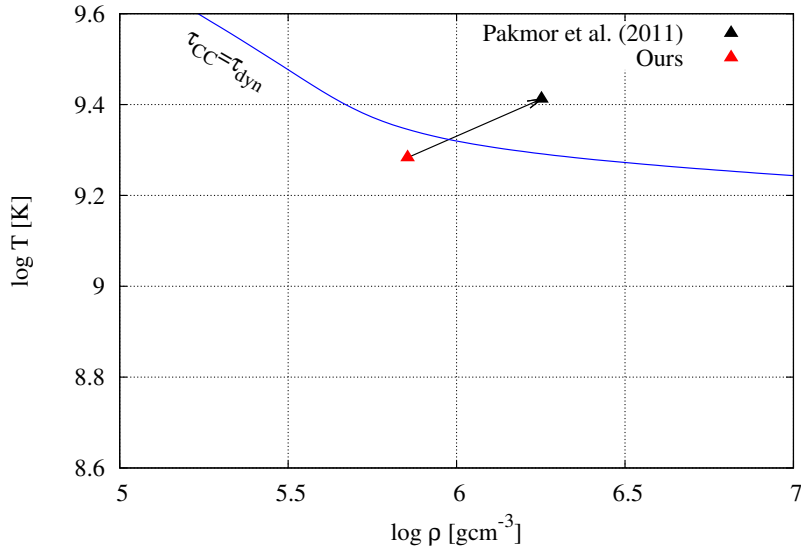


FIGURE 4.12: Density and temperature of a particle which has the minimum τ_{CC}/τ_{dyn} ratio in $0.9 + 0.75 M_{\odot}$ with $500k M_{\odot}^{-1}$. The red triangle corresponds to the model with our initial condition. The black one is the model with the initial condition of Pakmor et al. (2011). The blue solid line depicts $\tau_{CC} = \tau_{dyn}$.

Numerical resolution

As discussed in Section 4.1, numerical resolution might also cause the difference. Figure 4.1 indicates that the maximum temperature and the minimum τ_{CC}/τ_{dyn} ratio do not converge in the range of $10k \sim 500k M_{\odot}^{-1}$. This is because smaller hot regions can be resolved as the numerical resolution becomes higher. Pakmor et al. (2011) performed their fiducial models with $\sim 10^6 M_{\odot}^{-1}$, which is about double of ours. They also reported that the number of high temperature ($\geq 2 \times 10^9$ K) particles increases with the numerical resolution. Therefore, their simulations might resolve smaller structures having higher temperature than ours.

In order to check that, we perform merger simulations with numerical resolutions higher ($1000k M_{\odot}^{-1}$, $2000k M_{\odot}^{-1}$) than our standard one ($500k M_{\odot}^{-1}$) for $0.8 + 0.775 M_{\odot}$, $0.9 + 0.8 M_{\odot}$, $1.1 + 0.8 M_{\odot}$ WDs. Our numerical results are summarized in Figure 4.13. The maximum temperature (the minimum τ_{CC}/τ_{dyn} ratio) still increases (decreases) except for $0.8 + 0.775 M_{\odot}$ as the numerical resolution increases. This trend is consistent with Figure 4.1 and indicates that our results have not yet been fully converged, up to $2000k M_{\odot}^{-1}$ at least. Therefore, our critical mass ratio could be slightly lower than Equation 3.5, although the effect of higher numerical resolutions seems to be less than that of the initial condition and nuclear reactions in the range of $500k M_{\odot}^{-1} \sim 2000k M_{\odot}^{-1}$.

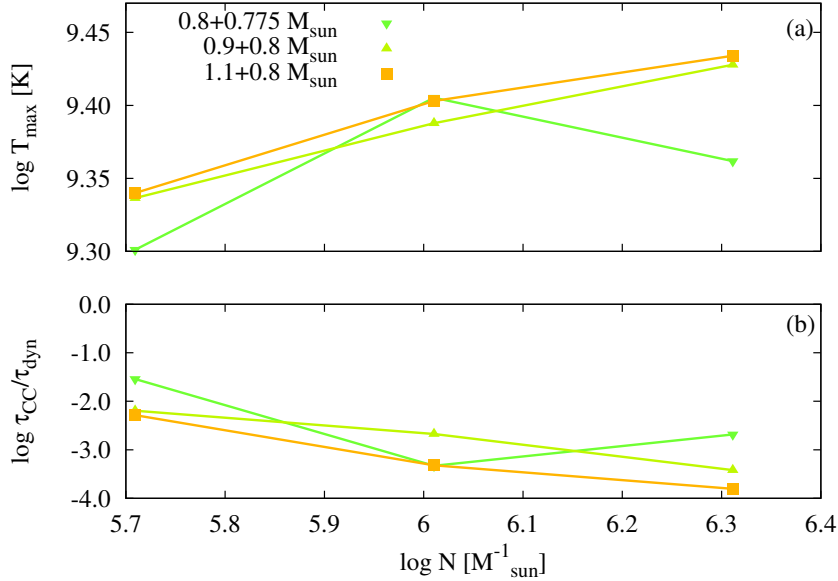


FIGURE 4.13: Numerical dependence of (a) the maximum temperature and (b) the minimum $\tau_{\text{CC}}/\tau_{\text{dyn}}$ ratio in the dynamical merger phase. Their resolutions are $500k, 1000k, 2000k$ per 1 solar mass. Its general tendency is consistent with that presented in Figure 4.1. Colors and shapes of symbols have the same meanings as in Figure 3.5. This figure is taken from Figure 6 of Sato et al. (2016).

Brightness distribution of the violent merger-induced SNe Ia

Using the results of Pakmor et al. (2011) and the binary population synthesis (BPS) calculation (Ruiter et al., 2011), Ruiter et al. (2013) estimated the peak brightness distribution of SNe Ia arising from the violent merger scenario. They found that their brightness distribution could be qualitatively consistent with an observational study (Li et al., 2011b). They adopted the value of $q_{\text{cr}} = 0.8$ at $M_1 = 0.9 M_{\odot}$ from Pakmor et al. (2011), and assumed

$$q_{\text{cr}}(M_1) = \min \left[0.8 \left(\frac{M_1}{0.9 M_{\odot}} \right)^{-\eta}, 1.0 \right], \quad (4.1)$$

where they applied $\eta = 0.0, 0.75, 1.5$. We add these three cases as black lines in Figure 4.9. The black solid line corresponds to $\eta = 0.0$, the black dashed one is $\eta = 0.75$, and the dashed-dotted one is $\eta = 1.5$. Figure 4.9 indicates that our $q_{\text{cr}}(M_1)$ is basically larger than those assumed in Ruiter et al. (2013). Although Ruiter et al. (2013) reported that the most potent factor determining the brightness distribution is mass of the primary WD in the violent merger scenario, the difference in the critical mass ratio could have influence on the distribution. Therefore, we investigate that here.

In order to examine how our q_{cr} would affect the brightness distribution of the violent merger SNe Ia, we adopt the same assumptions as in Ruiter et al. (2013) except for q_{cr} , and their BPS results. For the primary of merging WDs, we use the same mass distribution as Ruiter et al. (2011) and Ruiter et al. (2013), although it is highly uncertain whether a CO WD can increase its mass by avoiding formation of a common envelope during

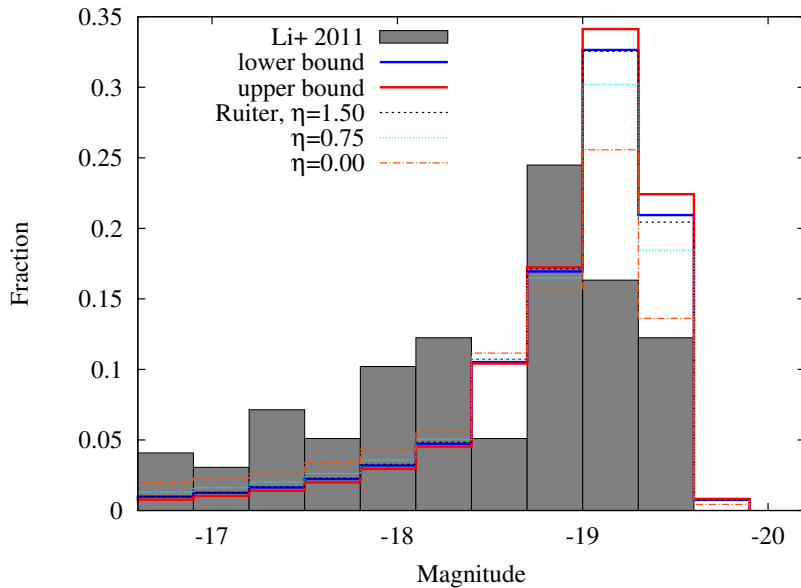


FIGURE 4.14: The peak brightness distribution of SNe Ia originating from the violent merger scenario, which are derived from our and Ruiter et al. (2013)’s $q_{\text{cr}}(M_1)$. The blue (red) histogram depicts a result derived from the lower (upper) bound of our $q_{\text{cr}}(M_1)$. The black, cyan, orange histograms indicate products using the hypothetical $q_{\text{cr}}(M_1)$ of Ruiter et al. (2013). They correspond to $\eta = 1.5$ (black), $\eta = 0.75$ (cyan), $\eta = 0.0$ (orange), respectively (see text for more details). We also show an observational result obtained from LOSS, which is described as the gray histogram. Magnitudes of models are bolometric, while those of LOSS are in R -band.

very rapid mass accretion from its He star companion. We also assume the same relation between mass of exploding WDs (m_{WD}) and the bolometric magnitude (M_{bol}) of SNe Ia as Ruiter et al. (2013)⁸. They derived a relation from the results of Sim et al. (2010), which performed 1D hydrodynamical simulations of sub-Chandrasekhar CO WD explosions by pure detonation. Sim et al. (2010) covered the mass range of WDs from $0.81 M_{\odot}$ to $1.15 M_{\odot}$, and showed that their peak luminosities are almost consistent with those of the violent merger SNe Ia (Pakmor et al., 2010; Pakmor et al., 2012a). We assume a flat mass ratio distribution of DD systems for simplicity although the distribution obtained from the BPS of Ruiter et al. (2011) is unknown. Because our interest is the impact on SN Ia brightness distribution comes from q_{cr} , the assumption of a simple mass ratio distribution is sufficient for our purpose.

Using the above assumptions and our and Ruiter et al. (2013)’s q_{cr} , we calculate the peak brightness distribution of the violent merger SNe Ia. Figure 4.14 presents the results. The red solid line indicates a result assuming the upper bound of our q_{cr} described in Equation 3.4, while the blue one corresponds to our lower bound in Equation 3.5. The results for q_{cr} of Ruiter et al. (2013) are depicted by the orange dashed-dotted ($\eta = 0.0$ in

⁸The detailed relation can be confirmed in Figure 4 and the appendix of Ruiter et al. (2013).

Equation 4.1), cyan dotted ($\eta = 0.75$), and black dashed ($\eta = 1.5$) lines. Comparing the brightness distribution of our q_{cr} with that of Ruiter et al. (2013), we find that there is no significant difference between them. This fact implies that the critical mass ratio is not so crucial for the brightness distribution of the violent merger SNe Ia, as reported in Ruiter et al. (2013). As Pakmor et al. (2010) and Pakmor et al. (2012a) presented, only the primary CO WD is converted to radioactive nickel by detonation, while the secondary produces intermediate elements. This is because, in the violent merger scenario, the brightness distribution of SNe Ia is not sensitive to q_{cr} , but mainly determined by the mass of the primary WD.

From Figure 4.14, our results are closest to $\eta = 1.5$ among the three cases of Ruiter et al. (2013). Using our q_{cr} and Ruiter et al.'s $\eta = 1.5$, the brightness distribution relatively concentrates around $M_{\text{bol}} = -19.0$.

For comparison, we add an observational volume-limited brightness distribution gray histogram nearby SNe Ia derived by the Lick Observatory Supernova Search (Li et al., 2011b, LOSS). Comparing our estimates with the observational result, the diversity of SN Ia luminosity can be explained, but there are some discrepancies. For example, the fraction of faint events ($M_{\text{bol}} > -19.0$) in our models is lower than that of the LOSS. This difference might decrease if we consider viewing angle effect arising from strong asymmetry of the violent merger SNe Ia (see also Ruiter et al., 2013), which might be increasingly important for large mass ratios⁹. Of course, there are large uncertainties for the observational SN Ia brightness distribution and our models are too simple to be compared with the observations. Therefore, a definitive conclusion may not be derived from this study.

As the mass ratio is approaching unity, the primary is more strongly deformed by the secondary at merging. As a result, the central density of the primary becomes lower. Because nucleosynthesis in SN Ia explosions is so sensitive to density profile near the center of the primary in the violent merger scenario, the amount of ^{56}Ni in the violent merger would decrease, while this effect is not accounted here (see also Kromer et al., 2013b).

4.2.3 Other parameter surveys

Dan et al. (2012), Dan et al. (2014), and Zhu et al. (2013) performed similar parameter surveys for mergers of WD binaries using their SPH codes¹⁰. Dan et al. (2012) and Dan et al. (2014) found that the dynamical carbon burning does not occur in their models, unless M_1 and M_2 are very massive, i.e., $\geq 1 M_{\odot}$ (see Figure 12 in Dan et al., 2014). They also showed that no model satisfies the condition of carbon detonation by Seitenzahl et al. (2009) (see Figure 9 in Dan et al., 2012). Their results seem to be different from ours since less massive CO WD binaries could ignite the dynamical carbon burning, as described in Figure 3.4. We consider that this discrepancy comes from two factors, the initial condition and numerical resolution.

⁹Here, the large mass ratio means close to unity.

¹⁰Dan et al. (2014) used the same results as those of Dan et al. (2012).

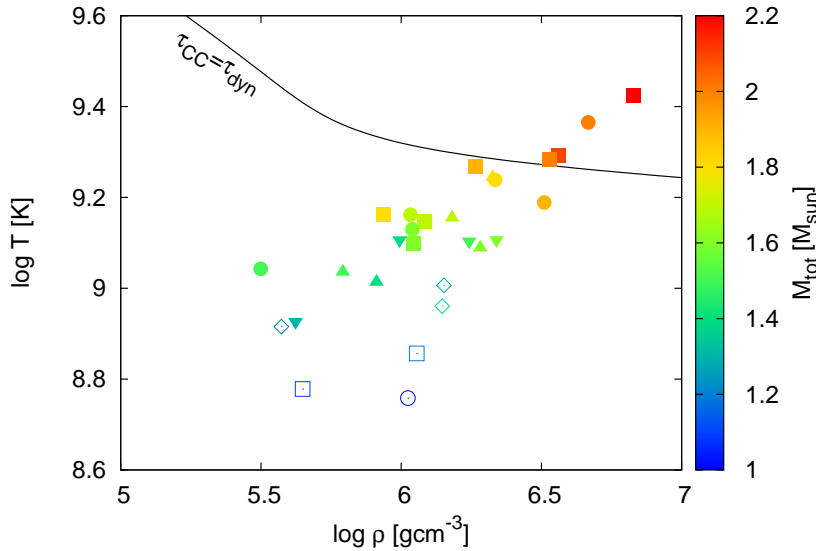


FIGURE 4.15: Same as Figure 3.4, but in models with lower numerical resolution ($10k M_{\odot}^{-1}$) than that of Figure 3.4 ($500k M_{\odot}^{-1}$). The colors and shapes have the same meanings in Figure 3.4. The black line indicates $\tau_{CC} = \tau_{dyn}$.

As discussed in Section 4.2.1 and 4.2.2, our initial orbital separation is generally smaller than that of Dan et al. (2012) and Dan et al. (2014) due to slightly different relaxation methods of a single WD. Mass transfer tends to become more violent as the initial separation is decreasing. Temperature of hot regions formed during the dynamical merger phase increases, and the dynamical carbon burning occurs easily (see discussion in Section 4.2.2).

Moreover, the numerical resolution of our standard models, $500k M_{\odot}^{-1}$, is about twenty times larger than that of Dan et al. (2012) and Dan et al. (2014), $\sim 2 \times 10^4 M_{\odot}^{-1}$. As we discuss in Section 4.1 (and a part of Section 4.2.2), since a higher numerical resolution can resolve smaller high temperature regions, temperature of the regions would become higher, and the dynamical carbon burning could occur easily.

As a result, the number of merger models which can satisfy the condition of carbon detonation would be larger in our simulations than Dan et al. (2012) and Dan et al. (2014). In order to check the influence of numerical resolution, we present results of our simulations with much lower resolution $10k M_{\odot}^{-1}$ in Figure 4.15, which is the same as Figure 3.4. We can confirm that less models can satisfy the necessary condition of dynamical carbon burning, i.e., $\tau_{CC} < \tau_{dyn}$, than our standard models represented in Figure 3.4. We also find that models leading to the dynamical carbon burning in the lower resolution are very massive ones ($M_1, M_2 \geq 1 M_{\odot}$).

Zhu et al. (2013) performed their merger simulations with $\sim 2 \times 10^5 M_{\odot}^{-1}$, which is almost a half of our standard models. They assumed non-spinning WDs and used the approximate initial condition (see discussion in Section 2.3 and 4.2.2). Therefore, as discussed above and in Section 4.2.2, the

initiation of carbon detonation would be easy, although they did not focus on the dynamical merger phase and identification of the violent merger scenario. As we mentioned in Section 4.2.1, the characteristics of merger remnants are not sensitive to the numerical resolution. They also do not depend on the initial condition significantly, at least in models with sufficiently smaller mass ratios than unity. On the other hand, in models with nearly equal masses, the structures of merger remnants are different between the initial conditions of Zhu et al. (2013) and ours (see also discussion in Section 4.2.1). However, the maximum temperature of hot envelope is not sensitive to the both numerical resolution and initial condition, as seen in Section 4.2.1. Therefore, for the identification of off-center carbon burning in the hot envelope of merger remnants, our results are consistent with theirs (see their Figure 17).

4.3 The final fate of Henize 2-428



FIGURE 4.16: Planetary nebula of Henize 2-428, which was obtained with the VLT; credited by ESO.

Henize 2-428 is a bipolar planetary nebula whose central system is recently claimed to be a super-Chandrasekhar DD binary (e.g., Rodríguez et al., 2001; Santander-García et al., 2015). This implies that Henize 2-428 might be one of the possible candidates of SN Ia progenitors in the DD scenario. Here, we predict the final fate of this system from its observational properties and our merger outcome diagram of CO WD mergers (Figure 3.11).

4.3.1 The observational properties of Henize 2-428

Henize 2-428 is a bipolar planetary nebula. It is suggested that a binary system exists at its center (e.g., Rodríguez et al., 2001). We present its optical image in Figure 4.16, which was observed by the Very Large Telescope (VLT), operated by the European Southern Observatory (ESO). All copyrights of that figure belong to ESO.

Recently, Santander-García et al. (2015) observed the Henize 2-428 at optical bands. They analyzed the light curve and spectra of its central system. From the depth of the light curve minima, intensities of two He II 541.2 nm absorption lines, and obtained radial velocity amplitudes, they interpreted the central system of Henize 2-428 as a DD (double post-AGB core) binary with nearly equal masses and effective temperatures¹¹. They estimated the total mass of the central DD system to be $1.8 M_{\odot}$, which exceeds the Chandrasekhar limit. They also derived the merging time of this system as 700 Myr from its orbital period of 0.176 days. Thus, the central system of Henize 2-428 can lose its angular momentum by radiating gravitational waves, and merge within the Hubble time. If their interpretation is correct, this is the first example of super-Chandrasekhar DD systems which can be a candidate of SN Ia progenitors in the DD scenario.

When we fix its mass ratio as unity, both the primary and secondary WDs in Henize 2-428 have an equal mass of $0.9 M_{\odot}$ (Santander-García et al., 2015). From our q_{cr} and Figure 3.11, such a system might be able to explode as an SN Ia in the violent merger scenario. In the next section, we investigate whether the core of Henize 2-428 leads to the violent merger-induced explosion, or produces other outcome.

4.3.2 Predicting the merger outcome of Henize 2-428

Although Santander-García et al. (2015) fixed mass ratio of the central system of Henize 2-428 at unity based on the similar depths of the light curve minima and radial velocity amplitudes, we derive possible ranges of the mass ratio and the primary's mass without fixing the mass ratio. We consider 1σ uncertainties of radial velocity amplitudes and orbital period presented in Santander-García et al. (2015). We calculate the mass ratio $q = M_2/M_1$ and the primary's mass of the DD core of Henize 2-428 using the following formulation (Eggleton, 2006),

$$\frac{q^3}{(1+q)^3}(M_1+M_2) = \frac{(1-e^2)^{3/2}}{2\pi G} V_1^3 P_{\text{orb}} \sin^{-3} \theta_i, \quad (4.2)$$

$$\frac{1}{(1+q)^3}(M_1+M_2) = \frac{(1-e^2)^{3/2}}{2\pi G} V_2^3 P_{\text{orb}} \sin^{-3} \theta_i, \quad (4.3)$$

where e is the eccentricity, V_i is the radial velocity amplitude, P_{orb} is the orbital period, θ_i is the inclination angle, and subscriptions of 1 and 2 indicate the primary and the secondary, respectively. From above equations, we can obtain,

$$q = V_1/V_2, \quad (4.4)$$

$$M_1 = \frac{(1-e^2)^{3/2}}{2\pi G} (1+q)^2 V_2^3 P_{\text{orb}}. \quad (4.5)$$

¹¹Although there are a few negative arguments against this conclusion due to the contradiction of its luminosity and temperature to theoretical evolution models of post-AGB cores (e.g., Frew et al., 2016; García-Berro et al., 2016), the definitive conclusion has not yet been reached because of uncertainties of binary evolution.

We use observational values cited by Santander-García et al. (2015), which are summarized in Table 4.1. Although the inclination angle has uncertainty, we fix it at $\theta_i = 64.7^\circ$. We find that our results are not changed essentially if we use different values within its uncertainty.

Here, we assume $e = 0$, i.e., a circular orbit. The central system would strongly interact with mass transfer, e.g., common envelope, if we consider that the bipolar morphology of Henize 2-428 was generated by its orbital motion. Therefore, its orbit would be sufficiently circularized by such strong interactions.

We show our result in Figure 4.17. The black point with error bars depicts the possible parameters of Henize 2-428. Even considering the uncertainties, the symbol of Henize 2-428 lies within the region of the violent merger scenario. Therefore, we conclude that the central DD core of Henize 2-428 is a possible progenitor of the violent merger SNe Ia.

Parameter	Value (Santander-García et al., 2015)
Orbital period P_{orb} (day)	0.1758 ± 0.0005
Radial velocity amplitude V_1 (km/s)	206 ± 12
Radial velocity amplitude V_2 (km/s)	206 ± 8
Inclination angle θ_i (degree)	64.7 ± 1.4

TABLE 4.1: The observational parameters of Henize 2-428, cited by Santander-García et al. (2015).

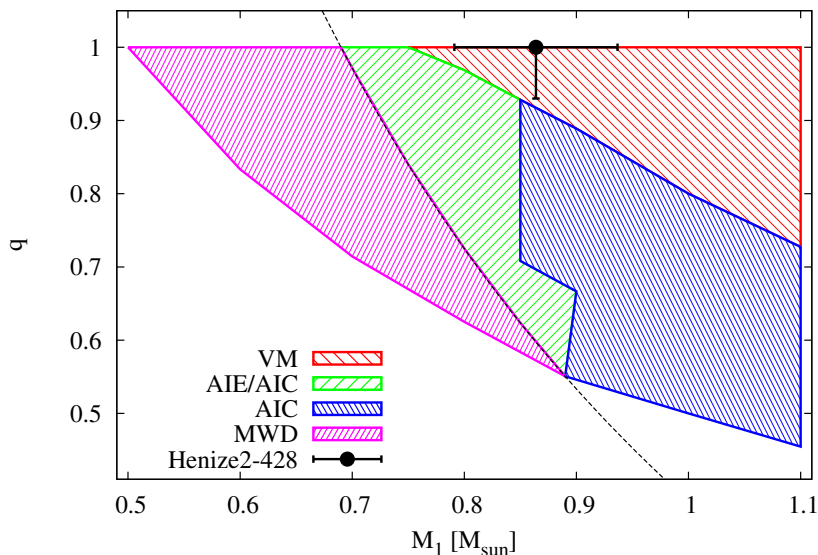


FIGURE 4.17: The same figure as Figure 3.11 (a). A black point indicates the M_1 and mass ratio of the central DD system in Henize 2-428 with 1σ error bar.

We briefly evaluate the predicted properties of the explosion of the DD core of Henize 2-428 in the violent merger scenario. In Figure 4.18, we show

the time evolution of (a) the orbital separation and (b) the maximum temperature of our $0.9 + 0.9 M_{\odot}$, which is the most similar mass combination to the observed values of Henize 2-428 ($0.89 + 0.89 M_{\odot}$) among our simulations. Here, we adopt the numerical resolution as $500k M_{\odot}^{-1}$. A black dashed vertical line indicates the time when the first particle satisfying our detonation condition appears (~ 351 s). We present the merger structure at the time in Figure 4.20, (a) SPH particles in the x-y plane and (b) x-z plane. The red filled circles are the position of the first detonation particle. Figure 4.19 depicts density profiles at the time along positive-x (red solid), negative-x (red dashed), positive-y (green solid), negative-y (green dashed), positive-z (blue solid), and negative-z axis (blue dashed). We set the origin of Figure 4.20 at the primary's center of mass. We find that the profiles have strong asymmetric structures, especially along negative-x axis due to the presence of the highly disrupted secondary WD. If carbon detonation successfully initiates at the first detonation particle (expressed as a red circle in Figure 4.19), and blows off the primary and secondary, the explosion would be observed as an asymmetric transient. Observing the polarization, typical SNe Ia are considered as highly symmetric explosions (e.g., Wang and Wheeler, 2008). Therefore, the asymmetry included in the density profiles of $0.9 + 0.9 M_{\odot}$ at the time of the explosion might be inconsistent with normal SNe Ia.

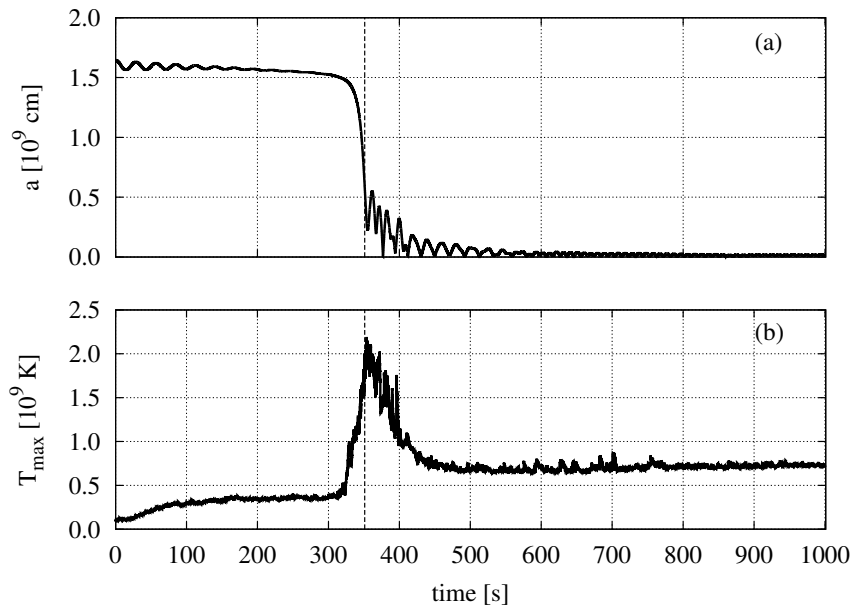


FIGURE 4.18: Time evolution of (a) the orbital separation and (b) the highest temperature of our $0.9 + 0.9 M_{\odot}$ with $500k M_{\odot}^{-1}$. Black vertical dashed lines show the time when the first detonation particle appears in the simulation (~ 351 s).

Pakmor et al. (2010) performed the simulations of a merger and explosion of $0.89 + 0.89 M_{\odot}$. They found that the explosion produces $\sim 0.1 M_{\odot}$ radioactive nickels, and its peak magnitude reaches ~ -17 mag. The observational properties of the explosion reproduce those of SN 1991bg-like SNe Ia. Although there are differences of initial conditions for merger simulations between our study and Pakmor et al. (2010), their results also showed

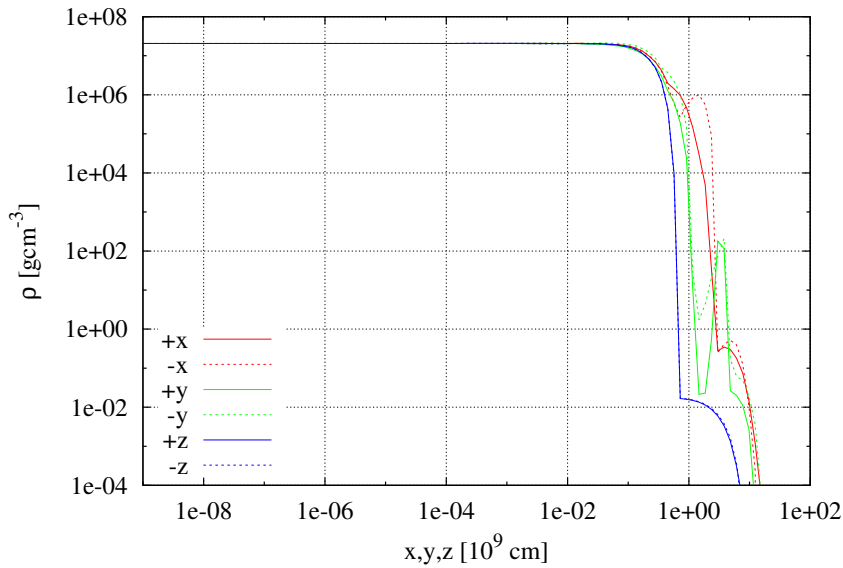


FIGURE 4.19: The density profiles of our $0.9 + 0.9 M_{\odot}$ at the time indicated as black dashed line in Figure 4.18 along each axis. The red/green/blue solid (dashed) line is positive(negative)-x/y/z axis.

deviations from a spherical symmetry. They reported that the asymmetry caused the viewing angle effect on the light curve, which becomes more conspicuous in bluer bands. The similar effect would appear in our model.

SN 2010lp is an SN 2002es-like SN Ia, which had the peak brightness $B_{\max} \sim -17.8$ mag and decline rate $\Delta m_{15,B} \sim 1.24$ (e.g., Taubenberger et al., 2013; Kromer et al., 2013b). It showed narrow O I emission lines with double peak profile in its late spectra (Taubenberger et al., 2013), although the spectra of typical SN 1991bg-like events are dominated narrow lines of iron group elements. This observational result indicates the presence of unburned oxygen near the center of the explosion, and the asymmetric distribution of oxygen. Kromer et al. (2013b) performed simulations of a violent merger SN Ia explosion of $0.9 + 0.76 M_{\odot}$, whose merger was simulated in Pakmor et al. (2011), although the mass combination could not lead to the violent merger SN Ia in our study (see Figure 3.5). They found that the peak brightness, decline rate, and early spectra of SN 2010lp could be explained by their model. Because their model left oxygen near the center and its distribution was highly asymmetric, the O I emission lines in the late spectra could be explained¹². Since the primary mass and morphological structure at the initiation of carbon detonation in our $0.9 + 0.9 M_{\odot}$ model are similar to their $0.9 + 0.76 M_{\odot}$ model, the DD core of Henize 2-428 might lead to the similar explosion to SN 2010lp, i.e., a subluminous SN Ia with the emission from oxygen in the late spectra. Kromer et al. (2013b) showed that the amount of ^{56}Ni synthesized in the explosion became smaller in $0.9 + 0.9 M_{\odot}$ (Pakmor et al., 2010) than in $0.9 + 0.76 M_{\odot}$ because tidal deformation, which is stronger in mergers with higher mass ratio, lowers the central density of the primary WD. Therefore, the SN explosion of Henize

¹²They did not calculate the late spectra of the model.

2-428 might be dimmer than SN 2010lp.

In summary, we expect that the explosion induced from the violent merger of the DD core of Henize 2-428 would be observed as a subluminoous SN 1991bg-like (or SN 2002es-like) SN Ia, and might show the emission lines of oxygen in its late spectra. Due to the asymmetric distribution of materials, it would show relatively stronger polarization than normal SNe Ia, and its observational properties might be affected by the viewing angle.

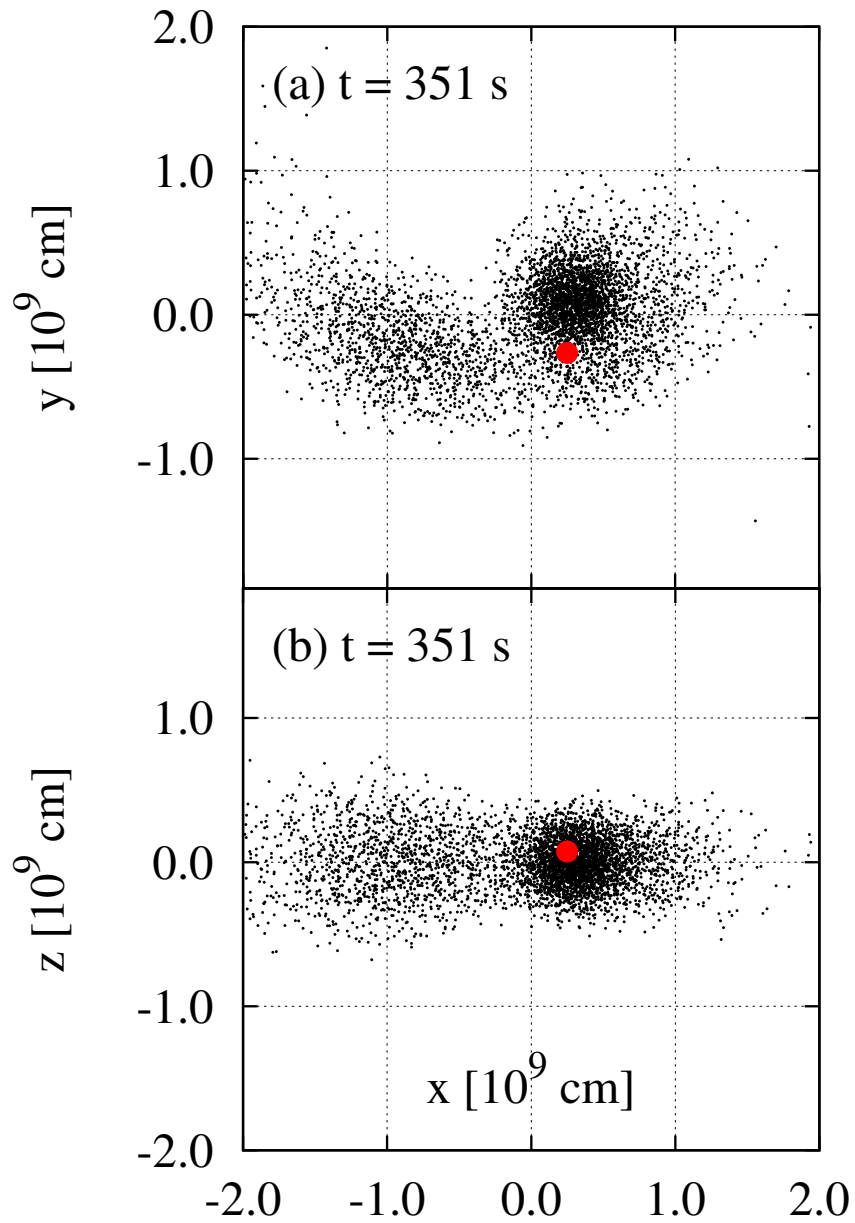


FIGURE 4.20: The structures of the merger of our $0.9 + 0.9 M_{\odot}$ model at the time indicated as black dashed lines in Figure 4.18. (a) x-y plane, (b) x-z plane. Red filled circles depict the location of the first detonation particle.

Chapter 5

Conclusion and Remarks

We perform 3D SPH simulations of mergers of CO WD binaries, examine products from the mergers, and discuss the possibility that it explodes as an SN Ia. Our simulations cover a wide mass range of $0.5 \sim 1.1 M_{\odot}$, have higher numerical resolution up to $500k M_{\odot}^{-1}$ than similar previous studies (Dan et al., 2012; Dan et al., 2014; Zhu et al., 2013), and adopt a plausible initial condition (Rasio and Shapiro, 1995; Dan et al., 2011). We follow CO WD mergers from the RLOF of the secondary to the formation of a quasi-stationary merger remnant. Using the results of our simulations, we obtain the following conclusions.

1. We investigate whether CO WD mergers ignite carbon detonation in the dynamical merger phase, and can explode as an SN Ia in the violent merger scenario in Section 3.2. We find that our models which have $M_1 > 0.8 M_{\odot}$ and $M_2 > 0.8 M_{\odot}$ can satisfy our detonation condition, and they would lead to the violent merger-induced SNe Ia. We derive the critical mass ratio, above which the violent merger would succeed, as a function of the primary mass. Those are expressed as Equations 3.4 and 3.5, and larger than that derived in Pakmor et al. (2011).
2. We also examine the occurrence of quiescent off-center carbon burning at the end of (early) remnant phase in Section 3.3, when a merger remnant is formed. We showed that off-center carbon burning ignites in hot envelope of a merger remnant when M_1 is larger than $0.9 M_{\odot}$ (in cases with the smoothed temperature, T_s defined as Equation 3.6). If carbon burning occurs off-center and $M_1 + M_2 \geq M_{\text{Ch}}$, a CO core of the merger remnant is converted to an ONeMg core, and eventually collapses into a neutron star along the AIC scenario, instead of explosion as an SN Ia. On the other hand, merger remnants without off-center carbon burning could increase its core mass by accretion of surrounding matter up to M_{Ch} , and would explode at last (the AIE scenario).
3. We summarize the merger outcomes in $M_1 - q$ diagram (Figure 3.11) using the results of our simulations in Section 3.4. The outcomes represented in this study are (1) the violent merger-induced SN Ia during the merger, (2) post-merger SN Ia explosion along the AIE, (3) gravitational collapse to a neutron star along the AIC, and (4) formation of

a single massive CO WD.

4. According to our $M_1 - q$ diagram, all CO WD mergers with a sub-Chandrasekhar mass could not explode as an SN Ia in the violent merger scenario. Because mergers of massive CO WD binaries having $> 2 M_\odot$ would explode as a violent merger-induced SN Ia or collapse to a neutron star along the AIC scenario, the DD model might be unable to explain super-Chandrasekhar SN Ia events, which are considered to have large amount of radioactive nickel $> 1 M_\odot$ and massive ejecta $> 2 M_\odot$.
5. We estimate the ratio of CO WD mergers leading to SNe Ia in the violent merger and the AIE to all the WD mergers, and found that it would be less than 8% under some assumptions. When we adopt results of some observational studies, contribution from SNe Ia originating from CO WD mergers to the entire Galactic SNe Ia is estimated as less than 10%. Therefore, it might be unlikely that mergers of CO WD binaries are the main progenitors of SNe Ia. We should consider other possible scenarios, such as He double detonation scenario (Nomoto, 1982b; Livne, 1990), if we explain SNe Ia by the DD model. However, having large uncertainties, our estimate might change sufficiently due to future studies and definitive conclusions have not been achieved yet.
6. We examine the numerical convergence of our simulations in the range of resolution $10k \sim 500k M_\odot^{-1}$ in Section 4.1. We find that the results of our simulations in the dynamical merger phase depend on the number of SPH particles, while those of merger remnants do not. Such tendencies were already reported in the several previous studies (e.g., Pakmor et al., 2011; Raskin et al., 2012). Therefore, the identification of the violent merger scenario might be slightly changed in future simulations of CO WD mergers with much higher resolution. We have to keep that in mind when we interpret our study.
7. We compare our results with those of previous studies in Section 4.2, for our $1.1 + 0.9 M_\odot$ and $0.9 + 0.6 M_\odot$ models. Because our initial condition provides slightly smaller initial orbital separations than those of Dan et al. (2011) and Pakmor et al. (2012b), which adopted similar initial condition and performed similar simulations, small differences appear in the orbital separation and morphological features of merger remnants. However, we find that there is no significant difference for the identification of carbon detonation and off-center carbon burning.
8. We discuss the difference between our critical mass ratio of the violent merger and that of Pakmor et al. (2011). Considering the inclusion of nuclear burning, initial condition of merger simulations, and numerical resolution, we finally conclude that the initial condition has the largest impact on our results. A preceding state of a merging CO WD

binary is still under debate, especially, whether or not spin-orbit synchronization is achieved until the merger.

9. We estimate the peak brightness distribution of the violent merger-induced SNe Ia using our critical mass ratio, compared it with previous study using q_{cr} of Pakmor et al. (2011), and evaluate the influence of q_{cr} on the brightness distribution. Our results indicate that the influence is much less than that arising from M_1 distribution, which determine the amount of radioactive nickel in the violent merger scenario.
10. Using our $M_1 - q$ diagram (Figure 3.11), we try to predict the final fate of Henize 2-428, which is a bipolar planetary nebula, since the recent observation (Santander-García et al., 2015) claimed that it might host a super-Chandrasekhar DD system, which is a possible SN Ia progenitor. We calculate its mass ratio and primary mass from their observational values, i.e., the orbital period, radial velocity amplitudes, and inclination angle. Comparing results of the calculation with our $M_1 - q$ diagram (Figure 4.17), we show that the DD core of Henize 2-428 would result in an SN Ia explosion during its merger in the violent merger scenario.

The above conclusions are not decisive yet. For instance, because our standard models do not include any nuclear reactions, we cannot follow ignition of detonation consistently, although there is no SPH simulation of CO WD merger that succeeded in igniting carbon detonation self-consistently. Thus, we judge carbon detonation by the detonation condition explained in Section 3.2. However, our condition is based on whether the dynamical carbon burning occurs in the dynamical merger phase, so the condition is just a necessary condition, but not a sufficient condition. Even if satisfying our detonation condition, the models might be unable to initiate carbon detonation and explode in the violent merger scenario.

For the definitive identification whether off-center carbon burning ignites in a merger remnant, we have to follow further evolution of merger remnants in the viscous and thermal evolution phases. As studied in the several previous studies (Yoon et al., 2007; Shen et al., 2012; Schwab et al., 2012), there are possible cases in which off-center carbon burning occur in those evolution phases. Therefore, some of our models which avoid off-center carbon burning might ignite carbon and lead to the AIC, instead of exploding in the AIE scenario. Further study of merger remnant evolution must be done to identify the final products of DD mergers.

As we have discussed in this thesis, mergers of CO WD binaries, i.e., the classical DD model, might be insufficient to explain the total SN Ia population. Recent observational studies implied that SNe Ia are not uniform as we have considered and have several sub groups, and there might be multiple progenitors of SNe Ia. In order to understand their genuine nature, we have to turn our eyes to other progenitor models, such as the He double

detonation scenario, SD scenario, or core degenerate scenario which supposes that an SN Ia arises from a merger of CO WD and AGB core during a common envelope. However, our study also conclude that a part of SNe Ia could arise from CO WD mergers. Some of the sub groups can be products from those different progenitor scenarios. Thus, what we have to do is theoretical prediction of observational features of each different model, and propose future observations by indicating what we have to see. Such studies will allow us to understand the profound nature of SNe Ia.

Acknowledgements

First of all, I would like to thank my supervisor, Izumi Hachisu, for his greatly generous aids. I would like to thank Naohito Nakasato for providing me the numerical code and warm and kind guidance about computational problems. I would like to thank Ataru Tanikawa for his generous supports, helpful discussion, and delightful conversations in ordinary days. I would like to thank Ken'ichi Nomoto for his helpful advice and discussion, and generous financial supports for my research. I would like to thank Keiichi Maeda for his helpful advice and discussion. This study would never be achieved without the extraordinary supports from these supervisor and collaborators.

I am deeply grateful to Toshikazu Shigeyama and the members of his laboratory for allowing me to join their seminar on every Friday. In that seminar, I could obtain greatly useful comments on my study, listen to many interesting talks about various topics, and enjoy ordinary conversations with them. I would like to thank the members of *Toppatsu Tentai (TT)* seminar held on every Friday for their useful discussion. I would like to thank Shin'ichiro Yosida and Takeru Suzuki for their helpful supports and comments in the seminar of my laboratory. I would like to thank Keiko Hisaga for her greatly generous supports for the procedures of my joining conferences, trips, and life in the laboratory. I want to give a special thanks to Kotaro Fujisawa for his extraordinarily generous aids, interesting discussion, very helpful advice, and highly suggestive conversations. I want to express my gratitude to my friends for their various supports and warm encouragements.

Finally, I would like to greatly thank my family for their warm, kind, and generous aids and encouragements. I could not get to here without their supports.

Our simulations in this thesis were performed by using the computational resources of the Kavli Institute for the Physics and Mathematics of the Universe (IPMU) and HA-PACS at the Center for Computational Science at the University of Tsukuba under the Interdisciplinary Computational Science Program.

A part of this thesis has made use of the CfA Supernova Archive, which is funded in part by the National Science Foundation through grant AST 0907903.

Appendix A

Summary of Our Simulation

We summarize the results of our simulations in Table A1. Presented numerical quantities are the primary mass M_1 , secondary mass M_2 , initial orbital separation a_{ini} , maximum temperature during the dynamical merger phase T_{max} , corresponding density $\rho(T_{\text{max}})$, maximum raw temperature at the end of the simulation $T_{\text{max,rem}}$, corresponding density $\rho(T_{\text{max,rem}})$, maximum smoothed temperature at the end of the simulation $T_{\text{s,max,rem}}$, corresponding density $\rho(T_{\text{s,max,rem}})$. Those units are also shown in Table A1. We put them together by each numerical resolutions $10k$, $50k$, $100k$, $500k$, $1000k$, $2000k$ per 1 solar mass and whether or not carbon burning is included. We take some fraction of them from Table 1 of Sato et al. (2015). Our table starts from the next page.

TABLE A.1: Summary of all simulations in this study. See text for details of the variables. Some of the data are taken from Sato et al. (2015).

M_1 (M_\odot)	M_2 (M_\odot)	a_{init} (10^9 cm)	T_{max} (10^9 K)	$\rho(T_{\text{max}})$ (10^6 g cm $^{-3}$)	$T_{\text{max,rem}}$ (10^9 K)	$\rho(T_{\text{max,rem}})$ (10^6 g cm $^{-3}$)	$T_{\text{s,max,rem}}$ (10^9 K)	$\rho(T_{\text{s,max,rem}})$ (10^6 g cm $^{-3}$)
Resolution = $10k M_\odot^{-1}$, without carbon burning								
1.1	1.1	1.22	2.66	6.72	1.81	2.72	1.69	3.12
1.1	1.0	1.42	1.96	3.65	1.41	1.94	1.25	2.52
1.1	0.9	1.64	1.92	3.37	1.25	3.02	1.12	2.98
1.1	0.8	1.86	1.86	1.83	1.18	2.94	1.02	2.37
1.1	0.7	2.11	1.45	0.87	1.25	1.82	0.94	2.74
1.1	0.6	2.40	1.40	1.21	1.01	2.64	0.88	2.48
1.1	0.5	2.75	1.25	1.10	0.97	1.03	0.83	2.29
1.0	1.0	1.40	2.31	4.67	1.40	3.12	1.24	3.03
1.0	0.9	1.61	1.54	3.24	1.05	2.35	0.94	2.16
1.0	0.8	1.81	1.73	2.16	0.93	2.50	0.83	2.01
1.0	0.7	2.05	1.45	1.08	0.90	2.12	0.78	2.51
1.0	0.6	2.35	1.35	1.10	0.82	2.78	0.74	2.52
1.0	0.5	2.68	1.10	0.32	0.82	3.08	0.70	1.88
0.9	0.9	1.62	1.75	2.12	0.99	2.83	0.89	1.20
0.9	0.8	1.79	1.43	1.52	0.84	2.58	0.70	1.55
0.9	0.7	2.06	1.23	1.91	0.72	2.07	0.61	1.98
0.9	0.6	2.34	1.09	0.62	0.68	1.17	0.58	1.37
0.9	0.5	2.67	1.03	0.82	0.65	2.48	0.53	1.15
0.8	0.8	1.77	1.28	2.19	0.68	1.89	0.60	1.30
0.8	0.7	2.00	1.27	1.75	0.57	0.87	0.49	1.41
0.8	0.6	2.26	1.28	0.99	0.77	1.20	0.54	1.20
0.8	0.5	2.58	0.84	0.42	0.57	0.93	0.45	0.45
0.7	0.7	1.95	0.91	1.40	0.55	0.98	0.46	1.26
0.7	0.6	2.21	1.01	1.42	0.50	1.08	0.41	1.08
0.7	0.5	2.49	0.82	0.37	0.45	0.38	0.37	0.86
0.6	0.6	2.16	0.72	1.14	0.45	0.41	0.32	0.41
0.6	0.5	2.40	0.60	0.45	0.41	1.28	0.28	1.06
0.5	0.5	2.35	0.57	1.06	0.30	0.76	0.24	0.49

TABLE A.1: Continued

M_1 (M_\odot)	M_2 (M_\odot)	a_{init} (10^9 cm)	T_{max} (10^9 K)	$\rho(T_{\text{max}})$ (10^6 g cm $^{-3}$)	$T_{\text{max,rem}}$ (10^9 K)	$\rho(T_{\text{max,rem}})$ (10^6 g cm $^{-3}$)	$T_{\text{s,max,rem}}$ (10^9 K)	$\rho(T_{\text{s,max,rem}})$ (10^6 g cm $^{-3}$)
Resolution = $50k M_\odot^{-1}$, without carbon burning								
1.1	1.1	1.23	3.58	6.13	1.56	3.02	1.44	3.09
1.1	1.0	1.44	3.10	4.15	1.27	2.71	1.14	2.83
1.1	0.9	1.65	2.20	2.87	1.13	2.94	0.99	2.36
1.1	0.8	1.89	1.94	1.47	1.08	2.42	0.93	2.80
1.1	0.7	2.13	1.58	0.39	1.00	1.96	0.86	1.76
1.1	0.6	2.42	1.52	0.33	0.94	1.89	0.82	2.19
1.1	0.5	2.79	1.40	0.67	0.96	1.40	0.81	1.49
1.0	1.0	1.42	2.77	3.55	1.11	2.98	0.99	3.08
1.0	0.9	1.62	2.16	2.67	0.94	1.87	0.81	2.73
1.0	0.8	1.85	1.93	1.98	0.86	1.57	0.76	1.29
1.0	0.7	2.09	1.72	0.93	0.85	0.86	0.70	1.31
1.0	0.6	2.37	1.28	0.50	0.79	0.88	0.66	2.01
1.0	0.5	2.73	1.13	0.23	0.72	1.14	0.64	1.41
0.9	0.9	1.62	2.15	2.22	0.77	2.35	0.66	1.55
0.9	0.8	1.84	1.59	2.08	0.69	1.55	0.58	0.85
0.9	0.7	2.09	1.44	0.79	0.64	0.44	0.55	0.44
0.9	0.6	2.37	1.21	0.86	0.62	1.29	0.55	0.70
0.9	0.5	2.73	1.00	0.29	0.63	2.51	0.50	0.37
0.8	0.8	1.80	1.65	1.62	0.58	1.55	0.51	1.91
0.8	0.7	2.03	1.59	1.39	0.56	2.81	0.45	0.68
0.8	0.6	2.30	1.21	0.56	0.51	0.62	0.42	0.62
0.8	0.5	2.65	0.96	0.29	0.49	0.73	0.41	0.38
0.7	0.7	2.00	1.50	0.84	0.53	1.49	0.45	1.07
0.7	0.6	2.29	1.10	1.04	0.45	2.94	0.34	0.32
0.7	0.5	2.61	0.98	0.33	0.42	0.32	0.33	0.32
0.6	0.6	2.22	0.93	0.81	0.48	2.78	0.31	0.55
0.6	0.5	2.52	0.74	0.48	0.36	0.32	0.25	0.32
0.5	0.5	2.44	0.85	0.59	0.35	1.37	0.23	0.27

TABLE A.1: Continued

M_1 (M_\odot)	M_2 (M_\odot)	a_{init} (10^9 cm)	T_{max} (10^9 K)	$\rho(T_{\text{max}})$ (10^6 g cm $^{-3}$)	$T_{\text{max,rem}}$ (10^9 K)	$\rho(T_{\text{max,rem}})$ (10^6 g cm $^{-3}$)	$T_{\text{s,max,rem}}$ (10^9 K)	$\rho(T_{\text{s,max,rem}})$ (10^6 g cm $^{-3}$)
Resolution = $100k M_\odot^{-1}$, without carbon burning								
1.1	1.1	1.25	3.64	5.51	1.39	2.82	1.25	2.88
1.1	1.0	1.45	3.02	6.71	1.23	2.67	1.10	3.11
1.1	0.9	1.67	2.54	4.13	1.17	2.74	1.01	1.73
1.1	0.8	1.86	2.21	1.92	1.08	2.12	0.96	2.96
1.1	0.7	2.11	1.82	1.10	0.98	2.47	0.90	1.51
1.1	0.6	2.39	1.56	0.42	0.95	1.82	0.82	1.24
1.1	0.5	2.72	1.42	1.91	0.92	0.67	0.81	0.83
1.0	1.0	1.43	3.08	4.80	0.98	3.05	0.86	2.57
1.0	0.9	1.64	2.10	3.32	0.93	1.15	0.80	1.70
1.0	0.8	1.87	1.99	2.49	0.84	0.73	0.74	0.97
1.0	0.7	2.13	1.64	1.05	0.81	0.38	0.68	0.45
1.0	0.6	2.40	1.45	1.23	0.77	0.98	0.66	1.16
1.0	0.5	2.75	1.30	0.18	0.75	0.90	0.62	0.78
0.9	0.9	1.64	2.17	3.21	0.78	2.92	0.66	2.09
0.9	0.8	1.86	1.96	1.24	0.71	1.26	0.60	0.97
0.9	0.7	2.08	1.48	1.51	0.66	0.40	0.59	0.38
0.9	0.6	2.35	1.27	0.67	0.65	0.56	0.58	0.72
0.9	0.5	2.68	1.07	0.31	0.59	0.48	0.50	0.50
0.8	0.8	1.83	1.65	2.20	0.59	2.92	0.54	1.31
0.8	0.7	2.07	1.51	0.89	0.58	0.79	0.46	0.97
0.8	0.6	2.35	1.27	0.56	0.57	0.43	0.45	0.37
0.8	0.5	2.69	1.19	0.37	0.50	2.74	0.40	0.51
0.7	0.7	2.01	1.44	1.12	0.49	0.86	0.42	0.79
0.7	0.6	2.27	1.12	0.45	0.47	0.60	0.35	0.46
0.7	0.5	2.60	0.84	0.45	0.46	0.35	0.34	0.32
0.6	0.6	2.25	1.13	0.76	0.49	2.61	0.28	0.43
0.6	0.5	2.55	0.81	0.44	0.32	2.64	0.25	0.35
0.5	0.5	2.47	0.85	0.52	0.40	1.89	0.22	0.32

TABLE A.1: Continued

M_1 (M_\odot)	M_2 (M_\odot)	a_{init} (10^9 cm)	T_{max} (10^9 K)	$\rho(T_{\text{max}})$ (10^6 g cm $^{-3}$)	$T_{\text{max,rem}}$ (10^9 K)	$\rho(T_{\text{max,rem}})$ (10^6 g cm $^{-3}$)	$T_{\text{s,max,rem}}$ (10^9 K)	$\rho(T_{\text{s,max,rem}})$ (10^6 g cm $^{-3}$)
Resolution = $500k M_\odot^{-1}$, without carbon burning								
1.1	1.1	1.25	3.91	5.84	1.18	3.10	0.99	2.90
1.1	1.0	1.46	3.50	3.81	1.18	2.41	1.02	1.63
1.1	0.9	1.67	2.58	4.24	1.10	1.48	1.01	1.11
1.1	0.8	1.91	2.19	2.23	1.04	0.54	0.94	1.01
1.1	0.7	2.16	1.66	1.50	0.96	0.99	0.85	0.91
1.1	0.6	2.45	1.68	0.70	0.95	0.74	0.82	0.89
1.1	0.5	2.81	1.70	0.76	0.90	0.63	0.78	0.61
1.0	1.0	1.43	3.50	4.27	0.92	2.97	0.80	1.82
1.0	0.9	1.64	2.95	3.78	0.90	1.89	0.78	1.77
1.0	0.8	1.87	2.26	1.32	0.87	0.91	0.77	0.73
1.0	0.7	2.11	1.87	0.93	0.84	1.06	0.73	0.33
1.0	0.6	2.40	1.31	0.65	0.79	0.72	0.66	1.11
1.0	0.5	2.74	1.49	0.58	0.78	0.74	0.63	0.51
0.9	0.9	1.64	2.77	3.84	0.79	2.66	0.56	1.19
0.9	0.8	1.86	2.17	1.26	0.64	0.87	0.57	1.03
0.9	0.7	2.11	1.72	0.50	0.64	0.38	0.57	0.40
0.9	0.6	2.40	1.30	0.43	0.63	0.51	0.52	0.46
0.9	0.5	2.75	1.28	0.24	0.59	0.60	0.50	0.36
0.8	0.8	1.82	2.16	2.08	0.57	1.86	0.47	0.44
0.8	0.7	2.06	1.74	0.80	0.50	0.82	0.43	0.53
0.8	0.6	2.34	1.38	0.75	0.50	0.54	0.44	0.24
0.8	0.5	2.67	1.04	0.33	0.50	0.49	0.41	0.17
0.7	0.7	2.05	1.63	1.38	0.51	1.71	0.37	0.59
0.7	0.6	2.31	1.11	0.55	0.48	3.13	0.33	0.22
0.7	0.5	2.65	1.07	0.25	0.44	2.57	0.34	0.15
0.6	0.6	2.24	1.45	1.21	0.50	1.90	0.27	0.49
0.6	0.5	2.55	0.93	0.52	0.40	1.77	0.25	0.10
0.5	0.5	2.47	1.09	0.52	0.41	1.50	0.21	0.38

TABLE A.1: Continued. The second model of $0.9 + 0.75 M_{\odot}$ is the case with non-spinning WDs and the approximate binary setup.

M_1 (M_{\odot})	M_2 (M_{\odot})	a_{init} (10^9 cm)	T_{max} (10^9 K)	$\rho(T_{\text{max}})$ (10^6 g cm $^{-3}$)	$T_{\text{max,rem}}$ (10^9 K)	$\rho(T_{\text{max,rem}})$ (10^6 g cm $^{-3}$)	$T_{\text{s,max,rem}}$ (10^9 K)	$\rho(T_{\text{s,max,rem}})$ (10^6 g cm $^{-3}$)
Resolution = $500k M_{\odot}^{-1}$, without carbon burning								
1.1	0.875	1.73	2.48	3.70	1.06	1.01	0.97	0.77
1.1	0.85	1.79	2.47	2.57	1.11	1.04	0.99	1.41
1.1	0.825	1.85	2.29	4.32	1.05	1.11	0.93	1.17
1.1	0.775	1.97	2.37	1.86	1.04	1.23	0.92	1.31
1.1	0.75	2.03	2.17	2.00	1.01	1.60	0.92	1.02
1.1	0.725	2.10	1.82	0.89	1.00	1.41	0.89	0.84
1.0	0.875	1.70	2.67	2.13	0.93	1.97	0.82	1.17
1.0	0.85	1.76	2.41	2.31	0.90	0.58	0.81	0.93
1.0	0.825	1.82	2.33	3.02	0.90	1.33	0.81	1.27
1.0	0.775	1.93	2.04	2.56	0.87	1.79	0.78	0.57
1.0	0.75	1.99	1.95	2.25	0.89	1.93	0.79	0.82
1.0	0.725	2.06	1.92	1.16	0.85	1.24	0.75	0.83
0.9	0.875	1.70	2.61	4.33	0.74	1.27	0.64	1.66
0.9	0.85	1.76	2.57	2.49	0.74	1.73	0.61	1.90
0.9	0.825	1.81	2.21	2.65	0.79	1.67	0.57	0.51
0.9	0.775	1.93	1.90	2.04	0.63	0.71	0.56	0.59
0.9	0.75	1.99	1.92	0.72	0.62	0.69	0.54	0.66
0.9	0.75	1.86	2.58	1.79	0.69	1.81	0.60	1.13
0.9	0.725	2.06	1.78	0.68	0.64	0.64	0.56	0.59
0.8	0.775	1.88	1.97	2.09	0.55	1.96	0.46	0.47
0.8	0.75	1.94	2.08	1.71	0.58	1.82	0.45	0.42
0.8	0.725	2.01	1.81	1.21	0.54	1.87	0.44	0.35
0.75	0.75	1.91	1.90	2.43	0.56	1.54	0.43	1.04

TABLE A.1: Continued

M_1 (M_\odot)	M_2 (M_\odot)	a_{init} (10^9 cm)	T_{max} (10^9 K)	$\rho(T_{\text{max}})$ (10^6 g cm $^{-3}$)	$T_{\text{max,rem}}$ (10^9 K)	$\rho(T_{\text{max,rem}})$ (10^6 g cm $^{-3}$)	$T_{\text{s,max,rem}}$ (10^9 K)	$\rho(T_{\text{s,max,rem}})$ (10^6 g cm $^{-3}$)
Resolution = 500k M_\odot^{-1} , with carbon burning								
1.1	0.8	1.91	2.67	2.90	1.05	1.50	0.93	0.55
1.1	0.775	1.97	2.46	2.30	1.04	0.31	0.92	0.44
1.1	0.75	2.03	2.35	1.34	0.99	1.66	0.88	0.32
1.1	0.725	2.10	2.33	1.56	0.99	1.38	0.87	2.00
1.0	0.8	1.87	2.65	2.13	0.88	0.88	0.77	0.87
1.0	0.775	1.93	2.58	3.22	0.87	0.44	0.76	0.78
1.0	0.75	1.99	2.33	1.46	0.84	0.91	0.75	0.37
1.0	0.725	2.06	2.29	1.50	0.84	1.27	0.77	0.75
0.9	0.8	1.86	2.66	2.19	0.64	1.19	0.55	0.52
0.9	0.775	1.93	2.51	1.66	0.66	0.51	0.56	0.53
0.9	0.75	1.99	2.48	2.16	0.64	0.58	0.57	0.62
0.9	0.725	2.06	2.19	1.35	0.66	0.46	0.57	0.34
0.8	0.775	1.88	2.51	3.06	0.58	1.91	0.44	0.52
0.8	0.75	1.94	2.32	1.26	0.52	2.01	0.45	0.83
0.8	0.725	2.01	2.45	1.59	0.54	2.04	0.43	0.65
0.75	0.75	1.91	2.46	2.57	0.60	1.77	0.41	0.83
Resolution = 1000k M_\odot^{-1} , without carbon burning								
1.1	0.8	1.87	2.53	1.47	1.11	1.24	1.03	1.11
0.9	0.8	1.84	2.44	0.87	0.65	0.59	0.58	0.54
0.8	0.775	1.89	2.54	1.97	0.63	1.97	0.41	0.46
Resolution = 2000k M_\odot^{-1} , without carbon burning								
1.1	0.8	1.88	2.72	2.27	1.03	1.67	0.92	1.36
0.9	0.8	1.85	2.68	1.23	0.66	1.97	0.53	2.04
0.8	0.775	1.86	2.30	2.21	0.59	2.04	0.42	0.50

Bibliography

- Aarseth, J. S. (1963). In: *MNRAS* 126.223.
- Badenes, C. and D. Maoz (2012). In: *ApJL* 749.L11.
- Balsara, D. S. (1995). In: *Journal of Computational Physics* 121.357.
- Barnes, J. and P. Hut (1986). In: *Nature* 324.446.
- Bedin, L. R. et al. (2014). In: *MNRAS* 439.354.
- Benetti, S. et al. (2006). In: *ApJL* 653.L129.
- Benvenuto, O. G. et al. (2015). In: *ApJL* 809.L6.
- Benz, W. et al. (1990). In: *ApJ* 348.647.
- Bianco, F. B. et al. (2011). In: *ApJ* 741.20.
- Blinnikov, S. I. and A. M. Khokhlov (1987). In: *Soviet Astronomy Letters* 13.364.
- Blondin, S. et al. (2012). In: *AJ* 143.126.
- Bloom, J. S. et al. (2012). In: *ApJL* 744.L17.
- Brooks, J. et al. (2017). In: *ApJL* 834.L9.
- Brown, P. J. et al. (2012a). In: *ApJ* 749.18.
- Brown, P. J. et al. (2012b). In: *ApJ* 753.22.
- Brown, P. J. et al. (2014). In: *ApJ* 787.29.
- Cao, Y. et al. (2015). In: *Nature* 521.328.
- Chakradhari, N. K. et al. (2014). In: *MNRAS* 443.1663.
- Chandrasekhar, S. (1939). "Introduction to the Study of Stellar Structure".
In: *Chicago, Ill., The University of Chicago press.*
- Chen, M. C. et al. (2014). In: *MNRAS* 440.1274.
- Childress, M. J. et al. (2015). In: *MNRAS* 454.3816.
- Chomiuk, L. (2013). In: *PASA* 30.46.
- Chomiuk, L. et al. (2012). In: *ApJ* 750.164.
- Dan, M. et al. (2011). In: *ApJ* 737.89.
- (2012). In: *MNRAS* 422.2417.
- Dan, M. et al. (2014). In: *MNRAS* 438.14.
- Denissenkov, P. A. et al. (2013). In: *ApJ* 772.37.
- Di Stefano, R. (2010). In: *ApJ* 712.728.
- Di Stefano, R. and M. Kilic (2012). In: *ApJ* 759.56.
- Di Stefano, R. et al. (2011). In: *ApJL* 738.L1.
- Dilday, B. et al. (2012). In: *Science* 337.942.
- Eggleton, P. (2006). "Evolutionary Processes in Binary and Multiple Stars".
In: *Cambridge University Press.*
- Eggleton, P. P. (1983). In: *ApJ* 268.368.
- Filippenko, A. V. (1997). In: *ARA&A* 35.309.
- Filippenko, A. V. et al. (1992a). In: *ApJL* 384.L15.
- Filippenko, A. V. et al. (1992b). In: *AJ* 104.1543.
- Fink, M. et al. (2014). In: *MNRAS* 438.1762.
- Foley, R. J. et al. (2012a). In: *ApJ* 744.38.
- Foley, R. J. et al. (2012b). In: *ApJ* 752.101.
- Foley, R. J. et al. (2013). In: *ApJ* 767.57.
- Foley, R. J. et al. (2014). In: *ApJ* 792.29.
- Fossey, S. J. et al. (2014). In: *CBET* 3792.

- Fowler, W. A. and F. Hoyle (1964). In: *ApJS* 9.201.
- Fowler, W. A. et al. (1975). In: *ARA&A* 21.69.
- Frew, D. J. et al. (2016). In: *MNRAS* 455.1459.
- Fryer, C. L. et al. (2010). In: *ApJ* 725.296.
- Fuller, J. and D. Lai (2014). In: *MNRAS* 444.3488.
- Gal-Yam, A. (2016). In: arXiv: 1611.09353.
- Ganeshalingam, M. et al. (2011). In: *MNRAS* 416.2607.
- Ganeshalingam, M. et al. (2012). In: *ApJ* 751.142.
- García-Berro, E. et al. (2016). In: *NewA* 45.7.
- Gilfanov, M. and Á. Bogdán (2010). In: *Nature* 463.924.
- Gingold, R. A. and J. J. Monaghan (1977). In: *ApJ* 181.375.
- González Hernández, J. I. et al. (2012). In: *Nature* 489.533.
- Goobar, A. et al. (2014). In: *ApJL* 784.L12.
- Graham, M. L. et al. (2015). In: *MNRAS* 454.1948.
- Greggio, L. (2005). In: *A&A* 441.1055.
- Guerrero, J. et al. (2004). In: *A&A* 413.257.
- Hachisu, I. (1986). In: *ApJS* 69.479.
- Hachisu, I. et al. (1996). In: *ApJL* 470.L97.
- (1999). In: *ApJ* 522.487.
- (2008a). In: *ApJ* 679.1390.
- (2008b). In: *ApJ* 683.L127.
- (2010). In: *ApJL* 724.L212.
- Hachisu, I. et al. (2012a). In: *ApJ* 744.69.
- Hachisu, I. et al. (2012b). In: *ApJL* 756.L4.
- Hamuy, M. et al. (1993). In: *AJ* 106.2392.
- Hamuy, M. et al. (1996). In: *AJ* 112.2391.
- Hamuy, M. et al. (2003). In: *Nature* 424.651.
- Hayden, B. T. et al. (2010). In: *ApJ* 722.1691.
- Hicken, M. et al. (2007). In: *ApJL* 669.L17.
- Hillebrandt, W. and J. C. Niemeyer (2000). In: *ARA&A* 38.191.
- Hillebrandt, W. et al. (2007). In: *A&A* 465.L17.
- Hillebrandt, W. et al. (2013). In: *Frontiers of Physics* 8.116.
- Höflich, P. (1995). In: *ApJ* 443.89.
- Howell, D. A. (2011). In: *Nature Communications* 2.350.
- Howell, D. A. et al. (2006). In: *Nature* 443.308.
- Hoyle, F. and W. A. Fowler (1960). In: *ApJ* 132.565.
- Iben, I. Jr. and A. V. Tutukov (1984). In: *ApJS* 54.335.
- Inutsuka, S. I. (2002). In: *Journal of Computational Physics* 179.238.
- Itoh, N. et al. (1996). In: *ApJS* 102.411.
- Iwamoto, K. et al. (1999). In: *ApJS* 125.439.
- Jha, S. et al. (2006). In: *AJ* 131.527.
- Ji, S. et al. (2013). In: *ApJ* 773.136.
- Jones, S. et al. (2016). In: *A&A* 593.A72.
- Jordan IV, G. C. et al. (2012). In: *ApJL* 761.L23.
- Justham, S. (2011). In: *ApJL* 730.L34.
- Kasen, D. (2010). In: *ApJ* 708.1025.
- Kashi, A. and N. Soker (2011). In: *MNRAS* 417.1466.
- Kashyap, R. et al. (2015). In: *ApJL* 800.L7.
- Kato, M. and I. Hachisu (1994). In: *ApJ* 437.802.
- Kato, M. et al. (2014). In: *ApJ* 793.136.
- Kelly, P. L. et al. (2014). In: *ApJ* 790.3.

- Kerzendorf, W. E. et al. (2012). In: *ApJ* 759.7.
- Kerzendorf, W. E. et al. (2013). In: *ApJ* 774.99.
- Khokhlov, A. M. (1991). In: *A&A* 245.L25.
- Kleinman, S. J. et al. (2013). In: *ApJS* 204.5.
- Kobayashi, C. et al. (1998). In: *ApJL* 503.L155.
- Kromer, M. et al. (2013a). In: *MNRAS* 429.2287.
- Kromer, M. et al. (2013b). In: *ApJL* 778.L18.
- Kromer, M. et al. (2015). In: *MNRAS* 450.3045.
- Kromer, M. et al. (2016). In: *MNRAS* 459.4428.
- Kushnir, D. et al. (2013). In: *ApJL* 778.L37.
- Kutsuna, M. and T. Shigeyama (2015). In: *PASJ* 67.54.
- Lecoanet, D. et al. (2016). In: *ApJ* 832.71.
- Leibundgut, B. et al. (1993). In: *AJ* 105.301.
- Leonard, D. C. (2007). In: *ApJ* 670.1275.
- Leonard, D. C. et al. (2002). In: *AJ* 124.2490.
- Li, W. et al. (2003). In: *PASP* 115.453.
- Li, W. et al. (2011a). In: *Nature* 480.348.
- Li, W. et al. (2011b). In: *MNRAS* 412.1441.
- Li, W. et al. (2011c). In: *MNRAS* 412.1473.
- Liu, Z.-W. and R. J. Stancliffe (2016). In: *MNRAS* 459.1781.
- Livne, E. (1990). In: *ApJL* 354.L53.
- Lorén-Aguilar, P. et al. (2009). In: *A&A* 500.1193.
- Lucy, L. B. (1977). In: *AJ* 82.1013.
- Lundqvist, P. et al. (2013). In: *MNRAS* 435.329.
- Lundqvist, P. et al. (2015). In: *A&A* 577.A39.
- Maeda, K. et al. (2010). In: *Nature* 466.82.
- Maguire, K. et al. (2011). In: *MNRAS* 418.747.
- Maguire, K. et al. (2013). In: *MNRAS* 436.222.
- Maguire, K. et al. (2016). In: *MNRAS* 457.3254.
- Maoz, D. and N. Hallakoun (2016). In: arXiv: 1609.02156.
- Maoz, D. et al. (2014). In: *ARA&A* 52.107.
- Margutti, R. et al. (2012). In: *ApJ* 751.134.
- Marietta, E. et al. (2000). In: *ApJS* 128.615.
- Marion, G. H. et al. (2016). In: *ApJ* 820.92.
- Marsh, T. R. et al. (2004). In: *MNRAS* 350.113.
- Matheson, T. et al. (2008). In: *AJ* 135.1598.
- Mattila, S. et al. (2005). In: *A&A* 443.649.
- Mazzali, P. A. et al. (1995). In: *A&A* 297.509.
- Mazzali, P. A. et al. (2007). In: *Science* 315.825.
- McCully, C. et al. (2014). In: *Nature* 512.54.
- McMillan, P. J. (2011). In: *MNRAS* 414.2446.
- Millard, J. et al. (1999). In: *ApJ* 527.746.
- Moll, R. et al. (2014). In: *ApJ* 785.105.
- Monaghan, J. J. (1992). In: *ARA&A* 30.543.
- (2005). In: *RPPh* 68.1703.
- Moriya, T. et al. (2010). In: *ApJ* 719.1445.
- Morris, J. P. and J. J. Monaghan (1997). In: *Journal of Computational Physics* 136.41.
- Nakasato, N. et al. (2012). In: arXiv: 1206.1199.
- Napiwotzki, R. et al. (2001). In: *Astronomische Nachrichten* 322.411.
- Noda, K. et al. (2016). In: *PASJ* 68.11.

- Noebauer, U. M. et al. (2016). In: *MNRAS* 463.2972.
- Nomoto, K. (1982a). In: *ApJ* 253.798.
- (1982b). In: *ApJ* 257.780.
- Nomoto, K. and I. Jr. Iben (1985). In: *ApJ* 297.531.
- Nomoto, K. and Y. Kondo (1991). In: *ApJL* 367.L19.
- Nomoto, K. et al. (1984). In: *ApJ* 286.644.
- Nugent, P. et al. (1997). In: *ApJ* 485.812.
- Nugent, P. E. et al. (2011). In: *Nature* 480.344.
- Olling, R. P. et al. (2015). In: *Nature* 521.332.
- Pakmor, R. et al. (2008). In: *A&A* 489.943.
- Pakmor, R. et al. (2010). In: *Nature* 463.61.
- Pakmor, R. et al. (2011). In: *A&A* 528.A117.
- Pakmor, R. et al. (2012a). In: *ApJL* 747.L10.
- Pakmor, R. et al. (2012b). In: *MNRAS* 424.2222.
- Patat, F. et al. (2007). In: *Science* 317.924.
- Perlmutter, S. et al. (1999). In: *ApJ* 517.565.
- Phillips, M. M. (1993). In: *ApJL* 413.L105.
- Phillips, M. M. et al. (2007). In: *The Publications of the Astronomical Society of the Pacific* 119.360.
- Phillips, M. M. et al. (2013). In: *ApJ* 779.38.
- Prieto, J. L. et al. (2007). In: arXiv: 0706.4088.
- Pskovskii, I. P. (1977). In: *Soviet Astronomy* 21.675.
- Rasio, F. A. and S. L. Shapiro (1995). In: *ApJ* 438.887.
- Raskin, C. and D. Kasen (2013). In: *ApJ* 772.1.
- Raskin, C. et al. (2012). In: *ApJ* 746.62.
- Riess, A. G. et al. (1998). In: *AJ* 116.1009.
- Rodríguez, M. et al. (2001). In: *A&A* 337.1042.
- Röpke, F. K. et al. (2012). In: *ApJL* 750.L19.
- Rosswog, S. (2009). In: *NewAR* 53.78.
- Ruiter, A. J. et al. (2011). In: *MNRAS* 417.408.
- Ruiter, A. J. et al. (2013). In: *MNRAS* 429.1425.
- Saio, H. and K. Nomoto (1985). In: *A&A* 150.L21.
- (1998). In: *ApJ* 500.388.
- (2004). In: *ApJ* 615.444.
- Santander-García, M. et al. (2015). In: *Nature* 519.63.
- Sato, Y. et al. (2015). “A Systematic Study of Carbon-Oxygen White Dwarf Mergers: Mass Combinations for Type Ia Supernovae”. In: *ApJ* 807.105.
URL: <http://dx.doi.org/10.1088/0004-637X/807/1/105>.
- (2016). “The Critical Mass Ratio of Double White Dwarf Binaries for Violent Merger-induced Type Ia Supernova Explosions”. In: *ApJ* 821.67.
URL: <http://dx.doi.org/10.3847/0004-637X/821/1/67>.
- Scalzo, R. et al. (2014a). In: *MNRAS* 440.1498.
- Scalzo, R. A. et al. (2010). In: *ApJ* 713.1073.
- Scalzo, R. A. et al. (2014b). In: *MNRAS* 445.2535.
- Schaefer, B. and A. Pagnotta (2012). In: *Nature* 481.164.
- Schwab, J. et al. (2012). In: *MNRAS* 427.190.
- Schwab, J. et al. (2015). In: *MNRAS* 453.1910.
- Seitzzahl, I. R. et al. (2009). In: *ApJ* 696.515.
- Seitzzahl, I. R. et al. (2013). In: *MNRAS* 429.1156.
- Shappee, B. J. et al. (2013). In: *ApJL* 762.L5.
- Shappee, B. J. et al. (2016). In: arXiv: 1610.07601.

- Shen, K. J. et al. (2012). In: *ApJ* 748.35.
- Shen, K. J. et al. (2013). In: *ApJL* 770.L35.
- Silverman, J. M. et al. (2011). In: *MNRAS* 410.585.
- Silverman, J. M. et al. (2013a). In: *ApJ* 772.125.
- Silverman, J. M. et al. (2013b). In: *ApJS* 207.3.
- Sim, S. A. et al. (2010). In: *ApJL* 714.L52.
- Smartt, S. J. (2009). In: *ARA&A* 47.63.
- Soker, N. et al. (2013). In: *MNRAS* 431.1541.
- Sternberg, A. et al. (2011). In: *Science* 333.856.
- Sullivan, M. et al. (2011). In: *ApJ* 732.118.
- Tanaka, M. et al. (2010). In: *ApJ* 714.1209.
- Tanikawa, A. et al. (2015). In: *ApJ* 807.40.
- Taubenberger, S. et al. (2008). In: *MNRAS* 385.75.
- Taubenberger, S. et al. (2011). In: *MNRAS* 412.2735.
- Taubenberger, S. et al. (2013). In: *ApJL* 775.L43.
- Thacker, R. J. et al. (2000). In: *MNRAS* 319.619.
- Thielemann, F.-K. et al. (1986). In: *A&A* 158.17.
- Thomas, P. A. and H. M. P. Couchman (1992). In: *MNRAS* 257.11.
- Timmes, F. X. and D. Arnett (1999). In: *ApJS* 125.277.
- Timmes, F. X. and F. D. Swesty (2000). In: *ApJS* 126.501.
- Timmes, F. X. et al. (1995). In: *ApJS* 98.617.
- Tominaga, N. et al. (2005). In: *ApJL* 633.L97.
- Totani, T. et al. (2008). In: *PASJ* 60.1327.
- Umeda, H. et al. (1999). In: *ApJ* 513.861.
- van den Heuvel, E. P. J. et al. (1992). In: *A&A* 262.97.
- van Kerkwijk, M. H. et al. (2010). In: *ApJL* 722.L157.
- Wang, L. and J. C. Wheeler (2008). In: *ARA&A* 45.433.
- Webbink, R. F. (1984). In: *ApJ* 277.355.
- Whelan, J. and I. Jr. Iben (1973). In: *ApJ* 186.1007.
- White, C. J. et al. (2015). In: *ApJ* 799.52.
- Woosley, S. E. and T. A. Weaver (1995). In: *ApJS* 101.181.
- Yakovlev, D. G. and D. A. Shyalybkov (1989). In: *Astrophysics and Space Physics Reviews* 319.311.
- Yamanaka, M. et al. (2009). In: *ApJL* 707.L118.
- Yamanaka, M. et al. (2016). In: *PASJ* 68.68.
- Yoon, S.-C. and N. Langer (2004). In: *A&A* 419.623.
- (2005). In: *A&A* 435.967.
- Yoon, S. C. et al. (2007). In: *MNRAS* 380.933.
- Yuan, F. et al. (2010). In: *ApJ* 715.1338.
- Yungelson, L. R. and A. G. Kuranov (2017). In: *MNRAS* 464.1607.
- Yungelson, L. R. and M. Livio (2000). In: *ApJ* 528.108.
- Zhu, C. et al. (2013). In: *ApJ* 767.164.